Structural Perspectives on Glycosaminoglycan-Binding Proteins and Their Receptors

by

Wei Feng

A Dissertation Presented in Partial Fulfillment
of the Requirements for the Degree
Doctor of Philosophy

Approved March 2019 by the
Graduate Supervisory Committee:

Xu Wang, Chair
Jeff Yarger
Giovanna Ghirlanda

ARIZONA STATE UNIVERSITY

May 2019

ABSTRACT

Glycosaminoglycans (GAGs) are long chains of negatively charged sulfated polysaccharides. They are often found to be covalently attached to proteins and form proteoglycans in the extracellular matrix (ECM). Many proteins bind GAGs through electrostatic interactions. GAG-binding proteins (GBPs) are involved in diverse physiological activities ranging from bacterial infections to cell-cell/cell-ECM contacts. This thesis is devoted to understanding how interactions between GBPs and their receptors modulate biological phenomena. Bacteria express GBPs on surface that facilitate dissemination and colonization by attaching to host ECM. The first GBP investigated in this thesis is decorin binding protein (DBP) found on the surface of *Borrelia burgdorferi*, causative pathogens in Lyme disease. DBPs bind GAGs of decorin, a proteoglycan in ECM. Of the two isoforms, DBPB is less studied than DBPA. In current work, structure of DBPB from *B. burgdorferi* and its GAG interactions were investigated using solution NMR techniques. DBPB adopts a five-helical structure, similar to DBPA. Despite similar GAG affinities, DBPB has its primary GAG-binding site on the lysine-rich C terminus, which is different from DBPA. Besides GAGs, GBPs in ECM also interact with cell surface receptors, such as integrins. Integrins belong to a big family of heterodimeric transmembrane proteins that receive extracellular cues and transmit signals bidirectionally to regulate cell adhesion, migration, growth and survival. The second part of this thesis focuses on α_M I-domain of the promiscuous integrin $\alpha_M\beta_2$ (Mac-1 or CD11b/CD18) and explores the structural mechanism of α_M I-domain interactions with pleiotrophin (PTN) and platelet factor 4 (PF4), which are cationic

proteins with high GAG affinities. After completing the backbone assignment of α_M I-domain, paramagnetic relaxation enhancement (PRE) experiments were performed to show that both PTN and PF4 bind α_M I-domain using metal ion dependent adhesion site (MIDAS) in an Mg^{2+} independent way, which differs from the classical Mg^{2+} dependent mechanism used by all known integrin ligands thus far. In addition, NMR relaxation dispersion analysis revealed unique inherent conformational dynamics in α_M I-domain centered around MIDAS and the crucial C-terminal helix. These dynamic motions are potentially functionally relevant and may explain the ligand promiscuity of the receptor, but requires further studies.

DEDICATION

To my parents

ACKNOWLEDGMENT

Throughout the course of my years as a graduate student, I have received encouragement and support from many people. First, I would like to appreciate my advisor Dr. Xu Wang for his mentorship, encouragement and patience. He taught me how good structural biology is done at the bench and beyond the bench. In addition, his scientific and editorial advices are crucial to the completion of the thesis. Second, I want to thank Dr. Brian Cherry from ASU Magnetic Resonance Research Center for the maintenance of spectrometers used in the work. Third, I am grateful to my committee members, Drs. Jeff Yarger, Giovanna Ghirlanda and Petra Fromme for their guidance.

Many colleagues in Dr. Wang's lab have been generous and helped me a lot. I would like to thank Di Shen and Dr. Hanqing Deng for performing microscale thermophoresis analysis. I am also grateful to our collaborators Drs. Tatiana Ugarova and Nataly Podolnikova for their insightful comments on manuscripts.

Finally, I would like to thank my family and friends for their love and support. My deepest gratitude goes to my twin brother for sharing this wonderful life journey from day one, my dad for everything, and my mother for always supporting and believing in me. None of this would have been possible without you.

TABLE OF CONTENTS

Page

CHAPTER Page

CHAPTER Page

APPENDIX

LIST OF TABLES

LIST OF FIGURES

CHAPTER 1

INTRODUCTION

1.1 Glycosaminoglycan (GAG)-binding Proteins (GBPs)

Glycosaminoglycans are long negatively charged heteropolysaccharide chains of repeating disaccharide units of an amino sugar and a uronic acid. Depending on disaccharide unit composition and sulfation pattern, GAGs can be classified into the following categories: hyaluronic acid (HA), chondroitin sulfate (CS), dermatan sulfate (DS), keratin sulfate (KS), heparan sulfate (HS) and heparin (HP). Details of the aforementioned GAG composition and properties are summarized in Table 1.1 (1). Most GAGs, except for HA, are covalently attached to core proteins to form entities known as proteoglycan (PG), often found on cell surface or extracellular matrix (ECM). Of all GAG types, heparan sulfate (HS) and heparin (HP) are probably the most studied due to their high affinities for protein ligands. Structures of major GAG disaccharide units are illustrated in Figure 1.1 (2).

GAGs are known to bind to a broad spectrum of proteins. The number of GAG-binding proteins (GBPs) is estimated to be several hundred (3,4). Among them are chemokines, growth factors, enzyme inhibitors and extracellular matrix (ECM) proteins (5,6). Through various protein ligands, GAGs mediate multiple processes through modulation of cell-cell and cell-ECM interactions. These include development and differentiation, immune response (inflammation), cancer, infectious diseases and neurodegenerative diseases (2,7-19). Some of previously reported GBPs are summarized in Table 1.2 (20). GAG bindings have various effects on proteins, including but not

limited to, protection from proteolysis, regulation of binding to other proteins, protein oligomerization, modulation of enzyme activity and immobilization of proteins (21). Most GBPs identified interact with heparin/heparan sulfate with high affinity due to high sulfation content, in contrast to the relatively small number of proteins that bind CS, DS or KS specifically (21).

GAG	Molecular properties Mw Disaccharide Mw Polydispersity (PD)	Average chain length in disaccharides	Sulpho groups (per disaccharide unit)	Structure
Hyaluronan (HA)	~100–1000 kDa 379.1 Da	260–2600	0	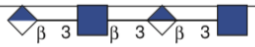
Heparin (HP)	~15 kDa> 476.9 Da PD – 1.4	~30	~2.7	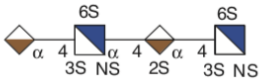
Heparan sulphate (HS)	~20 kDa 459.1 Da	~40	~1	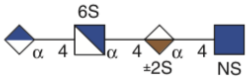
Chondroitin sulphate –A (CSA)	~20 kDa 469 Da PD – 1.2	~40	≤1	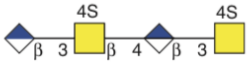
Chondroitin sulphate-B (CSB or DS)	~30 kDa 459.1 Da	~60	≤1	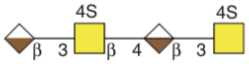
Chondroitin sulphate-C (CSC)	~20 kDa 459.1 Da	~40	≤1	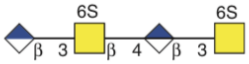
Chondroitin sulphate-D (CSD)	~20 kDa 539 Da	~40	~2	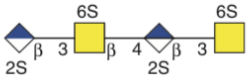
Chondroitin sulphate-E (CSE)	~20 kDa 539 Da	~40	~2	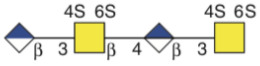
Keratan sulphate-I (KS I)	~14 kDa 500 Da	~35 ~10	~1.5	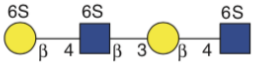
Keratan sulphate-II (KS II)	~5 kDa 500 Da			

Glucuronic acid (GlcA) Glucosamine (GlcN) N-Acetylglucosamine (GlcNAc) Iduronic acid (IdoA) Galactose (Gal) N-Acetylgalactosamine (GalNAc)
Structure of the major disaccharide units are represented based on the consortium for functional glycomics nomenclature. The abbreviations 2S, 4S or 6S indicate 2-*O*, 4-*O* or 6-*O*-sulpho, respectively. Mw, molecular weight.

Table 1.1 Composition and Property of GAGs.
Reprinted with permission from Kamhi, E., Joo, E. J., Dordick, J. S., and Linhardt, R. J. (2013) Glycosaminoglycans in infectious disease. Biological reviews of the Cambridge Philosophical Society 88, 928-943. Copyright (2013) John Wiley and Sons. See Appendix C.

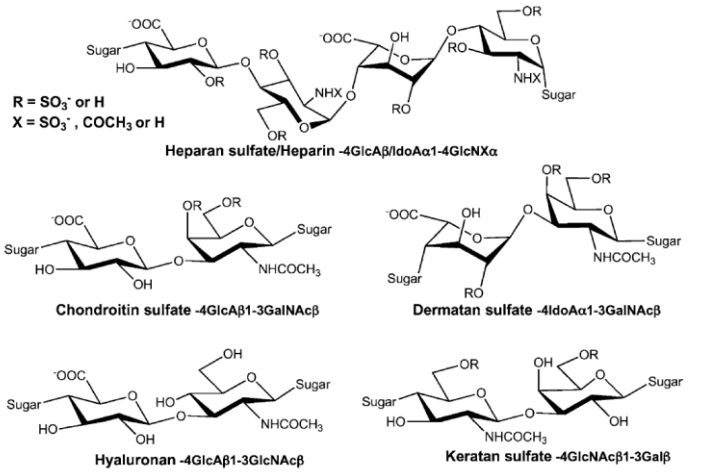

Figure 1.1 Structures of Repeating Disaccharide Units in Common GAGs.
Reprinted with permission from Linhardt, R. J., and Toida, T. (2004) Role of glycosaminoglycans in cellular communication. Accounts of chemical research 37, 431-438. Copyright (2004) American Chemical Society. See Appendix D.

Morphogens
- Activin
- BMP-2, -4
- Chordin
- Sonic hedgehog
- Frizzled-related peptides
- Sprouty peptides
- Wnt (1–13)

Growth factor binding proteins (BP)
- Follistatin
- IGF BP-3, -5
- TGF-β BP
- Noggin

Anti-angiogenic factors
- Angiostatin
- Endostatin
- PF4

Collectins
- SPA, D
- MBP

Antimicrobial peptides
- PR-39
- Bac 5, 7
- β defensin

Growth factors and receptors
- EGF family
  - Amphiregulin
  - Betacellulin
  - Heparin-binding-EGF
  - Neuregulin
- FGFs (1–23)/FGFRs
- PDGF/PDGFR
- GDNF/cRet
- VEGFs/VEGFRs
- HGF/cMet
- TGFβ1, -2

ECM components
- Fibrin
- Fibronectin
- Interstitial collagens
- Laminins
- Pleiotropin (HB-GAM)
- Tenascin
- Thrombospondin
- Vitronectin
- Fibrillin
- Tropoelastin

Energy balance
- Agouti signaling peptide
- Agouti-related protein
- ApoB, E
- Lipoprotein lipase
- Triglyceride lipases

Tissue remodeling
- Tissue plasminogen activator
- Plasminogen activator inhibitor-1
- Protease nexin I
- TIMP-3

Complement proteins (25)
Contact system protein (4)
Coagulation proteins
- Antithrombin III
- Heparin cofactor II
- Leuserpin
- Tissue factor pathway inhibitor
- Thrombin
- Factors IX, X, XI, and XII

Proteinases
- Neutrophil elastase
- CathepsinG
- MCP-4, -5
- Carboxypeptidase A

Unclassified
- Acetylcholinesterase
- HIP
- Thyroglobulin
- Cyclophilin A
- Superoxidase dismutase

Cell adhesion molecules
- E-, L-, P-selectins
- MAC-1
- N-CAM
- PECAM

Chemokines
- C–C, for example MIP-1a, RANTES
- CXC, for example IP-10, IL-8

Cytokines
- GM-CSF
- IL-2, -3, -4, -5, -7, -12
- Interferon γ
- Kininogen
- TNF-α

Viral and parasite
Coat proteins
- HIV-1 tat
- HIV-1 gp41, 120
- HSV gB, gC, gD
- HHV-6 gp65
- HHV-8 gK8.1A
- Circumsprorozoite

Table 1.2 A list of Reported GAG-binding Proteins.
Reprinted with permission from Zhang, L. (2010) Glycosaminoglycan (GAG) biosynthesis and GAG-binding proteins. Progress in molecular biology and translational science 93, 1-17. Copyright (2010) Elsevier. See Appendix E.

1.2 Protein-glycosaminoglycan Interactions

Protein-GAG bindings are dominated by electrostatic interactions between positively charged basic residues in proteins and negatively charged GAG chains. The premise leads researchers to investigate if consensus sequences for GAG binding exist in protein ligands. As the most negatively charged GAG type, heparin has been heavily used in investigations of GAG-protein systems. The first study was reported in 1989 by Cardin and Weintraub (22). They proposed two binding motifs after studying GAG-binding regions of four heparin-binding proteins (apolipoproteins B, apolipoprotein E, vitronectin and platelet factor 4). The two binding motifs are XBBXBX and XBBBXXBX, in which B denotes basic amino acids (lysine, arginine and histidine) and X denotes hydropathic (neutral and hydrophobic) amino acids (alanine, glycine, isoleucine, leucine and tyrosine). These motifs were also identified in other heparin-binding proteins. In their modeling, when these motifs reside in β strands, basic residues would be oriented on one side while hydrophobic residues are positioned on the opposite side, pointing toward the protein core. When the motif is on α helix, basic residues are concentrated on one side of the helix while hydrophobic residues are located back towards the protein core. These arrangements facilitate binding of negatively charged GAGs to positively charged residues in proteins. Using the same strategy, a third consensus sequence, XBBBXXBBBXXBBX, was discovered from another heparin binding protein, von Willebrand factor, by Sobel et al. (23).

However, further investigations revealed that the previously proposed motifs do not apply in all cases. Basic residues that are not close in sequence may be positioned close in the folded conformation as the GAG binding site. An excellent example is the

observation made by Margalit et al. (24). Using molecular modeling, they revealed that the ~ 20 Å distance between basic amino acids on opposite sides of the protein is essential for heparin bindings, whether the residues are on α helix or β strand. In this scenario, the heparin molecule coils around the protein in such a way to bind sequence-distant basic residues, with the possibility of inducing conformational changes.

Other factors also affect GAG-protein bindings. Basic amino acid type is one of them. Arginines bind GAGs with 2.5-fold higher affinity than lysines. This is likely to be a result of stronger hydrogen bonding between the guanidine group of arginine and the sulphate of heparin (25). In addition, basic amino acid pattern and spacing influence GAG bindings. Synthetic peptides with different positive charge density, -RRG$_m$RR- and -RRRG$_m$R-, were tested with heparin and heparin sulfate. Highly sulfated heparin binds tighter with higher charge density -RRRG$_m$R- motif while less sulfated heparan sulfate binds tighter with lower charge density -RRG$_m$RR- motif (26). As GAG bindings involve spatially close basic residues in a binding surface with only a small segment of GAG chains, one single long GAG chain could interact with multiple proteins at different sites in a way that facilitates cooperative binding and possibly leads to protein oligomerization (21).

1.3 Functions Of Glycosaminoglycan-binding Proteins (GBPs) in Bacterial Infection.

Since most GAGs are incorporated into proteoglycans displayed on cell surface or in ECM, GAGs and GBPs primarily mediate cell-cell and cell-ECM interactions. Pathogen-cell contact exemplifies such interactions. Accumulating evidences indicate that GAG bindings are associated with enhanced viral and bacterial infection (27). As

eukaryotic cells and pathogens both have GAGs on surface, surface proteins on pathogens bind to host cell GAGs and vice versa, mediating adhesion and invasion onto host cells (27). For bacterial pathogenesis, a key step is attachment onto and colonization of host cells. As host cells are glycosylated, GBPs on bacterial surface provide initial "weak" contact with host cells, thus facilitating subsequent binding to host cell surface receptors with more stable interactions (28,29). GAG-protein interactions also contribute to bacterial infections by promoting bacterial internalization into host cells or by blocking access of cationic antimicrobial proteins to host cells with GAGs (30-32).

Examples of bacterial GBPs are adhesins on *Borrelia burgdorferi*, the causative pathogen of Lyme disease. Lyme disease is the most commonly found tick-borne disease in the Northern Hemisphere (33,34). Its symptoms range from the classical erythema migrans (bull's-eye rash skin lesion) in the early stage and neurological and cardiovascular manifestations in the secondary stage to arthritis in the late stage (34). Lyme disease is transmitted through ixodid ticks infected with *Borrelia* bacteria. The specific strain of pathogen causing Lyme disease in North America is *Borrelia burgdorferi* (34,35).

B. burgdorferi expresses many GAG-binding lipoproteins on surface. These lipoproteins are crucial for the spirochete dissemination and immune invasion (35). Two well-known lipoproteins are decorin binding proteins A and B (DBPA/DBPB). DBPs bind DS chains of decorin (36,37). Besides DS, DBPs also bind other GAGs, such as HP and HS (38-40). As a matter of fact, HP binds DBPs with a higher affinity than DS due to its high sulfation density (40). DBPA has a lower sequence homology (~ 40 %) than

DBPB (~ 60 - 99.5 %) among difference strains (41,42). Although both contribute to the overall virulence, DBPA and DBPB have unequal effects in dissemination and colonization (43). As sequences of DBPB are less heterogeneous, it is a potentially more valuable therapeutic target. There have been more studies on DBPA than DBPB. First structure of DBPA was determined with solution NMR in 2012 (40). As shown in Figure 1.2, B31 version of DBPA adopts a five-helix structure and contains a basic patch as the GAG-binding site. The basic patch consists of C terminus, the linker between helices 1 and 2, and parts of helices 2 and 5, revealed by electrostatic potential mapping (40). A later study using X-ray crystallography confirmed the structure (44).

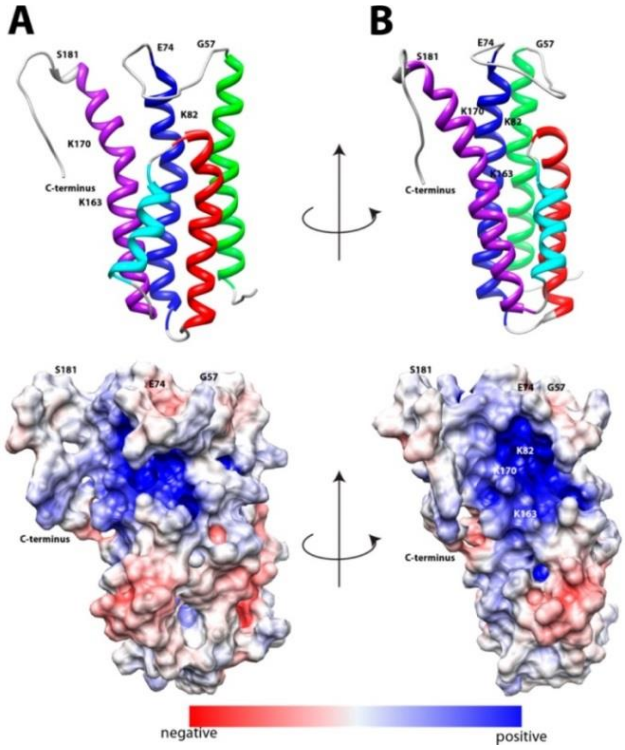

Figure 1.2 Electrostatic Potential Surface Map of B31 DBPA.
Surface is color coded with red for acidic and blue for basic regions. (A) and (B) are different orientations with 90° rotation about the vertical axis.

Current work on DBPB will be explored in Chapter 2. Using solution NMR, B31 DBPB structure was determined. Although DBPA and DBPB have similar GAG binding affinities, GAG-binding epitopes on DBPB are different from DBPA.

1.4 Non-Proteoglycan Receptors for GAG-binding Proteins (GBPs)

Extracellular matrix (ECM) is a key feature of multi-cellular eukaryotic organisms. This complex multi-component network is composed of polysaccharides and proteins (45). ECM provides dynamic environments needed for cell survival, migration, differentiation and tissue organization (45,46). As discussed above, many GBPs reside in ECM due to the abundance of GAGs in ECM. Surprisingly, many non-proteoglycan cell surface receptors recognize and bind cationic proteins, many of which are also GBPs. One of these non-proteoglycan receptors is integrin. Through binding ECM components, integrin mediate cell adhesion, migration, growth and survival (47). Integrin evolved early in metazoan history and all multi-cellular animals express the protein (48). In fact, integrin is so named for its role as integral membrane proteins that connect ECM and cytoskeleton network (49). All integrins are composed of non-covalently bound α and β subunits. Both α and β chains are type-1 transmembrane proteins with large extracellular domains and small cytosolic domains. α and β chains have around 1000 and 750 amino acid residues respectively. In vertebrates, 24 types of heterodimers are formed through assembly of 18 α and 8 β subunits (47). 9 out of the 18 α subunits contain an extra inserted domain, known as α I or α A domain (50). Based on this domain, the protein

family can be categorized into α I-domain containing integrins and α I-domain less integrins. The following discussions will focus on α I-domain containing integrins.

A complete understanding of how integrin functions is not possible without solving the structure of integrin. The long-awaited breakthrough was made in 2001 by Xiong et al. (51). They determined the extracellular domain structure of integrin $\alpha_v\beta_3$. This was followed by structures solved for $\alpha_{IIb}\beta_3$ (52) and $\alpha_x\beta_2$ (53). Surprisingly, all these crystal structures display "bent" conformations with N-terminal ligand binding regions (head) oriented close to where membrane surface would be *in vivo*, making the headpieces less accessible to ligands. Integrin domain organizations and ectodomain structure of $\alpha_x\beta_2$ are illustrated in Figure 1.3 (52,53). As shown in Figure 1.3, α chain contains a seven-bladed β-propeller, a thigh domain, two calf domains followed by a transmembrane domain and an intracellular domain. α I-domain is inserted between the second and third blades of β-propeller in α I-domain containing integrins (50). A similar I domain is also found in β chain. β I-domain is inserted in hybrid domains which are flanked by plexin-semaphorin-integrin (PSI) domains, on top of four epidermal growth factor (EGF) domains, a β-tail, a transmembrane domain and an intracellular domain. Bend is located in the leg region between thigh and calf-1 on α subunit and, between EGF-1 and EGF-2 on β subunit (52-54).

The discovery of the "bent" topology was unexpected as earlier observations from low resolution electron microscopy (EM) studies showed that the globular N-terminal extracellular regions (head) sit on long legs in an open/extended manner (55-62). Later on, accumulating evidences suggested that multiple conformations exist, including bent and

extended (63,64). Recent advances in super-resolution microscopy provided direct optical measurements of integrin extension from the membrane on cell surface (65,66). The global structural rearrangement is involved in integrin activation, as proposed in the switchblade model (47). The switchblade model postulates large scale of "bent to extended" conformational changes as shown in shown in Figure 1.4 (47).

As displayed in Figure 1.4, integrins exist in three different conformations: bent (closed), extended (closed) and extended (open). Disruption of weak interactions that stabilize the bent conformation would lead to straightening of the ectodomains. In α I-domain containing integrins, α I-domain serves as the primary ligand binding site. Specifically, an acidic residue in α I-domain serves as an intrinsic ligand for β I-domain. When this intrinsic ligand binds metal ion dependent adhesion site (MIDAS) of β I-domain, a downward movement of ~ 10 Å in the α7 helix of α I-domain would further induce structural rearrangements in its MIDAS and lead to enhanced ligand bindings (47,67).

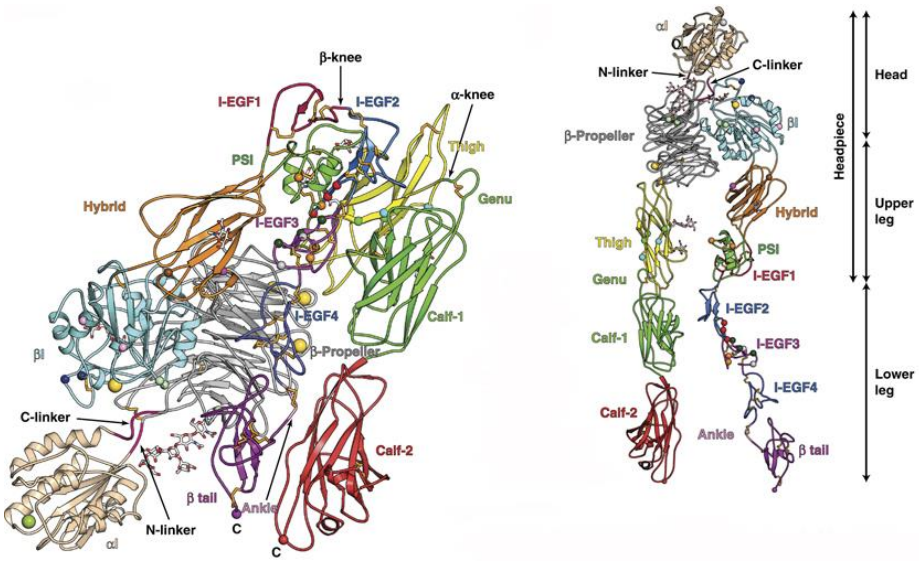

Figure 1.3 Crystal Structure of Integrins αxβ2 Ectodomains.
Structures are extended on the right for clear visualization of domain organizations.
Reprinted with permission from Xie, C., Zhu, J., Chen, X., Mi, L., Nishida, N., and Springer, T. A. (2010) Structure of an integrin with an alphaI domain, complement receptor type 4. The EMBO journal 29, 666-679. Copyright (2010) John Wiley and Sons. See Appendix G.

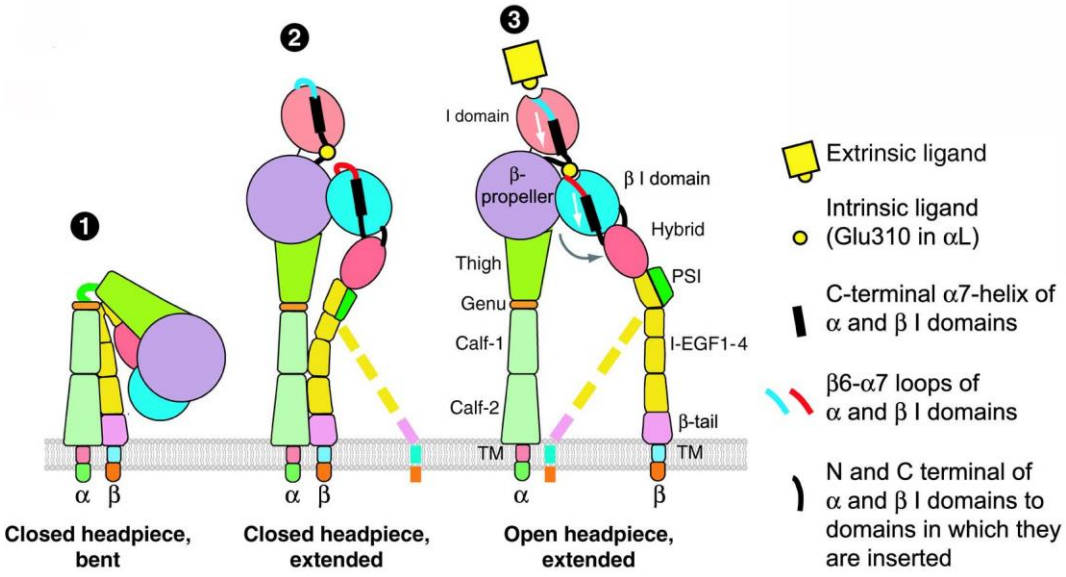

Figure 1.4 Structural Rearrangements in Activation of α I-domain Containing Integrins.
Reprinted with permission from Luo, B. H., Carman, C. V., and Springer, T. A. (2007) Structural basis of integrin regulation and signaling. Annual review of immunology 25, 619-647. Copyright (2007) ANNUAL REVIEWS. See Appendix H.

Many integrins have broad ligand binding specificities. Integrin $\alpha_M\beta_2$ (Mac-1 or CD11b/CD18) in fact is one of the most promiscuous members of integrin family. Over 40 ligands have been identified and more are expected (68). A recent study discovered that Mac-1 has high binding affinity for peptides with high occurrence of basic amino acids (68). As the ligand binding site of Mac-1, α_M I-domain was investigated in current studies with cationic ligands. Two proteins, pleiotrophin (PTN) and platelet factor 4 (PF4), were selected. PTN is a cytokine while PF4 is a chemokine. Both PTN and PF4

are highly positively charged and have high binding affinity for GAGs (69,70). They have been found to interact with Mac-1 and induce leukocyte responses through Mac-1. Binding sites for PTN and PF4 are localized to α_M I-domain in Mac-1 (71,72). Current works aim to investigate structural biology of α_M I-domain interaction with cationic ligands, and the conformational dynamics of α_M I-domain using NMR techniques. Chapter 3 is on the NMR backbone assignment of α_M I-domain. Chapter 4 explores the novel interaction mechanism of α_M I-domain with cationic ligands. Chapter 5 focuses on preliminary characterization of α_M I-domain dynamics using NMR relaxation dispersion experiments.

CHAPTER 2

STRUCTURE OF DECORIN BINDING PROTEIN B FROM BORRELIA BURGDORFERI AND ITS INTERACTIONS WITH GLYCOSAMINOGLYCANS

(*Reprinted with permission from Feng, W., and Wang, X. (2015) Structure of decorin binding protein B from Borrelia burgdorferi and its interactions with glycosaminoglycans. Biochimica et biophysica acta 1854, 1823-1832. Copyright (2015) Elsevier. See Appendix I.***)**

2.1 Abstract

Decorin-binding proteins (DBPs), DBPA and DBPB, are surface lipoproteins on *Borrelia burgdorferi*, causative agent of Lyme disease. DBPs bind to the connective tissue proteoglycan decorin and facilitate tissue colonization by the bacterium. Although structural and biochemical properties of DBPA are well understood, little is known about DBPB. In current work, we determined the solution structure of DBPB from strain B31 of *B. burgdorferi* and characterized its interactions with glycosaminoglycans (GAGs). Our structure shows DBPB adopts the same topology as DBPA, but possesses a much shorter terminal helix, resulting in a longer unstructured C-terminal tail, which is also rich in basic amino acids. Characterization of DBPB-GAG interactions reveals that, despite similar GAG affinities of DBPA and DBPB, the primary GAG-binding sites in DBPB are different from DBPA. In particular, our results indicate lysines in the C-terminus of DBPB are vital to DBPB's ability to bind GAGs whereas C-terminal tail for DBPA from strain B31 only plays a minor role in facilitating GAG bindings. Furthermore,

the traditional GAG-binding pocket important to DBPA-GAG interactions is only secondary to DBPB's GAG-binding ability.

2.2 Introduction

Borrelia burgdorferi is the causative agent of Lyme disease, which is the most prevalent vector-borne disease in North America. As an extracellular bacterium, *B. burgdorferi* relies almost entirely on host cells for nutrients. Because of its parasitic life cycle, *B. burgdorferi* has developed many strategies for adhering to and evading detection by the host. Many of the proteins involved in promoting the adhesion of the bacteria to the host cells have shown to be important to the virulence of the bacteria (1,2). Understanding the mechanisms of these virulent factors is therefore an important aspect in tackling *B. burgdorferi* infection.

One of the *B. burgdorferi* adhesins identified is decorin binding protein (DBP), a cell surface lipoprotein that is expressed during the mammalian infection stage (3). Two homologous forms of DBP, termed DBPA and DBPB, exist in the *B. burgdorferi* genome. Both are lipoproteins of approximately 20 kDa in size, and they share ~ 40 % sequence identity. Genetic studies of the two isoforms show both are important for the bacteria during early stages of infection (4-6). Although the two isoforms can compensate one another to a limited extent, absence of either one can produce defects in joint colonization and DBPB overexpression also inhibits proper dissemination of the bacterium (7,8). Interestingly, DBPA shows high sequence diversity among different strains of *Borrelia* bacteria, while DBPB sequence is well conserved (9-11).

DBPs facilitate bacterial colonization by adhering to proteoglycans in the extracellular matrix (ECM) and on cell surfaces. The ECM proteoglycan decorin is a particular important target for DBPs (3,12), and the glycosaminoglycan (GAG) portion of decorin is a major binding site for the DBPs (13-15). GAGs are sulfated linear polysaccharides composed of repeating disaccharide units of uronic acids and amino sugars (16). Because of their high sulfation density and large size, GAGs have strong interactions with a number of extracellular proteins via electrostatic interactions. This enables them to act as receptors for signaling proteins and microbes. Although the GAG chains found in decorin are either chondroitin sulfate (CS) or dermatan sulfate (DS), which contain N-acetylgalactosamine (GalNAc) only, DBPs are also known to interact with other GAG types including heparin and heparan sulfate (HS), both of which contain glucosamine instead of GalNAc. In fact, DBPA's affinity for heparin is significantly higher than its affinity for DS (9,13,14,17). The core protein of decorin is also suspected to play a role in facilitating the interactions between decorin and DBPs (12,13). However, there is yet no evidence of direct interactions between the decorin core protein and DBPs.

Although DBPA has been extensively studied functionally and structurally (10,13,18,19), very little information is available on DBPB. The lack of information is curious considering that one reason for the interest in DBPs is their potential as vaccine components. However, the high genetic diversity of DBPA means a single vaccine may not be sufficient in eliciting immunity against all strains of the bacterium. In this respect, DBPB, whose sequence is well conserved among different strains, may be a better

candidate for vaccine development. In fact, antibody against DBPB has been one of the most common antibodies found in serums of humans infected with the bacterium (20).

We have determined the solution structure of DBPB from strain B31 of *Borrelia burgdorferi* using solution NMR and characterized its interactions with GAGs. Structure of DBPB is homologous to the known DBPA structures. In particular, it is composed of five helices with an unstructured linker between helices one and two as well as a flexible C-terminal tail. However, the C-terminal helix of DBPB is considerably shorter than the helix in DBPA, resulting in a longer unstructured C-terminal tail that is enriched in basic amino acids. Characterizations of DBPB-GAG interactions showed DBPB has similar GAG affinities as DBPA, but possesses different binding sites than DBPA. In particular, although some of the lysine residues deemed important to DBPA's affinity for GAGs are also conserved in DBPB, the most important GAG-binding site in DBPB is its lysine-rich C-terminus, the elimination of which reduced the GAG affinity of DBPB significantly. These results indicate DBPB may be as important in facilitating bacterial adhesion as the well-studied DBPA.

2.3 Materials and Methods

1, Expression and purification of B31 DBPB

The open reading frame (ORF) of the wild type (WT) B31 DBPB (residues 21-187) was synthesized by Genscript Inc. (Piscataway, NJ) and cloned into the pHUE vector with ORF of His-tagged ubiquitin at the 5' end (21). Residue C21, which acts as the lipid anchor *in vivo*, was mutated to serine to prevent dimerization (3). To construct DBPB mutants, the following forward primers were designed: K65S/K69S, 5'-

GCGTTCACCGGCCTGAGCACGGGTAGCAGCGTTACCTCTGG-3'; R78S/K81S, 5'-GGCGGTCTGGCCCTGAGCGAAGCAAGCGTGCAGGCGATTG-3'; K81S, 5'-GGCCCTGCGCGAAGCAAGCGTGCAGGCGATTGTG-3'; K169S, 5'-GAAAGTGGTTAAAGAAAGCCAGAACATCGAAAACGG-3'; ^{184}SSSS^{187}, 5'-GGGCTCCGCGGTGGATCGAGC-3'; DBPB$_{21\text{-}183}$, 5'-GAAAAACAACAAAAGCTAAAAGAAAAAATGAAAG-3'. The reverse primers were designed: K65S/K69S, 5'-CCAGAGGTAACGCTGCTACCCGTGCTCAGGCCGGTGAACGC-3'; R78S/K81S, 5'-CAATCGCCTGCACGCTTGCTTCGCTCAGGGCCAGACCGCC-3'; K81S, 5'-CAACAATCGCCTGCACGCTTGCTTCGCGCAGGGCC-3'; K169S, 5'-CCGTTTTCGATGTTCTGGCTTTCTTTAACCACTTTC-3'; ^{184}SSSS^{187} 5'-GGGAAGCTTTCAGCTGCTGCTGCTGCTTTTGTTGTTTTT-3'; DBPB$_{21\text{-}183}$, 5'-CTTTCATTTTTTCTTTTAGCTTTTGTTGTTTTTC-3'. The mutagenesis was done with the Agilent Quickchange site-directed mutagenesis kit according to the manufacturer's protocol, and confirmed by sequencing.

Escherichia coli BL21 (DE3) cells transformed with the expression vectors were grown in M9 medium at 37 °C to an OD_{600} of 0.8. The cells were then induced with 0.5 mM IPTG before overnight incubation at 30 °C. $^{15}NH_4Cl$ and/or ^{13}C glucose were added into M9 medium for desired isotopic labeling. After cell harvesting by centrifugation, the resuspended cells were treated with 1 mg/mL lysozyme for 20 min and lysed via sonication. After centrifugation, the supernatant was subjected to Ni-affinity chromatography with a 5 mL HisTrap column (GE Life Sciences). The bound DBPB was

eluted from the column by applying an imidazole gradient of 35 to 500 mM at a flow rate of 3 mL/min. After exchanging the pooled protein into 25 mM Tris and 100 mM NaCl buffer (pH 8.0), the fusion protein was cleaved with 1/20 molar equivalent of USP2 (deubiquitinase) overnight at room temperature (21). Another Ni-affinity chromatography was applied to separate cleaved DBPB from His-tagged ubiquitin and His-tagged USP2.

2, Production of GAG fragments and TEMPO-labeled GAG fragments

Heparin and DS from Sigma-Aldrich were partially depolymerized using heparinase I (IBEX Inc.) and chondroitinase ABC (Sigma-Aldrich), respectively (22,23). Digested fragments were separated based on size with a 2.5 cm × 175 cm size exclusion chromatography column (Bio-Rad Biogel P10) at a flow rate of 0.2 mL/min. Fractions containing fragments of the same size were pooled, desalted, and lyophilized. For paramagnetic relaxation enhancement (PRE) studies, DS dodecasaccharide, or dp12 (degree of polymerization 12) fragments were paramagnetically labeled by modifying the reducing end with the nitroxide radical, 4-amino-TEMPO, through reductive amination (19). Specifically, 300 uM TEMPO was mixed with 1 mg of GAG fragments and 25 mM $NaCNBH_3$, and incubated at 65 °C for three days. After desalting, labeled fragments were further purified using SAX-HPLC.

3, Acquisition and analysis of NMR data for DBPB structure and backbone dynamics

NMR experiments were conducted on Bruker Ultra-Shield 600 MHz and Varian Inova 800 MHz spectrometers. Most of the pulse sequences were provided by the manufacturer. For backbone assignment, HNCACB, HNCOCACB, HNCO, and HNCOCA spectra were acquired for ^{13}C- and ^{15}N-labeled DBPB. To determine DBPB

structure, ^{15}N- and ^{13}C-edited NOESY-HSQC spectra were obtained for ^{13}C- and ^{15}N-labeled DBPB. Methyl group assignments were made with the methyl HCCH-TOCSY experiments (24) while side chain proton assignments were made using a combination of HCCH-TOCSY, HCCONH and ^{13}C-edited NOESY-HSQC. HN and NC residual dipolar couplings (RDCs) were measured with DBPB aligned in a 7% neutral polyacrylamide gel using J-modulated pulse sequences (25). NMR samples contain 100-600 uM of ^{13}C- and/or ^{15}N-labeled DBPB in 50 mM NaH_2PO_4 and 150 mM NaCl buffer (pH 6.5). All NMR data were processed with NMRPipe (26) and analyzed using NMRView (27).

For PRE studies, 400 uL of 150 uM WT ^{15}N-labeled DBPB was mixed with 8 molar equivalents of TEMPO-labeled DS dp12. PRE effect arising from the TEMPO-labeled fragments was estimated by collecting a ^{1}H-^{15}N HSQC spectrum before and after the radical was reduced by adding 3 uL of 1 M ascorbic acid (28).

To investigate the effects of GAG-binding on backbone mobility, backbone nitrogen T_1, T_2, and steady state heteronuclear nuclear Overhauser effect (NOE) were measured for WT ^{15}N-labeled DBPB with or without 10 molar equivalents of heparin dp10. Relaxation delays for longitudinal relaxation (T_1) and transverse relaxation (T_2) experiments were 0.1, 0.25, 0.4, 0.6, 0.8, 1.0 s and 10, 20, 40, 60, 80, 100 ms, respectively. Steady state heteronuclear NOE was extracted by calculating peak intensity ratios of spectra collected with or without proton saturation of 3 s. The order parameter S^2 was calculated with the program relax (29) using the isotropic global rotational diffusion model. The global rotational correlation time, τ_m, was approximated as the average rotational correlation times of all structured residues. The residue-specific correlation

times (τ_c) were determined according to the method of Kay et al. (30). Specifically, τ_c is estimated using the equation: $\tau_c = 1/(4(\pi\nu_N) \times [6(T_1/T_2) - 7]^{1/2}$, in which ν_N is the resonance frequency of ^{15}N in Hz. DS-induced millisecond time scale conformational exchange was measured on a sample containing 300 uM ^{15}N-labeled DBPB and 3 mM DS dp10 using the CPMG-based relaxation dispersion experiment designed by Tollinger et al. (31). The R_2 values were extracted by conducting two-point transverse relaxation measurements at relaxation delays of 5 and 50 ms. The field strength was varied from 10 to 210 Hz. The exchange component of the relaxation was estimated as the difference in R_2 values at field strengths of 10 and 210 Hz.

4, Structure calculation

Backbone dihedral angles of well-ordered residues were determined with the online server TALOS+ (32). ^{13}C- and ^{15}N-edited NOESY-HSQC spectra were analyzed manually to find unambiguous long-range contacts. The partially assigned peak lists were then used as input for CYANA's automatic structure determination procedure (33). The structures and constraint tables generated by CYANA were subsequently used in XPLOR-NIH for refinement with RDCs of HN and NC (34). The 10 structures with the least NOE violations were shown as the ensemble in the present article.

5, Gel mobility shift assay

Heparin and DS fragments were fluorescently labeled with 2-aminoacridone (2-AMAC) according to the method of Lyon et al. (35). To confirm DBPB-GAG binding and size dependency of the interaction, 2 ug of 2-AMAC labeled heparin or DS fragments (dp4, dp6, dp8, and dp10) were incubated in 50 mM NaH_2PO_4 and 150 mM

NaCl buffer (pH 6.5) containing 0 or 1 molar equivalent of WT DBPB. Gel mobility shift assays (GMSAs) were also carried out to compare the GAG binding affinities between DBPB and DBPA and between different mutants of DBPB. In these GMSAs, 1.5 ug of 2-AMAC heparin dp6 or DS dp10 was treated with 0, 0.5, and 1 molar equivalent of proteins. For all GMSAs, the mixtures were incubated at room temperature for 30 min and subjected to electrophoresis at 120 V for 15-25 min in 1% agarose gels made with 10 mM Tris-HCl, 1mM EDTA buffer (pH 6.4).

6, Affinity assay with immobilized GAGs

To compare the affinities of WT and mutant DBPBs for native GAGs, ELISA assays were performed with biotinylated heparin and DS immobilized on the neutravidin coated microwell plates (G-Biosciences). To prepare biotinylated GAGs, 550 ul reaction mixtures containing 1 mg of heparin or DS, 0.6 mM biotin, 2.5 mM EDC, 0.1 mM NHS and 100 mM MES (pH 5.5) were incubated overnight at room temperature and buffer exchanged to remove excess labels. For the ELISA, 2 ug of biotinylated heparin or DS was immobilized in each neutravidin well and probed with 2 ug of His-tagged WT DBPA, WT DBPB or mutant DBPBs. His-tagged ubiquitin was used as negative control. To detect bindings on all ELISA assay plates, anti-HIS antibodies conjugated to horseradish peroxidase (HRP) from Qiagen were added. The assays were developed using tetramethylbenzidine (TMB) as the substrate and then quenched with 100 uL of 0.1 M HCl. Each ELISA was performed at least twice, and four replicates of each sample were analyzed to calculate average and standard deviation.

7, Titrations of DBPs with GAG fragments

For WT and mutant DBPBs titrations, aliquots of 5 mM heparin dp10 were added to 400 uL of 50 mM NaH_2PO_4 and 150 mM NaCl buffer (pH 6.5) containing 100 uM protein to reach final concentrations of 0.2, 0.6, 1.0, 1.4, 1.8, and 2.2 mM. A ^{1}H-^{15}N HSQC spectrum was collected at each titration point. Chemical shift changes in ^{1}H and ^{15}N dimensions were combined to a single chemical shift value δ (36) using the equation $\delta = [\Delta\delta_H^2 + (2\Delta\delta_N)^2]^{1/2}$, with $\Delta\delta_H$ and $\Delta\delta_N$ representing the respective chemical shift changes in Hz on ^{1}H and ^{15}N dimensions. The Kds were determined using the 1:1 binding model in the software xcrvfit (http://www.bionmr.ualberta.ca/bds/software/xcrvfit/), which takes into consideration ligand depletion during the titration. Titrations of WT DBPB with heparin dp6 and DS dp10 were performed under the same conditions.

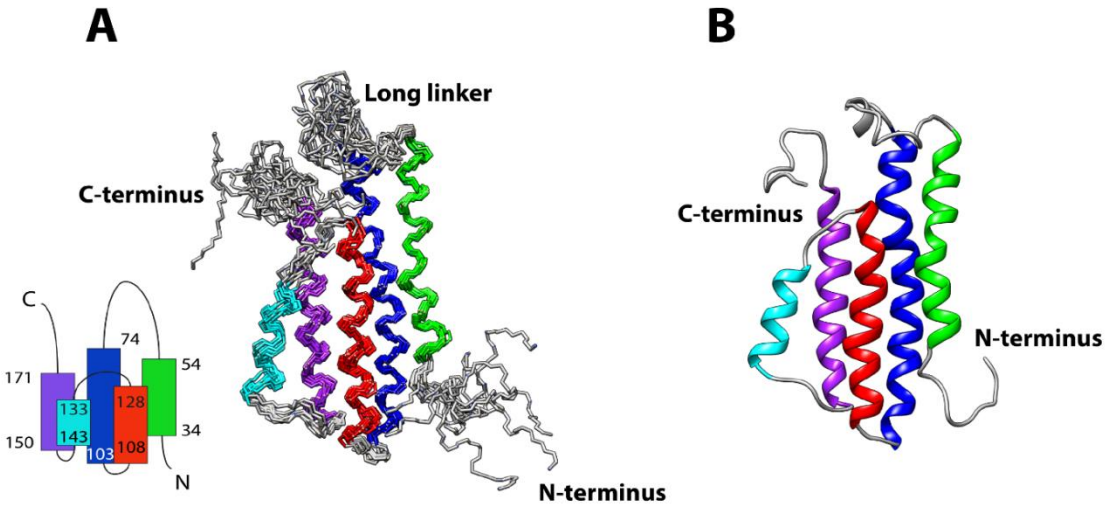

Figure 2.1 Solution Structures of DBPB.
(A) Ensemble of the 10 lowest-energy DBPB structures. Helix 1, consisting of residues 34 to 54, is colored green. Helix 2, consisting of residues 74 to 103, is colored blue. Helix 3, consisting of residues 108 to 128, is colored red. Helix 4, consisting of residues 133 to 143, is colored cyan. Helix 5, consisting of residues 150 to 171, is colored purple. The topology of DBPB is shown at the bottom left. (B) Ribbon depiction of a representative DBPB structure.

2.4 Results

1, DBPB Structure

In this study, the structure of DBPB was determined using solution NMR methods. The ensemble of 10 DBPB structures most consistent with the experimental data is depicted in Figure 2.1. Table 2.1 shows the structural statistics for the ensemble. In agreement with the previous predictions, the solution structure of DBPB adopts a conformation very similar to the known DBPA structures (10,18). Specifically, DBPB consists of five helices as well as two flexible segments arranged similarly as DBPA. This topology brings the linker (residues 55-73) between helices one and two and the C-terminal tail in proximity. Extensive hydrophobic contacts between residues in helices two, three and five have been identified in NOESY, leading to the formation of the hydrophobic core that establishes the tertiary fold of the protein. Hydrogen/deuterium exchange experiments were also performed to measure the stability of the helices. Not surprisingly, backbone amide protons of residues in helices two, three and five showed the least hydrogen / deuterium exchange (data not shown), indicating the three helices are the most stable helices in the protein, consistent with their participation in the hydrophobic core.

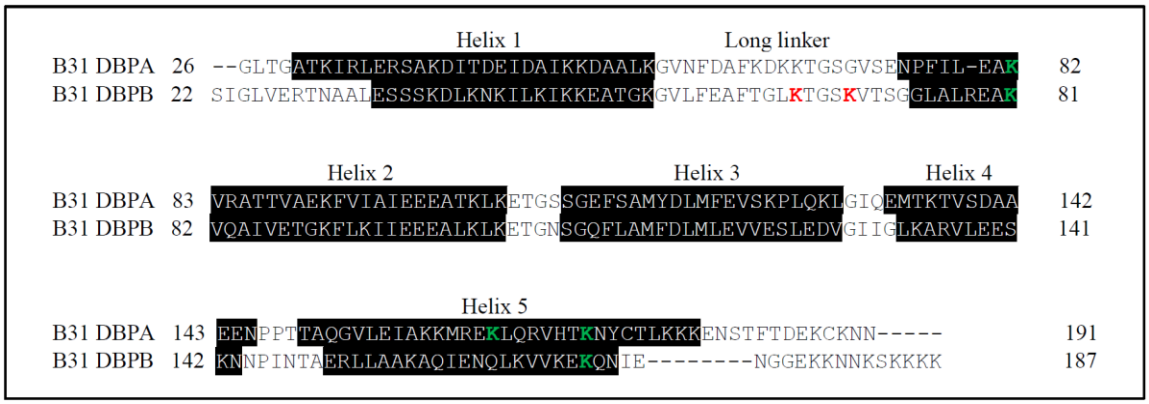

Figure 2.2 Sequence Alignment of B31 DBPA and B31 DBPB.
Lipidation signals of the proteins are not shown. Secondary structures are labeled with helices in black boxes. K82, K163 and K170 are colored green in DBPA. K65 and K69 are colored red, while conserved K81 and K169 are colored green in DBPB.

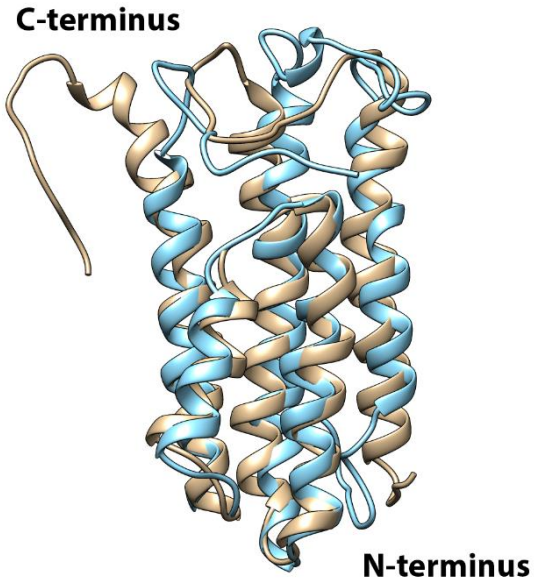

Figure 2.3 Superimposition of B31 DBPA and B31 DBPB Structures.
Ribbon representation of DBPA (pdb: 2lqu) is shown in gold and ribbon representation of DBPB is shown in cyan.

Despite these similarities, DBPB differs from DBPA structurally in several respects. Figure 2.2 shows the sequence alignment of DBPA and DBPB from strain B31

of *B. burgdorferi* and positions of the helices in these proteins. The alignment reveals that secondary structural elements are well conserved between the two. However, the helical content of DBPB is lower than DBPA because helices one and five in DBPB are shorter than those in DBPA. Figure 2.3 is the superimposition of DBPA and DBPB structures. The helices of the two structures superimpose with a backbone RMSD of 2.0 Å. The superimposition shows that the positions of the helices are also conserved between the proteins, but shortening of helix five has resulted in a longer unstructured C-terminus in DBPB. Moreover, cysteines in the C-terminal tail and helix five of DBPA form a disulfide bond that restrains the C-terminal tail to DBPA's core domain and reduces the tail's flexibility. However, such an intramolecular disulfide bond is missing in DBPB's C-terminus. Backbone dynamics experiments described below suggest the C-terminus as well as the linker between helices one and two are indeed very flexible. Another notable difference between B31 DBPA and DBPB is the lack of BXBB motif in the linker of DBPB. The BXBB motif in the linker has been shown to be an important GAG-binding site for GAGs in B31 DBPA(19). The lack of a similar sequence in DBPB means the linker of DBPB may not play a role in GAG binding.

Because GAG-protein interactions are dominated by electrostatic attractions, electrostatic potential on the surface of the protein is predictive of possible GAG-binding sites. Figure 2.4 is the electrostatic potential map of DBPB. To avoid artifacts produced by the artificial cavity formed when the flexible segments are placed near the binding pocket, we removed the C-terminus and the linker between helices one and two and only calculated the electrostatic potential map of the core domains. A large basic patch can be

seen in a pocket composed of helices two and five. A similar patch has also been observed in DBPA and was shown to be important in GAG binding (10,37). In agreement with the observation, the basic patch in DBPB includes residues K81 and K169, which are equivalent to two of the three GAG-binding residues identified in DBPA (Figure 2.2) (37).

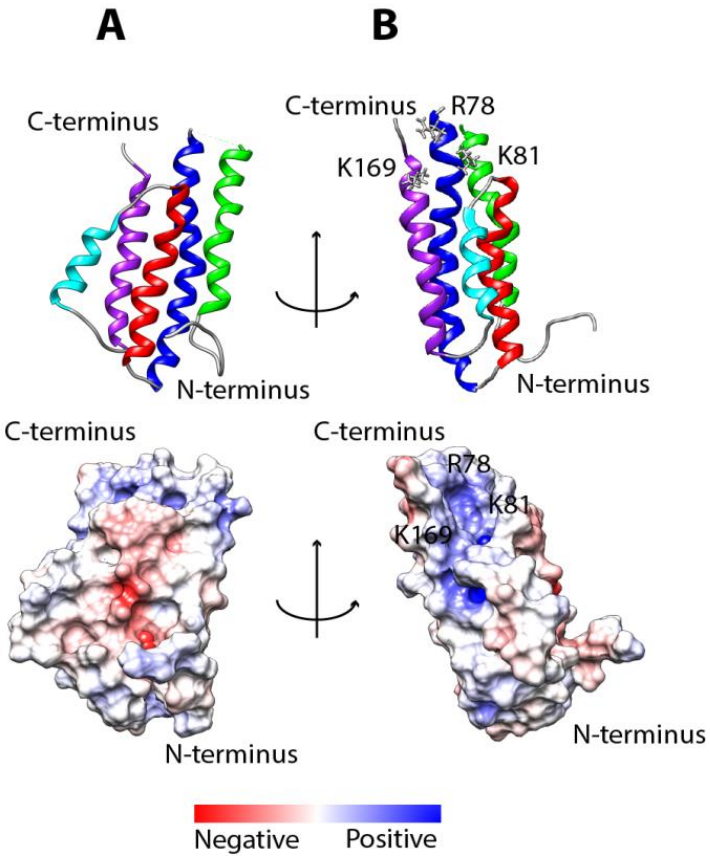

Figure 2.4 Electrostatic Potential Surface Map of DBPB.
Calculation of the surface electrostatic potential was carried out without the flexible linker and the C-terminal tail. (A) DBPB is in the same orientation as Figure 2.1B. (B) DBPB is rotated by 90 degrees about the vertical axis. R78, K81 and K169 are outlined.

2, Interactions of DBPB with GAGs

WT DBPB was analyzed in a series of experiments to characterize its GAG-binding properties. A qualitative examination using GMSA was carried out with WT DBPB and GAG fragments of defined sizes. In particular, fluorescently labeled heparin and DS tetrasaccharide (dp4), hexasaccharide (dp6), octasaccharide (dp8) and decasaccharide (dp10) were run on 1% agarose gel with or without DBPB. As shown in Figure 2.5, DBPB shifted a larger fraction of heparin fragments than DS fragments, indicating that DBPB binds heparin more strongly than DS. This is not unexpected considering the highly sulfated nature of heparin. The observations are also in line with previous studies using native long GAG chains, in which heparin was shown to be more effective in inhibiting bacterial adhesion than DS (14,15).

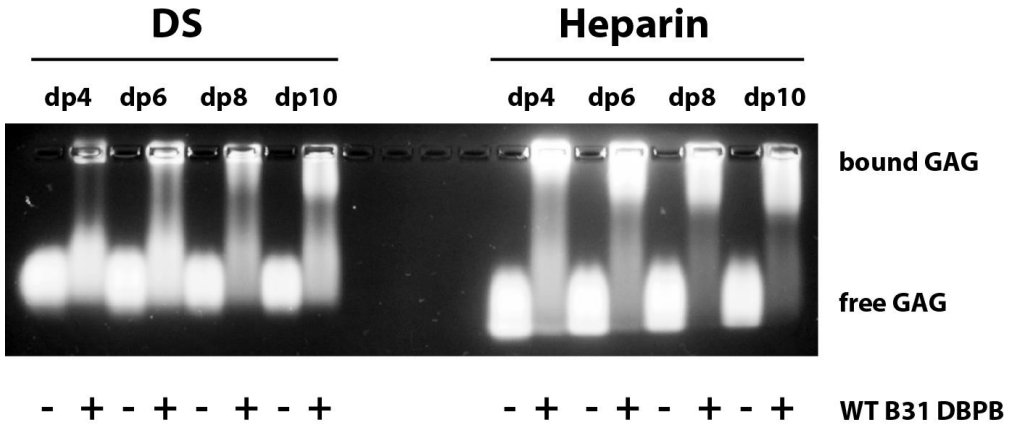

Figure 2.5 Gel Mobility Shift Assay Evaluation of WT DBPB's Interactions with Heparin and DS.

To obtain more quantitative affinity estimates, we also carried out NMR-monitored titrations of DBPB using heparin and DS. As is often the case with GAG-binding proteins, long GAG chains induce protein oligomerization and lead to NMR signal broadening without revealing useful information on the GAG-binding residues. As

a result, heparin dp10 and DS dp10 fragments were used in NMR analysis of DBPB-GAG interactions. Figure 2.6A shows ^{1}H-^{15}N HSQC spectra of DBPB titrated with heparin dp10 and Figure 2S1 shows the ^{1}H-^{15}N HSQC spectra of DBPB titrated with DS dp10. The amide proton and nitrogen chemical shift changes induced by both ligands are small compared to those seen in B31 DBPA (10). Small chemical shift changes have been conventionally associated with multiple binding modes in protein-ligand interactions, which can reduce magnitudes of chemical shift changes as a result of chemical shift averaging between different binding conformations. Observations of these small chemical shift changes indicate DBPB-GAG interactions are less specific than DBPA-GAG interactions.

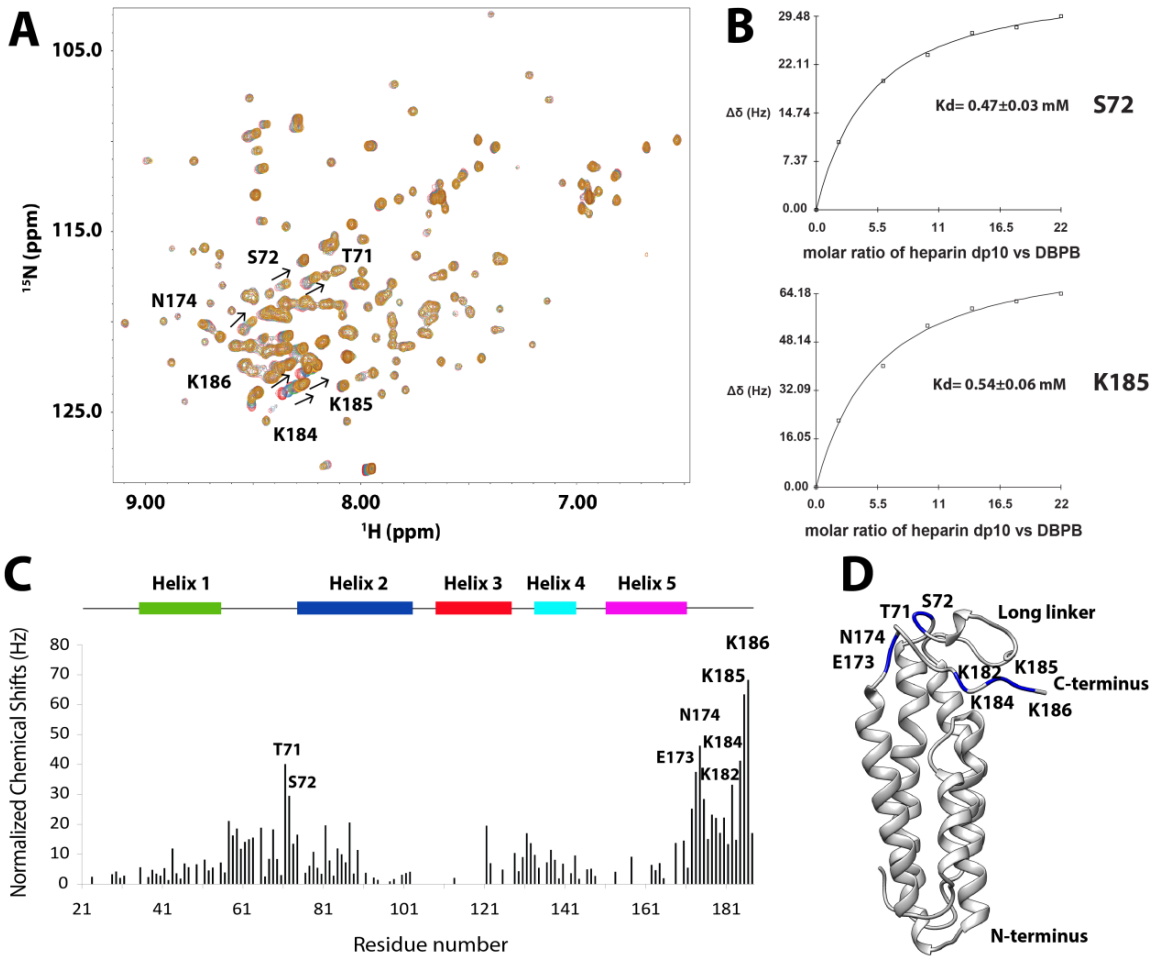

Figure 2.6 DBPB Titration with Heparin dp10.
(A) ^{1}H-^{15}N HSQC overlays of WT B31 DBPB with increasing concentrations of heparin dp10. Signals with large migrations are labeled with their residue numbers and arrows to indicate migration directions. T71, S72, E173, N174, K182, K184, K185 and K186 have the largest migration. Contours are color-coded with increasing concentrations of heparin dp10 (0, 0.2, 0.6, 1.0, 1.4, 1.8 and 2.2 mM). (B) Binding curves of DBPB residues S72 and K185 when titrated with heparin dp10. (C) Residue specific heparin-induced chemical shift changes. Normalized chemical shift perturbations to backbone amide nitrogen and proton by heparin dp10 are displayed. (D) Ribbon conformer of DBPB in the same orientation as in Figure 2.4B with residues showing large perturbations colored blue.

Using chemical shift changes from several residues that showed large perturbations, the dissociation constants (Kd) of the interaction were calculated for the

titrations and the binding curves are shown in Figure 2.6 and Figure 2S1. The Kd of WT DBPB with heparin dp10 is in the 0.5 mM range. On the other hand, DS dp10 showed no sign of saturating the protein even at very high concentrations (Figure 2S1). This indicates DBPB's affinity for DS is weaker than heparin, which is consistent with the GMSA data. DS dp10 did induce broadening of many signals in the HSQC spectrum, suggesting that both affinity and kinetics of the interactions are different compared to heparin dp10. To confirm that signal broadening is the result of dynamic DBPB-DS interactions, we prepared a DBPB sample containing 10 molar equivalents of DS dp10 and measured the contribution of conformational exchange to transverse relaxation of amide nitrogen using CPMG-based NMR relaxation dispersion experiments (31). The result of the CPMG experiments showed that most DS-induced relaxation dispersion can be refocused with a refocusing field strength less than 200 Hz, indicating interactions with DS occur on millisecond time scale. Moreover, the two residues that showed the strongest exchange relaxation are both located on the linker (G55 and T66) near the binding pocket (Figure 2S2). This is consistent with the hypothesis that signal broadening was induced by DS binding to the protein.

Because ligand-induced chemical shift perturbations can indicate the location of binding sites, we systematically tabulated heparin-induced chemical shift changes of backbone amide nitrogen and hydrogen for DBPB residues. Figure 2.6C shows ^{1}H-^{15}N chemical shift changes on a residue specific basis. The most perturbed residues were T71, S72, E173, N174, K182, K184, K185 and K186, most of which are located in the linker between helices one and two as well as the C-terminal tail, implying that those residues

could be involved in GAG binding. Some residues showed unexpected signal intensity increase whereas the majority of residues had reduced peak intensities due to the dilution by heparin dp10 addition. The residues with increased intensities included G63, T66, K69, S72, G73, S183, K184, K185 and K186, which are also in the linker and the C-terminal tail. The increases in their signal intensities are most likely a result of GAG binding-induced reduction in the rate of backbone amide proton exchange with solvent. We also performed similar titrations of DBPB with heparin dp6 ligands to ensure the observed chemical shift patterns are not ligand size and composition dependent. The titration shows heparin dp6 ligands induced identical chemical shift change patterns in DBPB as heparin dp10 (Figure 2S3), confirming DBPB interacts with heparin dp6 in a similar manner as heparin dp10. However, Kd of interaction between DBPB and heparn dp6 was twice as large as the Kd of interaction between DBPB and heparin dp10. This is consistent with the conventional belief that longer heparin ligands have higher affinity for DBPB. Unlike DS, signal broadening induced by heparin was minimal. This indicates interactions of heparin dp10 with DBPB fall in the fast exchange regime on the NMR time scale. However, because two flexible segments, the linker and the C-terminal tail, experienced substantial perturbations in chemical shift values upon binding GAGs, it is possible that GAG binding affects the nanosecond time scale motion of the two domains. To characterize the possible GAG-induced changes in conformational dynamics, we analyzed the dynamics of backbone amide nitrogens of the protein using the Lipari-Szabo model-free approach (38,39). This method represents the magnitude of internal rotational motions using the order parameter S^2, whose values can be estimated with longitudinal

relaxation rates, transverse relaxation rates and steady state heteronuclear NOE (30). An S^2 of zero represents vigorous local motion while an S^2 of one represents complete rigidity. T_1, T_2 and ^1H-^{15}N NOE of the backbone amide nitrogen atoms were measured and fitted using the program relax (29) to obtain order parameters S^2 for these atoms. The data showed the long linker and the C-terminal tail are highly dynamic (Figure 2S4), but no significant change in order parameters was detected even after the addition of 10 molar equivalents of heparin dp10. These observations show heparin dp10 has no significant effects on DBPB's dynamics. Similar observations were also made for DBPA (19,40). Finally, although chemical shift mapping is the most popular technique for determining ligand-binding sites, artifacts can occur if protein undergoes significant conformation changes after binding the ligand. To unambiguously identify residues that are close to bound GAGs, we probed DBPB with DS dp12 ligands functionalized with the paramagnetic nitroxide radical TEMPO. The unpaired electron in the paramagnetic tag generates heterogeneous magnetic field and induces increased longitudinal and transverse relaxation rates of spins in the vicinity. The phenomenon, known as paramagnetic relaxation enhancement (PRE), leads to decreases in signal intensities of nearby residues in a distance-dependent manner such that atoms close to the paramagnetic center suffer greater loss of signal than atoms far away (41). Figure 2.7A shows the overlays of ^1H-^{15}N HSQC spectra of a sample containing 0.15 mM WT B31 DBPB and 1.2 mM paramagnetic DS dp12 before and after the radical was reduced with ascorbic acid. The spectra revealed large increases in signal intensities of several residues upon the reduction of the radical, indicating that they are close to the paramagnetic center.

These residues include L57, E59, G73, G74, Q83, I131, Q158, Q162, and N171. Figure 2.7B shows the location of these perturbed residues. Similar to the results of chemical shift perturbation analysis, most TEMPO-perturbed residues are also found in the linker, the C-terminus and the basic patch. This is direct evidence that those regions are involved in GAG binding.

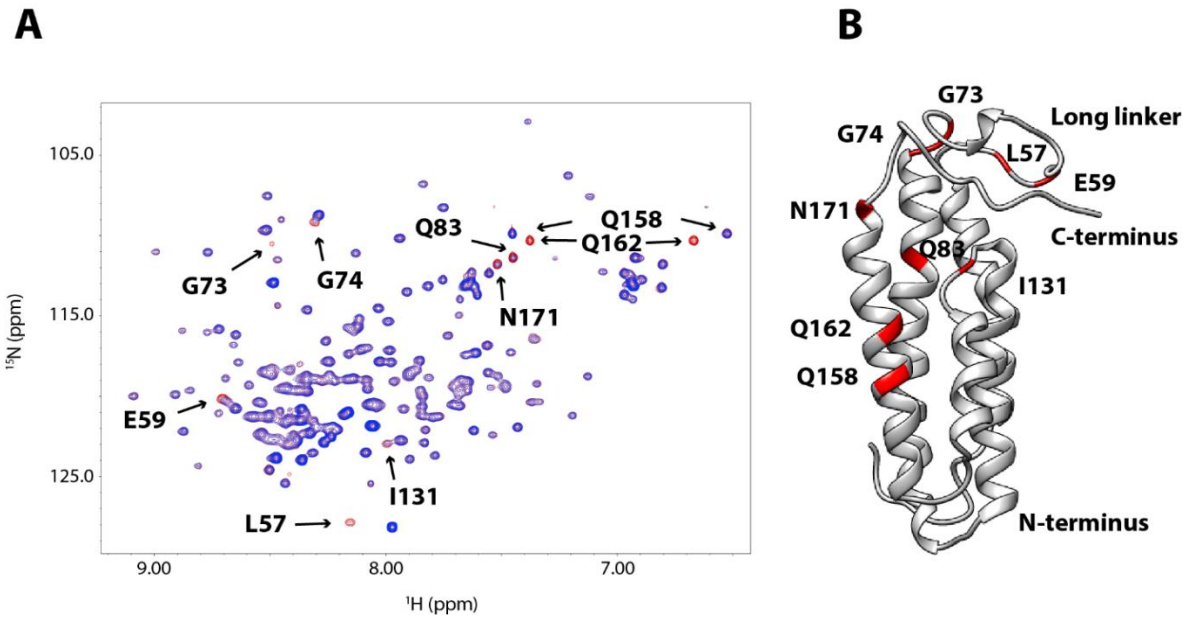

Figure 2.7 PRE Perturbation of DBPB by Paramagnetically Labeled DS dp12.
(A) ^{1}H-^{15}N HSQC overlays of WT B31 DBPB with 8 molar equivalents of TEMPO-labeled DS dp12. HSQC spectrum before the radical is reduced is shown in blue. HSQC spectrum of the protein after reduction of the radical is shown in red. Residues showing prominent PRE perturbations are indicated. They are L57, E59, G73, G74, Q83, I131, Q158, Q162 and N171. (B) Ribbon representation of DBPB in the same orientation as in Figure 2.4B with TEMPO-perturbed residues colored red.

3, Determination of DBPB's GAG-binding sites through mutagenesis

The DBPB structure identifies several possible GAG-binding sites. In order to study the contributions of these residues to GAG binding, WT and mutant DBPBs lacking one of the proposed sites were prepared and their heparin and DS affinities were

measured. Previous studies suggested that three lysine residues (K82, K163 and K170) are crucial to the binding of DBPA with GAGs (18,42). As shown in Figure 2.2, only two of the residues (K81 and K169) are conserved in DBPB. However, DBPB contains an additional arginine residue at position 78, which is located on the same face of helix 2 as K81 and K169 and able to synergistically participate in GAG binding with these residues. Besides these basic amino acids, chemical shift mappings showed that two other lysines, K65 and K69 in the long linker of DBPB, experienced large perturbations upon GAG binding, implying that these two lysines are potentially critical to DBPB's GAG binding activity. Based on these observations, three mutants, K65S/K69S, R78S/K81S and K81S/K169S, were prepared. The fact that DBPB C-terminal tail is rich in lysines and is the most perturbed domain in chemical shift mapping implies that the C-terminal tail might be crucial to GAG binding. Therefore, mutants lacking the last four residues ($DBPB_{21\text{-}183}$) or having them mutated from lysines to serines ($^{184}SSSS^{187}$) were also prepared.

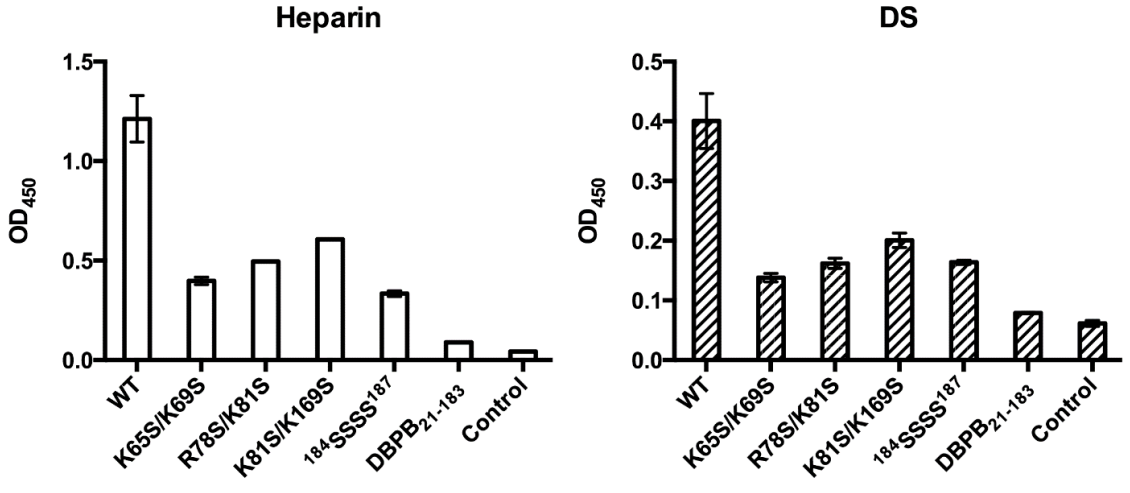

Figure 2.8 Impact of Mutations on DBPB's Heparin and DS Affinities Evaluated

using Immobilized Heparin or DS ELISA.

To evaluate the contributions of the proposed sites to GAG bindings, the GAG affinities of the mutants were characterized with NMR-monitored titrations, GMSA and ELISA. First, we measured different DBPB mutants' affinities for intact heparin and DS using ELISA assays with immobilized heparin and DS. As shown in Figure 2.8, the assays revealed the interactions of all mutants with native GAG chains were severely diminished. These results confirm the basic amino acids identified are crucial to GAG binding. We also studied the effect of the mutations on DBPB's interactions with sized-defined GAG fragments using GMSA and NMR. Results of the GMSA are shown in Figure 2.9. In the assay, WT DBPB shifted almost all heparin dp6 fragments. In contrast, the two C-terminus mutants failed to shift any GAG fragments while R78S/K81S and K81S/K169S mutants induced shifts of only a small fraction of GAGs. K65S/K69S induced a significant amount of fragment migration, but the fraction of the shifted fragments was still much less than that of the WT DBPB. Similar results were obtained using a DS-based GMSA (Figure 2.9). These results are in qualitative agreement with the ELISA data, and show K65 and K69 are not as important as other clusters of basic amino acids. Quantitative evaluations of binding affinities were also carried out by titrating the mutants with heparin dp10 (Figures 2S5 & 2S6). The dissociation constants (Kd) derived from the titrations are shown in Table 2.2. The Kds are consistent with the result of GMSA in Figure 2.9. Specifically, WT DBPB's Kd is smaller than all mutants, while the Kds of K65S/K69S, R78S/K81S and K81S/K169S mutants all showed varying degrees of increase compared to the WT protein. In contrast, two C-terminal mutants, ^{184}SSSS^{187}

and $DBPB_{21-183}$, showed no significant chemical shift migrations, suggesting their GAG affinities are severely attenuated (Figures 2S5D and 2S5E). Based on the results, we believe that the last four lysine residues are the most important GAG binding site in DBPB.

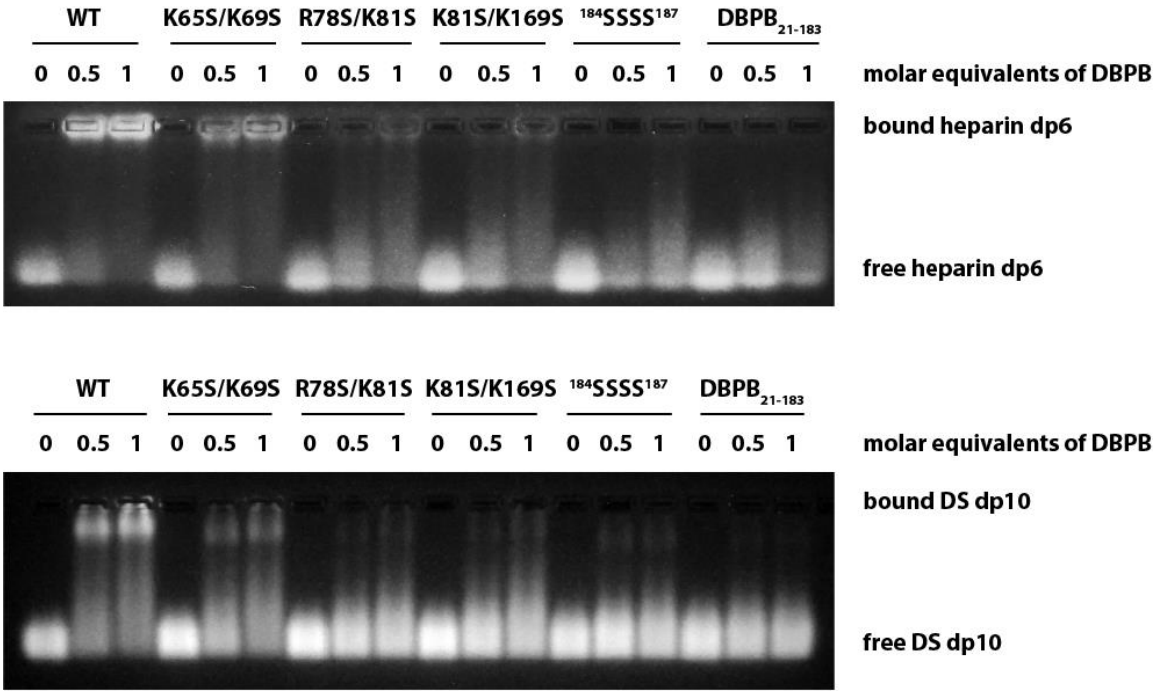

Figure 2.9 GMSA Evaluation of the Effects of Mutations on DBPB's Heparin and DS Affinity.

4, GAG affinity comparisons between DBPA and DBPB

To determine whether there are differences in GAG affinities of DBPA and DBPB, we probed their interactions with intact long chains of heparin and DS using ELISA. Our data showed B31 versions of DBPA and DBPB have similar affinities for both heparin and DS in ELISA (Figure 2S7A). This shows DBPB can be as important a GAG adhesin as DBPA. GMSA assay carried out on B31 DBPA and DBPB using size defined heparin dp6 also confirmed the similarities in their GAG affinities (Figure 2S7B).

Table 2.1 Structural Statistics for the Ensemble of DBPB Structures.

no. of NOE-based distance constraints	
total	1635
intra-residue (i=j)	484
sequential (|i-j|=1)	477
medium range (1<|i-j|<5)	389
long range (|i-j|≥5)	285
NOE constraints per restrained residue [a]	10.0
no. of RDCs	
H-N	93
N-C	91
no. of dihedral angle constraints	240
total no. of structures computed	50
no. of structures used	10
constraint violations [b]	
no. of distance violations per structure	
0.1~0.5 Å	37
>0.5 Å	0.9
no. of dihedral angle violations per structure	
>10°	0.5
no. of RDC violations per structure	
>1 Hz	1.4
rmsd	
all backbone atoms	0.7 Å (ordered [c])
all heavy atoms	1.2 Å (ordered [c])
Ramachandran plot summary from Procheck [d] (%)	
most favored regions	92.4
additionally allowed regions	7.4
generously allowed regions	0.2
disallowed regions	0.0

[a] There are 161 residues with conformational restricting constraints.
[b] Calculated for all constraints for the given residues, using a sum over r^{-6}.
[c] Residues 34-54, 74-103, 108-128, 134-143, and 150-171.
[d] Residues 30-57, 67-69, 75-130, 134-144, and 150-170.

2.5 Discussion

In this work, we determined the solution structure of DBPB from strain B31 of *B. burgdorferi* and determined its GAG binding residues. The topology of DBPB is similar to that of DBPA. Both have five helices and two unstructured segments (10,18). Despite

the similarities, their structures differ in several significant ways. Specifically, the C-terminal helix of DBPB is shorter than the corresponding helix in DBPA, leading to a far longer C-terminal tail that is unrestricted by any disulfide bond. The C-terminus is also distinguished from its DBPA counterpart by the large number of lysines found at its end. Most results from this study indicate these C-terminal basic residues contribute significantly to the GAG affinity of DBPB. In particular, the C-terminal residues (K184, K185 and K186) showed the largest changes in chemical shifts when DBPB was titrated with heparin dp10 and heparin dp6 (Figures 2.6 and 2S3). Removing the last four residues or mutating them to serine also attenuated DBPB's affinity greatly. All these show the C-terminus is an important GAG-binding site in DBPB. Although B31 DBPA did have two basic residues close to its C-terminus, previous study indicated that their impact on GAG affinity of DBPA was modest (19). We believe the location of these basic amino acids (none are located at the very terminus) in DBPA and the presence of the disulfide bond in DBPA may have restricted GAG ligands' access to the C-terminus of B31 DBPA. However, DBPA sequence heterogeneity is large, and C-termini of DBPAs from strain VS461 of *Borrelia afzelii* and strain PBr of *Borrelia garinii* have been shown to play a crucial role in their GAG binding activity (13,40), setting the precedence for the involvement of C-termini in GAG binding. What is different between DBPB and all versions of DBPA studied so far is that the canonical GAG binding site made up of basic amino acids from helices 2 and 5 do not appear to contribute as much to GAG binding in DBPB as it did in DBPA. This might be because the number of basic amino acids in DBPB's canonical GAG-binding pocket is half that of DBPA. In

particular, both K163 and R166 of B31 DBPA do not have equivalent basic residues in DBPB. The fact that the BXBB motif found in the linker of B31 DBPA is also missing in DBPB means the linker cannot contribute to GAG binding either. This may have further accentuated the importance of C-terminus of DBPB in GAG binding.

Table 2.2 Kd Values of DBPB Interactions with GAG Fragments.
WT and mutant DBPBs were titrated with heparin dp10 and DS dp10. Kds were calculated based on S72 and K185 for DBPBs.

	Kd (mM)	
	S72	K185
WT	0.47 ± 0.03	0.54 ± 0.06
K65S/K69S	0.90 ± 0.12	0.88 ± 0.06
R78S/K81S	1.04 ± 0.26	1.16 ± 0.18
K81S/K169S	1.24 ± 0.35	1.22 ± 0.12
^{184}SSSS^{187}	------	------
$DBPB_{21-183}$	------	------

The flexible nature of the C-terminus means GAG's interaction with the C-terminus most likely lacks precise geometric constraints and multiple binding conformations are possible. This is consistent with the PRE-perturbation data, which showed the reducing end of the ligand can be located in several locations. It also agrees with the smaller heparin-induced chemical shift perturbations observed for DBPB since heterogeneity in binding conformation are believed to reduce the magnitudes of chemical shift perturbations.

Of the five mutants investigated for their GAG-binding activity, all showed lower GAG affinities than WT DBPB. In particular, K65S/K69S, R78S/K81S and K81S/K169S mutants exhibited significant decreases in their affinities for both heparin and DS size-defined ligands, while $DBPB_{21\text{-}183}$ and $^{184}SSSS^{187}$ mutants showed no binding to these short GAG fragments. These data indicate that all three clusters play a role in promoting GAG binding, but the C-terminus is especially critical. Interestingly, in the ELISA assay, the $^{184}SSSS^{187}$ mutant showed slightly higher binding for native GAG polysaccharides than the $DBPB_{21\text{-}183}$ mutant. It is possible that serines at the C-terminal tail are capable of mediating minor GAG binding through hydrogen bond interactions, while the truncation of the C-terminus completely attenuates the interaction. One factor that could have enhanced the importance of the C-terminus in GAG binding may be its accessibility to ligands. Specifically, although dynamic, the location of linker means it can still pose a significant barrier to interactions between GAGs and the basic pocket. The surface exposed nature of the C-terminus means it is more likely to interact with GAGs than basic residues in the pocket, therefore exerts a strong influence on GAG affinity of the protein. In fact, B31 DBPB is not the only DBP with important GAG-binding in its C-terminus. The C-terminus of DBPA from *Borrelia afzelii* strain VS461 is also crucial to the protein's GAG affinity (13). Despite its importance in facilitating GAG-binding, the C-terminal tail showed no sign of perturbation in the PRE experiment. We believe this is possible because only the reducing end of DS dp12 is labeled with TEMPO, and the C-terminal tail may interact mainly with the non-reducing ends of the GAG fragments, allowing it to be unaffected by the paramagnetic tag.

CHAPTER 3

BACKBONE ASSIGNMENT OF INTEGRIN α_M I-DOMAIN

3.1 Abstract

Integrin is a family of cell surface receptors that primarily bind extracellular matrix (ECM) components, allowing cells to migrate and transform. Consisting of α and β subunits, the heterodimers undergo global conformational rearrangements during activation that dramatically increase their affinity for their ligands. $\alpha_M\beta_2$, or Mac-1, has a broad ligand recognition spectrum, making it the most promiscuous member of the protein family. Recent studies also indicated Mac-1's ligand binding mechanism is unique among integrins. α subunit of Mac-1 contains an α I-domain, which is the primary ligand binding site. Crystal structure of α_M I-domain reveals a Rossmann fold, common to all α I-domains. However, the reason behind α_M I-domain's ability to bind a diverse set of ligands is still not clear. We are interested in investigating the ligand-binding mechanism of α_M I-domain. Present work focuses on NMR backbone assignment and biophysical characterizations of α_M I-domain, including pH stability, Mg^{2+} bindings and homodimeric interactions.

3.2 Introduction

Half of the 18 α variants contain α I-domains. In fact, before the whole extracellular structure was solved, the structures of individual integrin domains including α_M I-domain were already determined (1-3). α I-domain, also known as a von Willebrand factor A domain, usually contains 200 amino acids. In α I-domain containing integrins, α I-domain is the primary ligand binding site. Left panel of Figure 3.1 is the crystal

structure of integrin α_M I-domain. Like other α I-domains, α_M I-domain adopts a Rossmann fold with 6 central β strands surrounded by 7 α helices on the outside (1). α I domain is anchored to the β propeller on the bottom surface with N and C linkers. On the top surface is an important site known as metal ion dependent adhesion site (MIDAS). Many divalent metal ions, such as Ca^{2+}, Mg^{2+} and Mn^{2+}, bind to MIDAS, with Mg^{2+} being the physiological cation (5). The divalent cation is coordinated by side chains of five residues in MIDAS. They all reside on loops: 1, three residues (Asp, Ser and Ser in a conserved motif DXSXS) can be found on the β1-α1 loop; 2, fourth residue (Thr) is located on the α3-α4 loop; 3, the last residue (Asp) is on the β4-α5 loop. Metal coordinating residues in MIDAS are displayed in the middle panel of Figure 3.1. Other than these residues, water molecules also provide coordinating oxygens (4). It has been established that MIDAS is important for ligand bindings in the following respects: 1, the divalent cation is necessary for ligand binding and acts as the bridge between α I-domains and ligands through metal coordination; 2, MIDAS residues that do not coordinate metals are also required for ligand recognition (4). Just like the global structural rearrangement of integrin, α I-domain also undergoes conformational change upon activation. Upon activation, metal coordinating loops in MIDAS rearrange, accompanied by a large shift in the β6-α7 loop and the characteristic 10 Å axial movement of α7 helix, creating a conformation with high affinity for ligands (open). This α7 helix movement transmits α I-domain conformational signals to the rest of integrin molecules. Right panel of Figure 3.1 displays the conformational changes within α_M I-domain in close/low affinity and open/high affinity states.

Integrin $\alpha_M\beta_2$ (Mac-1 or CD11b/CD18) is the most dominant integrin on myeloid cells. Mac-1 is responsible for adhesive activities of leukocytes (6). Although Mac-1 expression on neutrophils and monocytes is upregulated in response to inflammation stimuli, the increase in ligand interactions is largely due to enhanced affinity of a small fraction of Mac-1 rather than higher density of Mac-1 on cell surface (7-9). Most of ligand activities in Mac-1 are contributed by α_M I-domain. What's unique about Mac-1 is its broad ligand binding specificity. The number of reported Mac-1 ligands is over 40 and still increasing, making it the most promiscuous member of the integrin family (10). Many ligands of Mac-1 are ECM components, such as fibrinogen (11) and complement C3 cleavage fragment C3bi (12). The broad ligand range of Mac-1 has led to questions of binding motifs recognized by Mac-1. Ugarova et al. showed that Mac-1 has high affinity for peptides that contain high proportions of basic amino acids (10). As cationic ligands are highly positively charged and often lack acidic residues to coordinate divalent metal ions in MIDAS, the classical mechanism of α I-ligand interaction may not apply for cationic ligands. Specifically, in the classical Mg^{2+} dependent ligand binding mechanism, one coordinating residue in MIDAS must leave and be replaced by an acidic amino acid from the ligand. Mg^{2+} serves as the bridge between MIDAS of α I-domains and ligands. Given the broad and diverse ligand spectrum of Mac-1, and the fact that many of the ligands are free of acidic amino acids, it is possible that Mac-1 recognizes ligands via multiple mechanisms.

The following chapters will explore the ligand binding mechanism and dynamics of integrin α_M I-domain using solution NMR techniques. Information on ligand binding

and conformation change is inferred mostly from changes in ^{15}N-edited HSQC spectrum of α_M I-domain. To correctly interpret the data, bonded ^{15}N and ^{1}H atoms that give rise to the signals in the spectrum must be determined. However, there is currently no NMR study of α_M I-domain and assignment of these signals has never been done. Therefore, this chapter will focus on determining NMR chemical shift assignments of backbone atoms in α_M I-domain as well as biophysical characterizations of integrin α_M I-domain, such as Mg^{2+} bindings and pH stability. Our experiments also unexpectedly revealed presence of homodimers formed as result of interactions between termini of the protein and the MIDAS, which are mitigated only when both termini are shortened.

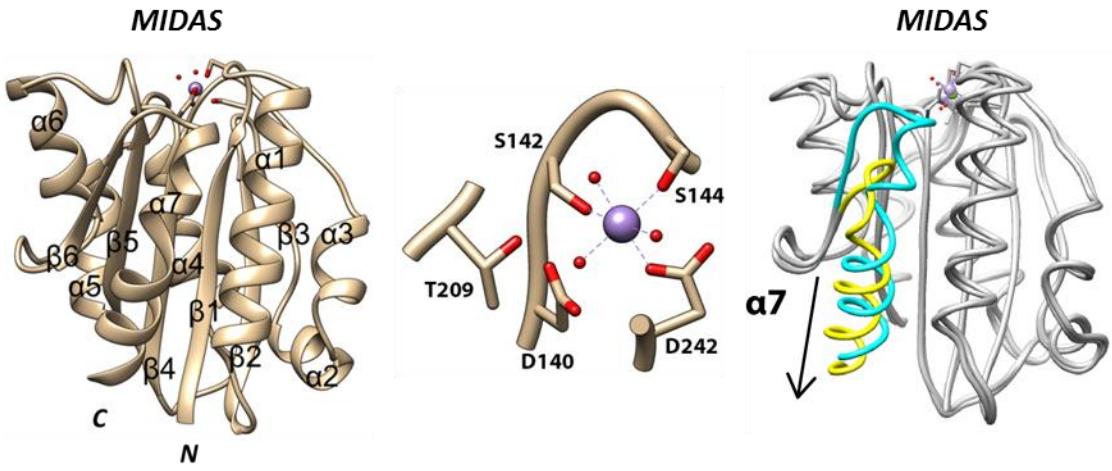

Figure 3.1 Integrin α_M I-domain Structure.
(Left), ribbon structure of α_M I-domain (pdb: 1jlm) with Mn^{2+} in MIDAS. Secondary structures are labeled. (Middle), metal coordinating residues in MIDAS of closed α_M I-domain. (Right), integrin α_M I-domain conformations in low and high ligand affinity states. Segments with the most significant shift are colored yellow in closed/low affinity state (pdb: 1jlm) and cyan in open/high affinity state (pdb: 1ido). The rest of α_M I-domain is colored grey.

3.3 Materials and Methods

1, Integrin α_M I-domain expression and purification

The open reading frame (ORF) of the wild type/WT (Q119-E333) α_M I-domain was cloned with His-tagged ubiquitin at 5' end into the pHUE vector (13). Truncated versions were designed as N-truncated (E131-E333), C-truncated (Q119-T324) and N/C-truncated (E131-T324). The plasmid was transformed into BL21 (DE3) cells for expression in M9 medium at 37 °C until an OD_{600} of 0.8 is reached. 0.5 mM IPTG was added into the expression mixture and cultured overnight at room temperature (23°C) before harvest next day. M9 medium was isotopically supplemented with $^{15}NH_4Cl$ and/or ^{13}C glucose. After harvest, cells were resuspended with lysis buffer (20 mM sodium phosphate, 0.5 M Nacl 10 mM imidazole, 5% glycerol, 0.01% NaN_3), then treated with 1mg/mL lysozyme for ~ 25 minutes before sonication. After sonication, mixture was centrifuged and supernatant was collected. The supernatant was applied on a 5mL HisTrap column (GE Life Sciences) during Ni affinity chromatography. To elute bound protein off the column, an imidazole gradient (ranging from 35 to 500 mM) was applied at a flow-rate of 3 mL/min. Fractions containing bound α_M I were buffer exchanged to 25 mM Tris and 100 mM NaCl (pH 8.0) for overnight digestion with USP2 deubiquitinating enzyme (1:20 molar ratio) (13). After cleavage, digested α_M I-domain was collected on a second Ni column. Finally, collected fractions were applied onto a Superdex 75 size exclusion column (GE Healthcare Life Sciences, Little Chalfont, UK). Protein purity is confirmed on a SDS-PAGE gel.

2, NMR data acquisition and backbone assignment

All NMR data were recorded on Bruker Ultra-Shield 600 MHz and 850 MHz spectrometers (Bruker Instruments, Inc., Bellerica, MA, USA), both equipped with cryo-probes. NMR samples contain ~ 0.15-1 mM protein in 20 mM HEPES and 100 mM NaCl (pH 7.0). For backbone assignment, HNCACB, HNCOCACAB, HNCO and HNCACO spectra were collected on $^{2}H/^{13}C/^{15}N$ labeled proteins. HNCA, HNCOCA spectra were collected on $^{13}C/^{15}N$ samples. To assist assignment, CCCONH and ^{15}N-edited NOESY spectra were also acquired. All NMR data were processed and analyzed with NMRPipe (14) and NMRView (15) respectively. Chemical shift information of Cα, Cβ, and backbone HN, N and CO were used in chemical shift index (CSI) analysis using developers' server (http://csi3.wishartlab.com/cgi-bin/index.php) (16). Mg^{2+} was added in series to 150 μM of ^{15}N integrin α_M I-domain for concentrations ranging from 0 to 50 mM Mg^{2+}.

3, Paramagnetic relaxation enhancement (PRE)

G321C mutagenesis was performed on N-truncated (E131-E333) and N&C-truncated (E131-T324) to introduce cysteine for paramagnetic labeling while C-truncated (Q119-T324) has C128 on its N terminus. MTSL, (1-Oxyl-2,2,5,5-tetramethylpyrroline-3-methyl) methanethiosulfonate (Santa Cruz Biotechnology), was dissolved in DMSO at ~0.5 M as stock solutions. Before MTSL labeling, 10mM DTT is added to purified α_M-I domain and then the mixture is applied onto HiTrap Desalting column (GE Life Sciences) to remove DTT and obtain free cysteine for high labeling efficiency. 10 molar equivalents of MTSL were added to the protein solution and incubated at room temperature overnight. The next day, the mixture is then buffer exchanged to remove

unreacted free MTSL and then concentrated for NMR studies. 1D ^{1}H NMR spectra were performed to verify MTSL labeling.

For PRE experiments, ^{1}H-^{15}N HSQC spectra (oxidized) were collected for a ~300 uL sample of 300 μM ^{15}N MTSL-labeled α_M I domain alone or equal molar (150 μM) mixture of ^{15}N α_M I and MTSL-labeled α_M I. Ascorbic acid was added in 5:1 molar ratio to reduce the paramagnetic radical and another ^{1}H-^{15}N HSQC spectra (reduced) were collected.

4, Circular dichroism (CD) spectroscopy

CD spectra were collected on a temperature controlled JASCO J710 spectropolarimeter. CD measurements were performed for 20 μM α_M I domain in 20 mM HEPES, 100 mM NaCl at pH levels of 4.0, 5.0, 6.0 and 7.0. CD data were recorded at 20 °C in the far- UV region (200-250 nM) with 100 mDeg sensitivity, 0.5 nm data pitch and scanning speed of 50 nm/min. Another sample containing pH 7.0 buffer only was also used as the negative control.

3.4 Results

1, Backbone Assignment

The backbone assignment was made through a combination of three dimensional (3D) NMR experiments. Cα and Cβ chemical shift values associated with each signal in the ^{15}N HSQC spectrum are extremely informative as not only do they provide a way to connect consecutive residues but they also help in narrowing down amino acid types. Therefore, HNCACB and HNCOCACB spectra were acquired for ^{2}H,^{13}C,^{15}N-labeled α_M

I-domain, together with HNCO and HNCACO spectra. Figure 3.2A and B show HNCACB, HNCOCACB, HNCO, HNCACO spectra of D273, A274 and F275. Cβ of A274 is a methyl carbon therefore its value is usually below 20 ppm. G272 has no Cβ and its Cα value is normally close to 45 ppm. By matching Cα and Cβ chemical shifts of signals from both HNCACB and HNCOCACB, we were able to assign over 70 % of residues in α_M I-domain. However, a number of residues were not assigned, mostly in β strand regions. The missing assignments are most likely due to weak signals. In particular, careful examination of ^{1}H-^{15}N heteronuclear single quantum coherence (HSQC) spectra of ^{2}H,^{13}C,^{15}N-labeled and ^{15}N-labeled protein samples revealed that a number of peaks are missing or considerably weaker in the deuterated sample compared to the undeuterated sample (Figure 3.4). This means that some backbone amide deuterons have slow exchange with solvent water, therefore is not observable in the ^{15}N HSQC spectrum. To overcome the hurdle, undeuterated ^{13}C,^{15}N-labeled α_M I-domain was prepared. HNCA and HNCOCA were recorded because they provide Cα information with higher sensitivity, which assist assignment when HNCACB and HNCOCACB of the deuterated sample do not yield satisfactory data quality. Figure 3.2C shows HNCA and HNCOCA spectra of residues in β4 strand. Signals of those residues were not observed in NMR spectra of deuterated samples.

So far, around 90% of observable backbone H-N peaks were assigned. Figure 3.3 displays ^{15}N HSQC spectra of α_M I-domain (E131-T324). Assigned peaks are marked with amino acid types and residue numbers. Unassigned residues are concentrated in two segments, α3-α4 loop and α4 helix. This is likely to be a result of the inherent dynamics

of the protein, which causes line broadening of signals. Chapter 5 will explore the dynamics of integrin α_M I-domain using relaxation dispersion experiments. To predict secondary structure of current α_M I domain, Cα, Cβ, and backbone CO, HN and N chemical shifts were combined as inputs for chemical shift index (CSI) analysis (16). The result, shown in the lower panel of Figure 3.3, suggests that the construct used here displays a pattern characterized by interleaved β strands and α helices, known as Rossmann fold (1). The secondary structure organization is consistent with the crystal structure of α_M I-domain (pdb: 1jlm) (17). Therefore, the protein should adopt a similar structure in solution.

Hydrogen/deuterium exchange is also useful in providing insights into protein structures. Figure 3.4 illustrates overlays of ^{1}H-^{15}N HSQC spectra of ^{15}N-labeled and ^{2}H,^{13}C,^{15}N-labeled α_M I-domain. Residues whose amide hydrogens are protected from solvent exchange are also mapped onto the ribbon structure. When comparing the spectra, it was instantly noticed that some peaks are only observed or have considerably higher signal intensities in undeuterated samples. This implies that these residues are protected from exchange with solvent hydrogen due to intramolecular hydrogen bond network or/and lack of solvent exposure. The protected residues are primarily located in β1, β2, β4, and β5 strands. The position of protected residues is consistent with the structure of α_M I-domain in which the central β strands are surrounded and shielded from solvent by surrounding α helices (17).

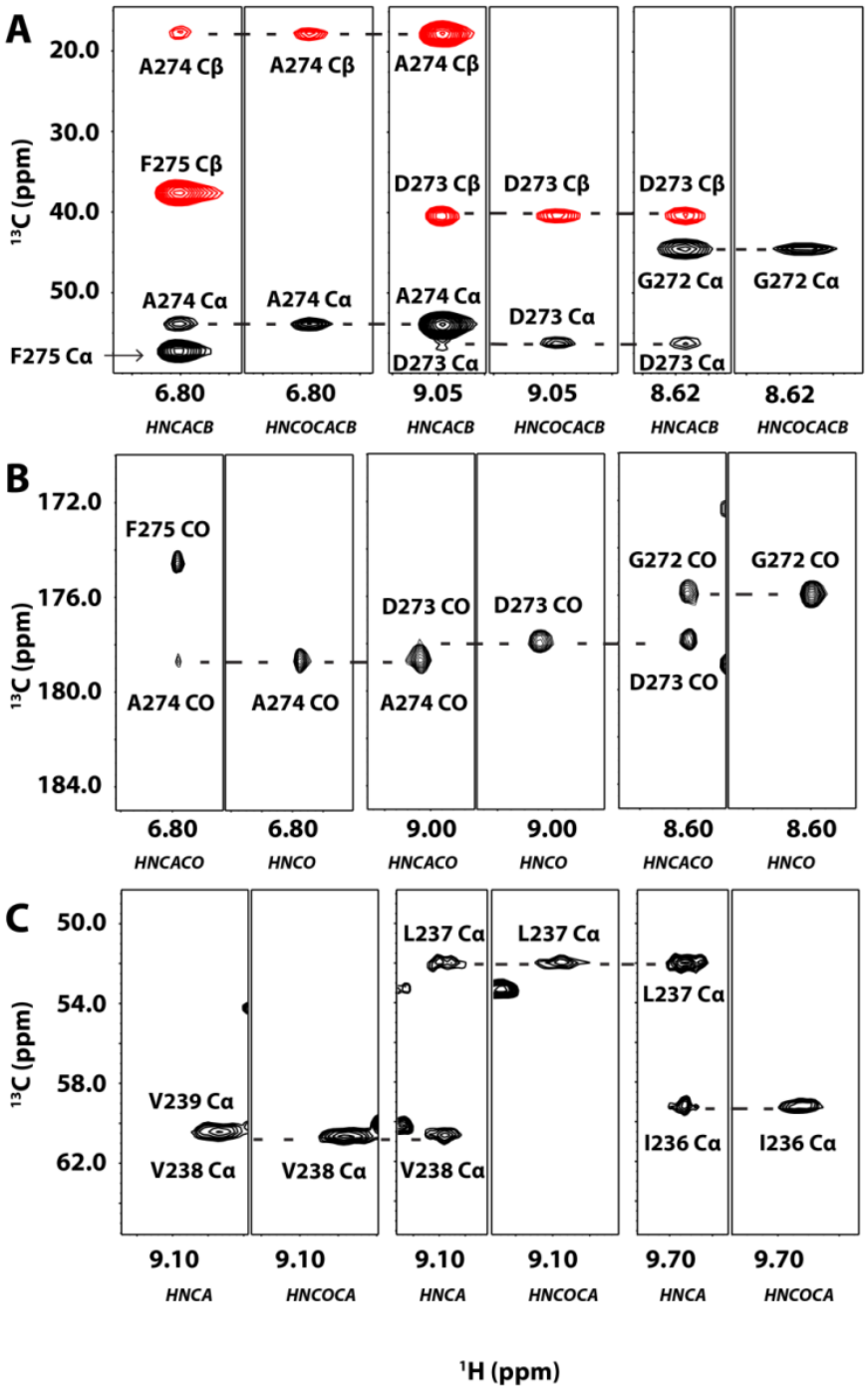

Figure 3.2 3D NMR Spectra for Backbone Assignment of αM I-domain.
(A), HNCACB and HNCOCACB spectra for F275, A274 and D273 in β5-α6 loop. (B), HNCO and HNCACO spectra for F275, A274 and D273 in β5-α6 loop; (C), HNCA and HNCOCA spectra of V239, V238 and L237 in β4 strand.

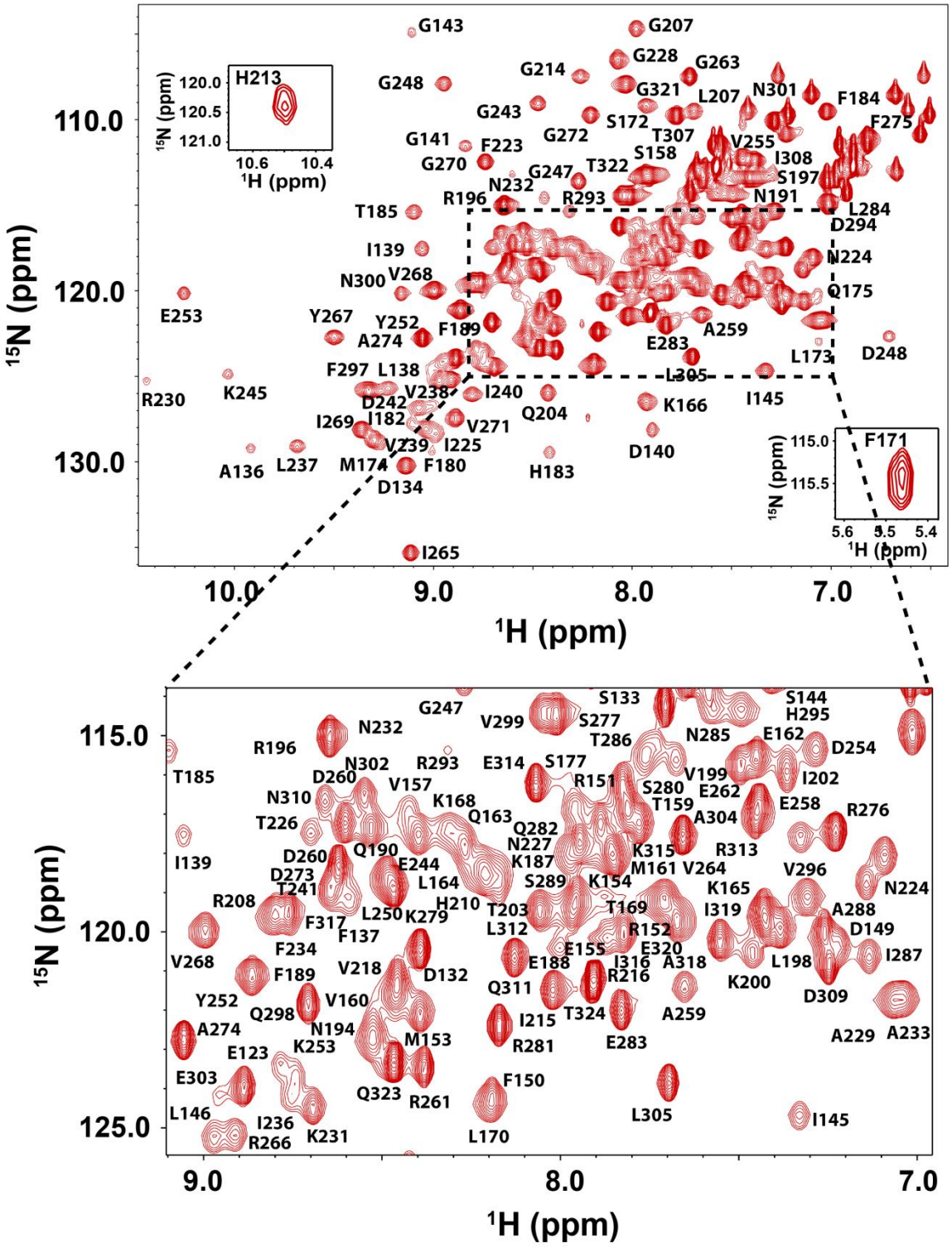
G143
G207
G228
G263
G214
G248
G321
L207
N301
F184
G243
S172
F275
G141
F223
G272
T307
V255
G270
S158
I308
G247
T322
S197
N232
R196
R293
N191
T185
L284
D294
I139
N224
N300
V268
Q175
E253
Y267
Y252
F189
A259
A274
E283
L173
D248
F297
L138
L305
R230
K245
V238
I240
I145
D242
Q204
K166
I269
I182
V271
I225
D140
V239
A136
L237
M174
F180
H183
D134
I265
H213
F171
^{15}N (ppm)
^{1}H (ppm)
S133
S144
G247
H295
N232
V299
S277
N285
E162
R196
T286
D254
N302
R293
E314
S177
T185
R151
V199
I202
D260
V157
S280
E262
N310
K168
T159
E258
Q163
A304
R276
T226
Q282
N227
D260
Q190
K315
R313
I139
E244
K187
M161
V264
V296
D273
L164
S289
K154
K165
N224
T241
H210
T203
T169
I319
A288
R208
L250
K279
L312
R152
D149
F317
F137
E155
E320
F234
I316
A318
I287
V268
E188
L198
F189
V218
D132
R216
K200
Q311
D309
Y252
V160
T324
A259
Q298
I215
N194
A274
M153
R281
E283
A229
A233
E123
K253
F150
E303
Q323
R261
L305
L146
I145
I236
L170
R266
K231
^{15}N (ppm)
^{1}H (ppm)

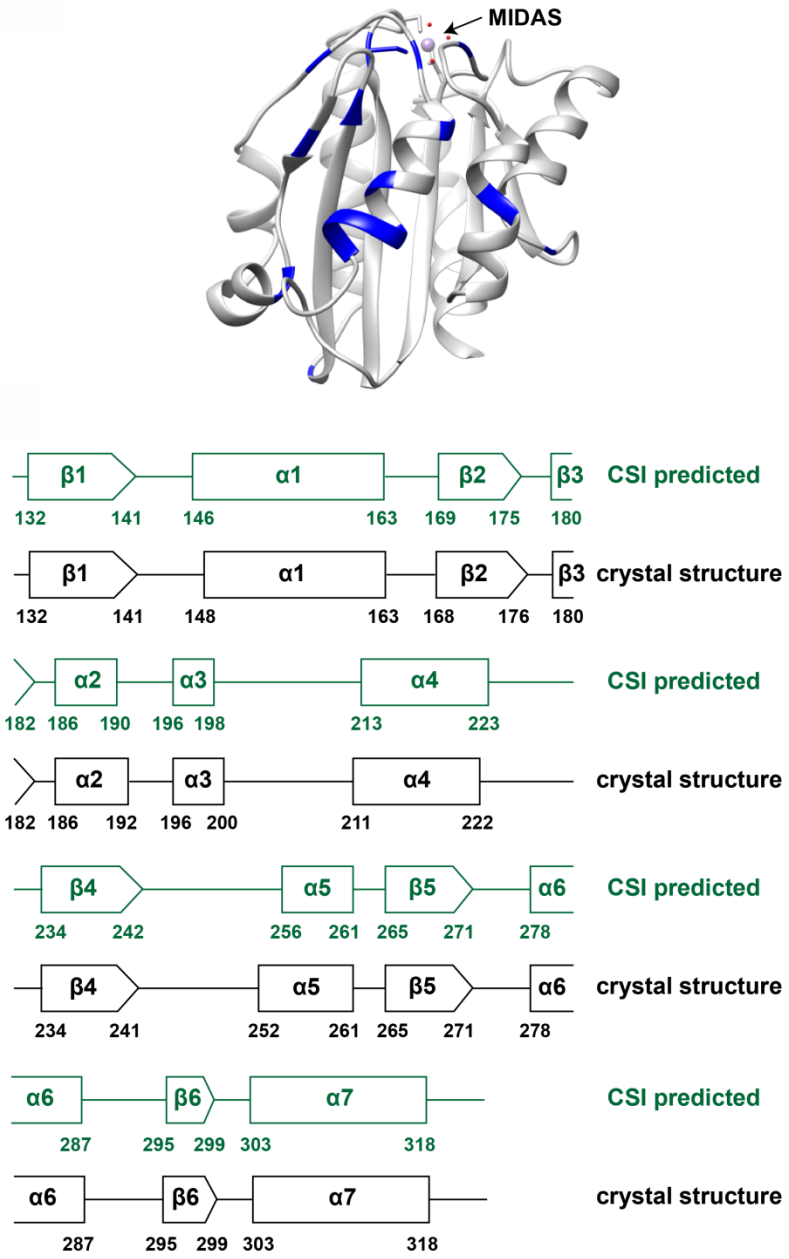

Figure 3.3 Backbone Assignment of Integrin α_M I-domain.
Upper panel: ^{1}H-^{15}N HSQC spectra of integrin α_M I-domain (E131-T324). The over-crowded region is enlarged for better presentation of peaks and assignments. Middle panel: unassigned residues are colored blue in α_M I-domain ribbon structure (pdb: 1jlm). Lower panel: Chemical shift index (CSI) analysis. CSI-predicted secondary structures are plotted (green) above secondary structures (black) of the α_M I-domain crystal structure (pdb: 1jlm). Positions of α helices (rectangle boxes) and β strands (pentagon boxes) are labeled with residue numbers.

In the initial process of backbone assignment, several peaks were found to possess similar Cα and Cβ chemical shift values. The CCCONH spectrum indicates that these peaks also share similar chemical shift values for other side chain carbon atoms. CCCONH not only reveals amino acid type but also provides definitive proof that some of these signals represent two states of the same residue. These residues with double resonances are all located in the N terminus: K120, E123, A124 and G127. The appearance of two distinct populations that are well resolved in NMR spectra is characteristic of chemical exchange on slow timescales (18). However, such dynamics was not observed for C-terminal residues or residues close to other prolines. The reason for the resonance doubling at the N-terminus is revealed by the CCCONH spectra of residue P122 as shown in Figure 3.5. The two states of P122 have very distinctive chemical shift patterns that represent cis- and trans- isomers of the proline. The trans-isomer has higher signal intensity than the cis-isomer, in all 2D and 3D NMR spectra, suggesting a biased trans-isomer population. The "double-state" residues (K120, E123, A124 and G127) are located around P122 and also display unequal signal intensities, indicating that they are the results of P122 isomerization. Such proline isomerization on the slow timescales has been reported before in protein NMR studies (19,20). To our best knowledge, this is the first report of proline isomerization in integrin α I-domains. The lack of proline could explain why this slow dynamics is not present in the C terminus.

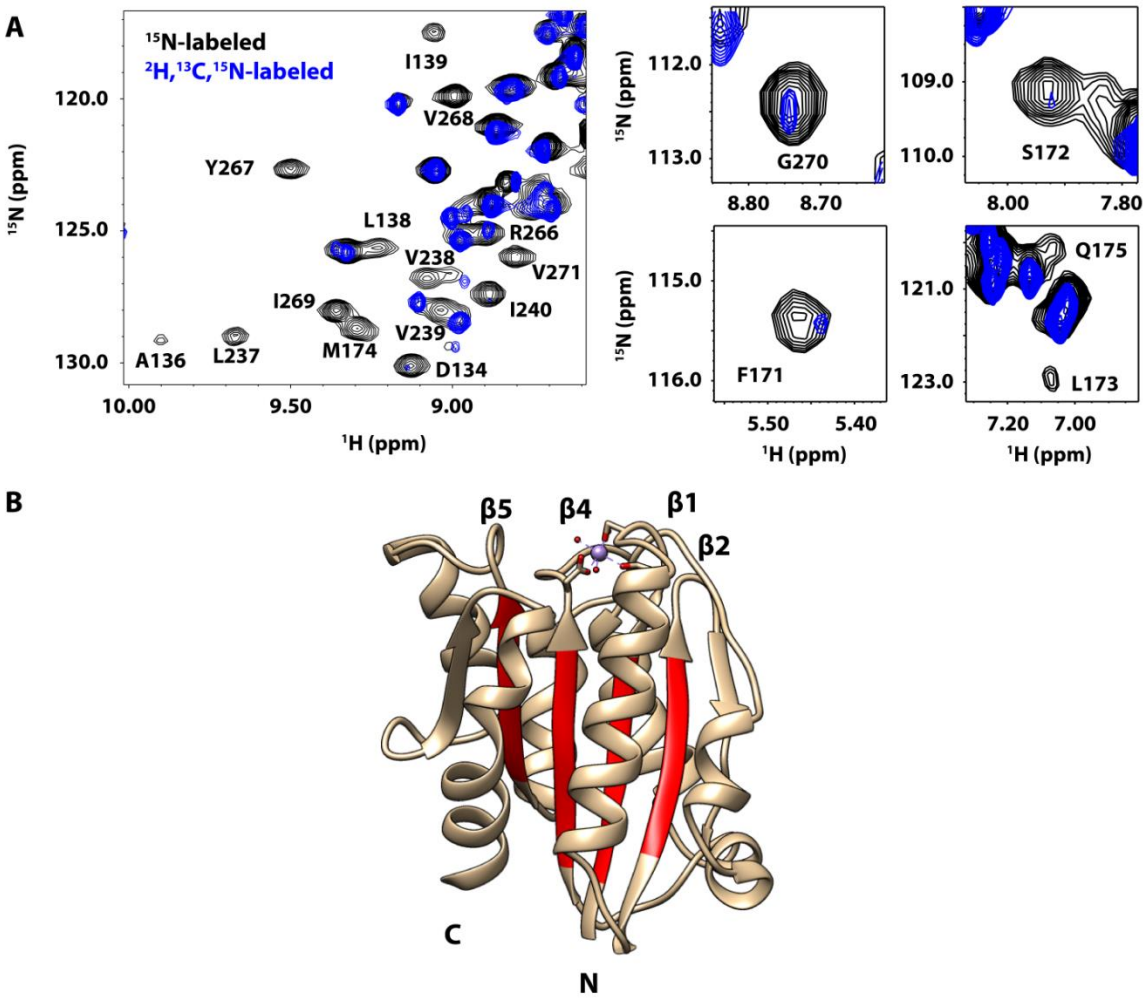

Figure 3.4 Central β Strands are Protected from Exchange with Solvent.
(A), ^{15}N HSQC overlays of residues with lower signal intensity. (B), protected residues are mapped (colored red) on the ribbon structure of α_M I domain.

2, pH stability and Mg^{2+} titrations

Like other membrane proteins, integrins are present on cell surface and regulated by the dynamic environment in which the cells reside. It has been found that lower extracellular pH, which occurs naturally at sites of inflammation, promotes integrin activation by facilitating open conformations and up-regulates many physiological

processes mediated through integrins, such as cell adhesion and migration (21,22). Present study focus on integrin α_M I-domain and assess its pH stability with circular dichroism (CD) spectroscopy. α_M I-domain samples in buffers ranging from pH 4.0-7.0 and a control sample without proteins were analyzed with CD. The CD data revealed that the overall fold of α_M I-domain is relatively stable under acidic conditions, even as low as pH 4.0 (Figure 3.6). This naturally leads to questions of how pH affects the conformation of the entire integrin molecules when α I-domain structure is not significantly altered. As shown through molecular dynamics simulations, acidic pH favors headpiece opening in some integrins (21). Therefore, it would be insightful to investigate how α_M I-domain responds to lower pH levels.

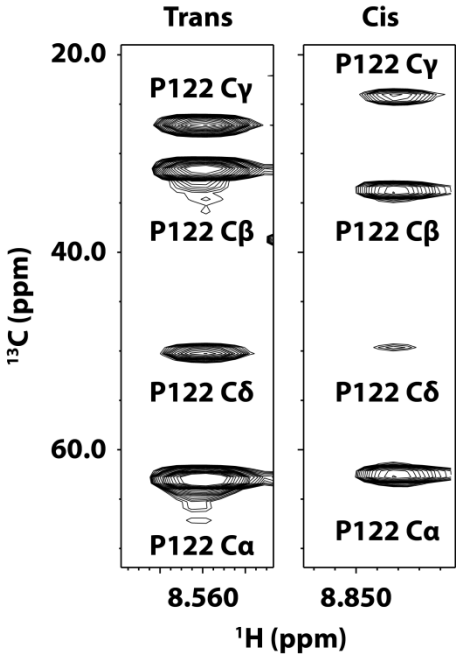

Figure 3.5 CCCONH spectra of Two Peaks Representing E123.
The side chain carbon resonances are from the previous residue P122. Left and right spectra are for trans- and cis-isomers respectively.

Divalent metal ions, such as Mg^{2+}, Mn^{2+} and Ca^{2+}, are critical for integrins as they are capable of regulating the ligand binding affinities (5). It was found that Mn^{2+} promotes, while Ca^{2+} inhibits integrin activation in many instances (23-25). Under physiological conditions, α I-domain MIDAS binds Mg^{2+} (5). Three MIDAS loops donate residues to directly coordinate Mg^{2+}. In the ligand-bound form, MIDAS rearranges so that one coordinating residues leaves and is replaced by an acidic residue from the ligand, thereby making Mg^{2+} necessary for ligand bindings (4). This is corroborated by X-ray crystal structures of high-affinity/open and low-affinity/closed states of integrin α_M I-domains (1,17). In light of the importance of metal bindings, the present work also assesses how pH affects Mg^{2+} bindings using solution NMR techniques. Figure 3.7 displays HSQC overlays of ^{15}N α_M I-domain in the presence or absence of Mg^{2+} at pH 5.0 and 7.0. At pH 7.0, Mg^{2+} addition results in a significant number of peak migrations, indicative of Mg^{2+} bindings. While at pH 5.0, there is no peak migration, which means Mg^{2+} bindings are not present under acidic pH conditions. Lower pH protonates acidic amino acids, therefore discourages metal coordination.

To quantify Kd of Mg^{2+} bindings at pH 7.0, Mg^{2+} was added in series to α_M I-domain sample to reach each specific concentration (0, 0.25, 0.5, 1.0, 2.0, 5.0, 10 and 50 mM). ^{15}N HSQC spectrum was collected for each titration point and displayed together. Instantly, it was noticed that Mg^{2+} bindings fall into a slow timescale exchange regime as two resolvable peaks were observed. With Mg^{2+} concertation increasing, one resonance gradually decreases in intensity while the other gains in intensity. Using the line shape fitting approach developed by Kovrigin (26) , two residues were selected and fitted to

extract the Kd value. Kd is fitted to be ~1.3 ± 0.3 mM, consistent with previous results from isothermal titration calorimetry (27). However, the NMR study also revealed that the kinetics of interaction between the protein and metal is slow. Specifically, the dissociation rate constant is only 0.0015 s^{-1}. Figure 3.8 shows line shape analysis of G141 and F184 in Mg^{2+} Titration.

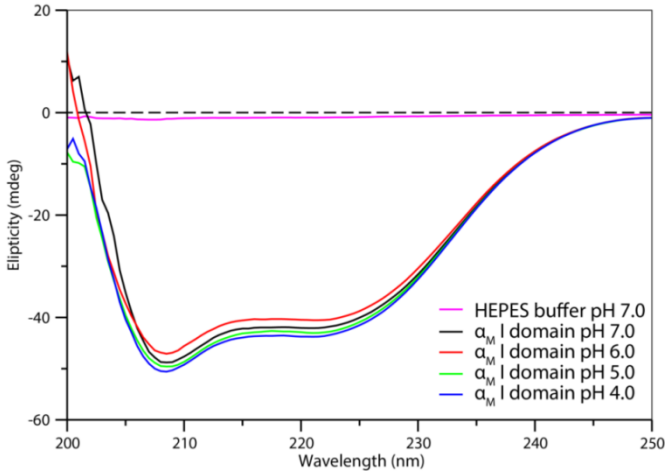

Figure 3.6 CD Spectra of Integrin α_M I-domain at Different pH Levels.
20 uM α_M I-domain in 20 mM HEPES and 100 mM NaCl under pH ranging from 4.0 to 7.0. HEPES buffer pH 7.0 serves as the negative control.

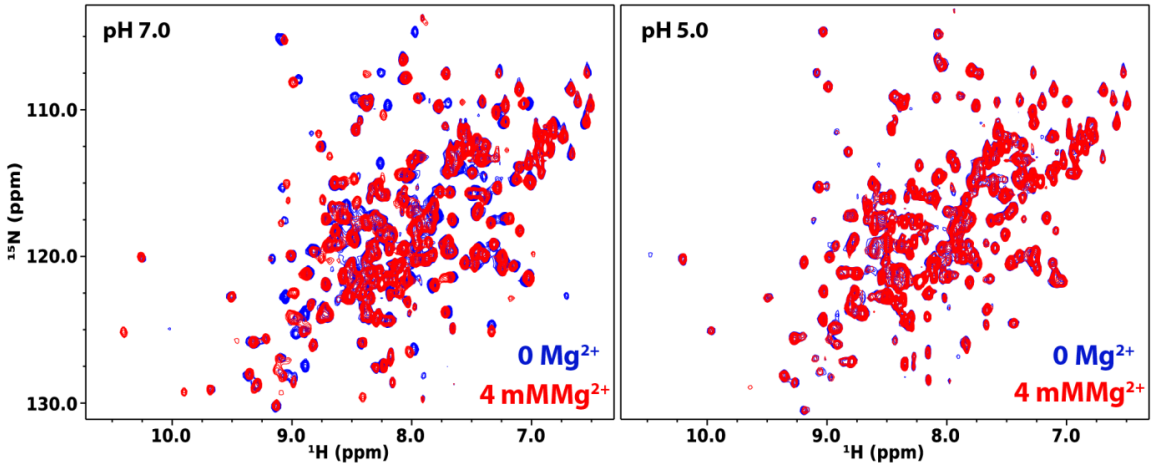

Figure 3.7 Mg^{2+} Bindings under Different pH Conditions.
The left (pH 7.0) and right (pH 5.0) are ^{1}H-^{15}N HSQC spectra are 150 µM ^{15}N α_M I

domain (Q119-E333) with or without 4 mM Mg^{2+}.

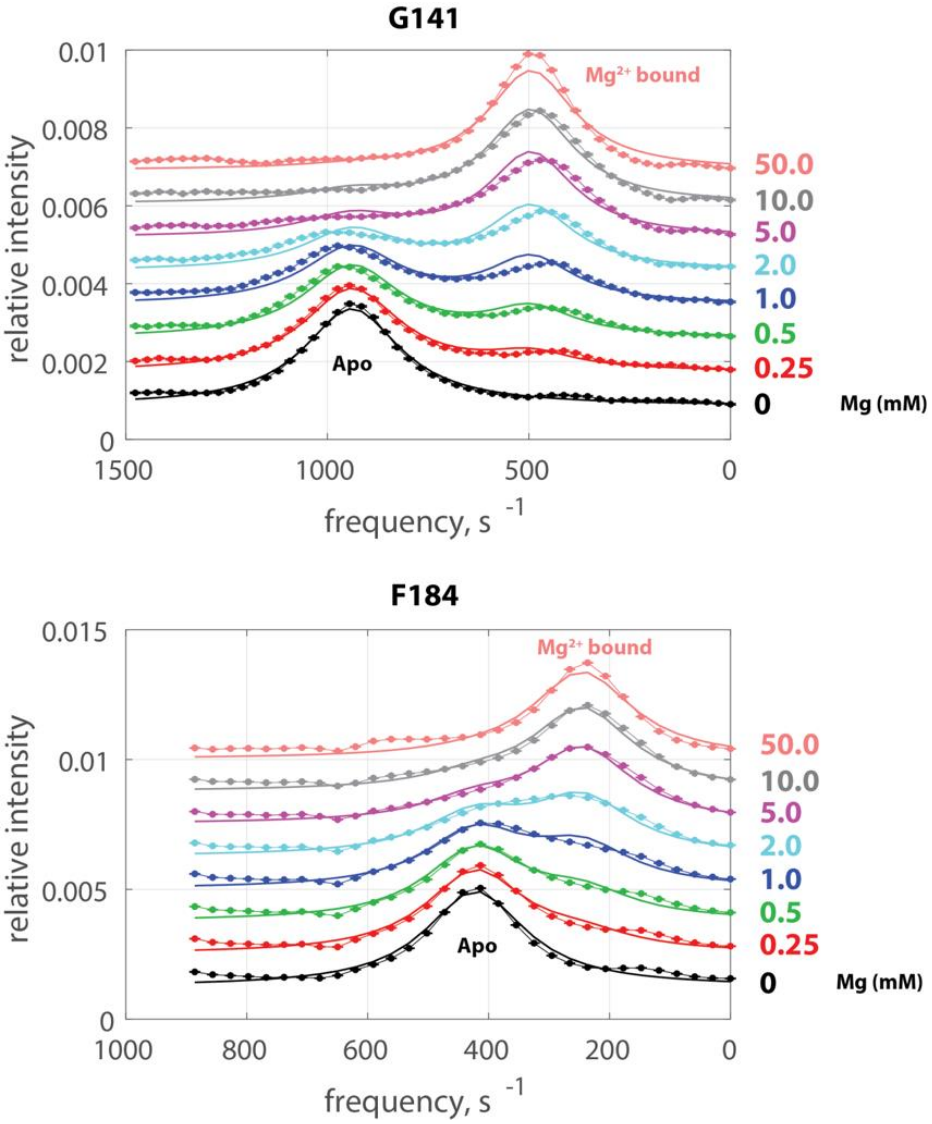

Figure 3.8 Line Shape Fitting Analysis of α_M I-domain Titration with Mg^{2+}.
Mg^{2+} concentrations are colored coded, ranging from 0 to 50 mM. 1D traces of G141 and F184 are displayed with error bars representing noise r.m.s. deviation for each spectrum. Data were fitted according to a two state model and the best fits are the curves with no error bars. K_d is fitted to be 1.3 ± 0.3 mM.

3, Homodimeric interactions

As shown in the X-ray structure of integrin $\alpha_x\beta_2$, the interface of the heterodimer involves α I-domain and β propeller from α subunit and β I-domain from β subunit (28). To be more specific, N and C termini of α I-domain are in close proximity to the MIDAS of β I-domain. The proposed activation mechanism (Figure 1.4 in Chapter 1) also denotes that an acidic amino acid on the C terminus of α I-domain interacts with MIDAS of β I-domain upon activation. Because the structural similarity between α I-domains and β I-domains, this raise the question of whether α I-domains have the potential of self-association. In this work, we examined homodimeric interactions between α_M I-domains using paramagnetic relaxation effects. Paramagnetic relaxation enhancement (PRE) in NMR is widely used to provide intermolecular distance-related information, which will be explored in details in the next chapter. We utilized the only cysteine in the protein, C128 on N terminus, to attach the paramagnetic nitroxide radical MTSL (*S*-(1-oxyl-2,2,5,5-tetramethyl-2,5-dihydro-1H-pyrrol-3-yl)methyl methanesulfonothioate) in full length (Q119-E333) version of integrin α_M I-domain. The magnetic field produced by unpaired electron of the radical will perturb nearby atoms and consequently increase these atoms' transverse relaxation rates (R_2) in a distance dependent fashion and therefore, lower signal intensity. Ascorbic acid can be added to reduce paramagnetic radicals and signal intensity is restored. The signal loss is inversely correlated with the distance between the radical and the atom (29).

We first observed homodimeric interactions on MTSL-labeled integrin α_M I-domain as displayed in Figure 3.9. Not surprisingly, N-terminal (C128) MTSL perturbs a great number of residues in the nearby N/C termini region, such as G321 (C terminus),

D134 (N terminus) and I265 (α5-β5 loop). Unexpectedly, residues Q204, G207 and R208 on α3- α4 loop in MIDAS are also perturbed by the N-terminal MTSL (Figure 3.9A). PRE analysis using a mixture of natural abundance MTSL-α_M I and ^{15}N α_M I-domain confirmed that PRE perturbations on MIDAS residues are indeed intermolecular rather than intramolecular (Figure 3.9B).

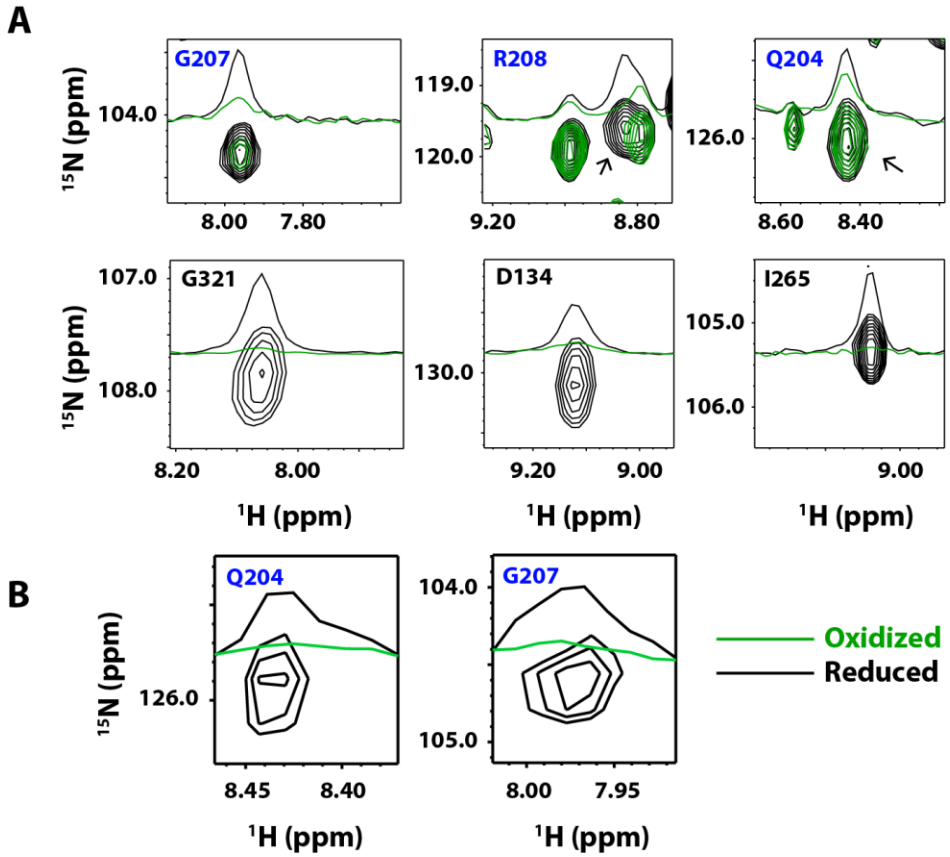

Figure 3.9 Homodimeric Interactions of Integrin α_M I-domain.
(A), ^{15}N HSQC spectra of MTSL-tagged ^{15}N α_M I-domain. Residues are perturbed by MTSL-labeled N terminus (C128). The upper panels are G207, R208 & Q204 in MIDAS, while the lower panels are G321, D134 and I265 in N/C termini region. (B), ^{15}N HSQC spectra of ^{15}N α_M I-domain mixed with natural abundance MTSL-tagged α_M I-domain (C128).

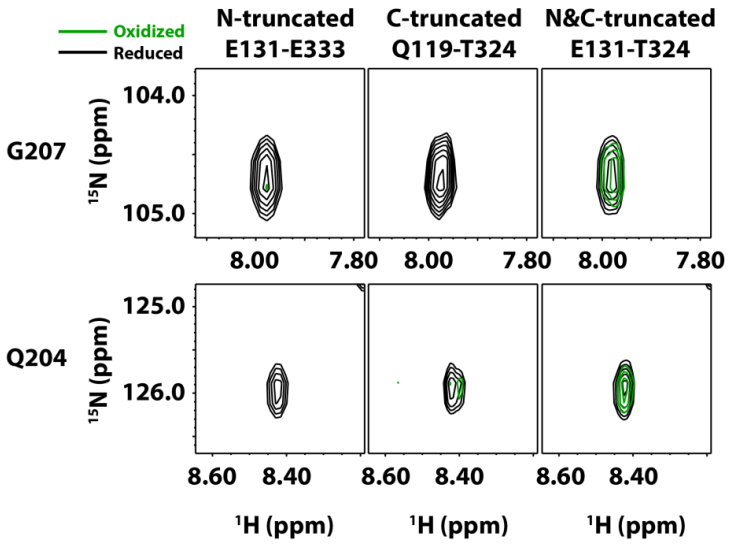

Figure 3.10 N or C Terminus Alone Mediates Intramolecular Homodimeric Interactions of Integrin α_M I domain.
N (C321-MTSL), C (C128-MTSL) and N/C (C321-MTSL)-truncated versions are generated. C128 and C321 are on N terminus and C terminus respectively. N/C MTSL perturbations to G207 and Q204 are significant in N-truncated or C-truncated versions. Only when N and C termini are simultaneously removed are the intramolecular interactions abolished. 200 µM of MTSL-tagged ^{15}N-integrin α_M I domain.

Now the intermolecular interaction of α_M I-domains is established. To identify which terminus is responsible for facilitating homodimeric interactions, the following constructs were designed, N-truncated version (E131-E333, C321-MTSL), C-truncated version (Q119-T324, C128-MTSL) and N&C-truncated (E131-T324, C321-MTSL). PRE data were acquired in the same way as described in Figure 3.10. For the three constructs above, significant perturbation is observed on residues in the N/C termini region (data not shown), which is not surprising as MTSL is tagged on either N or C terminus. However, as shown in Figure 3.10, several residues in the MIDAS, such as Q204 and G207, have enormous signal loss in either N-truncated or C-truncated versions whereas minor signal

decrease is seen on N&C-truncated version. Removal of N-terminus or C-terminus alone cannot abolish this intramolecular interaction to the same level as simultaneous removal of N and C termini. Therefore, N or C terminus alone is capable of interacting with MIDAS of another α_M I-domain. To our best knowledge, this is the first report of intermolecular interactions of integrin α I-domain.

3.5 Discussion

NMR has been instrumental in determining structures of integrin transmembrane and cytoplasmic domains (30-36). There have also been reports on use of NMR in studying integrin α_1 I (37-39), α_2 I (40) and α_L I (41-44) -domains. To our best knowledge, this is the first NMR study of α_M I-domain. Interestingly, although α_M I-domain and α_L I-domain share considerable sequence and structural homology, ^{15}N HSQC spectrum of α_M I-domain was of significantly worse quality compared to that of α_L I-domain. In particular, signals in ^{15}N HSQC of α_L I-domain showed far greater chemical shift dispersion and signal intensities are more even (44). The uneven signal levels in α_M I-domain spectra could be the result of oligomerization or dynamics. T_2 relaxation experiments provided estimations of rotational correlation time (τ_c), which does not imply presence of dimer, or any other oligomer. TROSY (transverse relaxation optimized spectroscopy)-HSQC did not show any significant improvement in resolution and sensitivity, which also suggests lack of oligomerization. Therefore, the uneven signal intensity distribution is likely a result of the intrinsic dynamics of the protein. In addition to that, most of the unassigned residues are in the α3-α4 loop and α4 helix. As almost all observed peaks are assigned, unassigned residues are due to weak signals. This hints the

occurrence of conformational dynamics, which leads to signal broadening. Poor NMR data quality because of dynamics might suggest why there is no NMR study on α_M I-domain, despite being well studied previously by crystallography (1,17,45). Chapter 5 will explore the conformational dynamics using NMR relaxation dispersion experiments.

CSI analysis performed in this study indicates that the construct used here adopts the same secondary structural arrangement in solution as the crystal structure, indicating they have the same conformation (17). When deuterated α_M I-domain was first prepared, many peaks in its ^{1}H-^{15}N HSQC spectrum are missing or have significantly lower signal intensities compared to undeutrated samples. The signal loss is due to restricted hydrogen/deuterium exchange because of the extensive hydrogen bond network. These protected residues are located in the central β strands sandwiched by α helices, which is consistent with the crystal structure.

Proline isomerization was reported to act as molecular switches that control protein activation (20). This type of activation is very unique as it does not require covalent modification and is able to induce significant conformational changes because the cis and trans isomers have drastically different dihedral angles. α_M I-domain has shown well resolved signals in NMR spectra, supporting the existence of proline isomerization with "trans" as the major state. Pro 122 on the N-terminal linker is close to the interface of α I-domain, β-propeller and β I-domain. Studies have shown that mutations in the interface and antagonists for the interface both promote integrin activation (46,47). Therefore it begs the question of whether P122 isomerization could

regulate integrin activation by modulating conformations in the interface. How P122 isomerization is biologically relevant should be investigated further.

Another potential activation factor is pH. Molecular dynamics (MD) simulations indicated that lower pH levels facilitate integrin activation by promoting headpiece opening (21). CD spectroscopy revealed that integrin α_M I domain is very resistant to pH change and maintains its fold even at pH 4.0. In contrast, α_M I-domain variants designed to adopt the active state through truncation at I316 or bearing the I316G mutation (48), is far less resistant to pH (data not shown). It is not known if the dramatic difference in pH tolerance between inactive and active states is functional or relevant under physiological conditions.

Universal to all integrin molecules, Mg^{2+} bindings are important to ligand interactions. Mg^{2+} titrations under pH 5.0 and pH 7.0 suggest that lower pH levels abolish Mg^{2+} bindings. At pH 7.0, two populations for apo and Mg^{2+} bound states respectively are well resolved in NMR spectra, suggesting chemical exchange on slow timescales. Quantitative analysis using line shape fitting approach reveals the Kd is ~ 1.3 ± 0.3 mM range at pH 7.0 (26). This is in agreement with Kds determined from isothermal titration calorimetry (ITC) (27). Weak metal affinity indicates that α_M I-domain is basically not saturated under physiological conditions (1 mM Mg^{2+}). As Mac-1 is the most promiscuous of all integrins, various ligands might interact with α_M I-domain through different mechanisms.

Surprisingly, homodimeric interactions between integrin α_M I-domains were discovered in current studies. Specifically, MIDAS of one α_M I-domain weakly interacts with N/C termini of another α_M I-domain. In light of the similarity between α I- and β I-domains, such homodimeric interactions of αI domains are suspected to be reminiscent of the heterodimeric interaction of α I- and β I-domains. The intermolecular interaction resembles the interface in intact integrin proteins where α chain and β chain lie together. Crystal structure of $\alpha_x\beta_2$ confirms the structural arrangements (28). Not surprisingly, intramolecular PRE effects are more significant than intermolecular PRE. However, intermolecular PRE perturbations are still present, especially for Q204, G207 and R208 on the α3-α4 loop. Since N and C terminus are positioned closely together, it was intuitive to investigate which terminus is involved in the intermolecular interactions. As revealed in Figure 3.10, intermolecular PRE perturbations on α3-α4 loops in MIDAS are still observed after only one of the termini is removed, while they are obviously abated when N and C termini are simultaneously truncated. This clearly elucidates that either terminus is able to mediate the homodimeric interactions. However, a lot of questions remain unanswered. For example, what is the biological relevance of the interaction and how is it regulated (pH or Mg^{2+})? More work needs to be performed to answer the questions.

CHAPTER 4

A NOVEL MECHANISM GOVERNS INTERACTIONS OF α_M I-DOMAIN WITH CATIONIC LIGANDS

4.1 Abstract

$\alpha_M\beta_2$ (Mac-1, CR3, CD11b/CD18) is an α I-domain containing member of the integrin family. It is highly expressed in macrophages and plays important roles in many immunological events. Unlike other integrins, Mac-1 can bind a broad spectrum of ligands. Studies have shown that α_M I-domain, which is responsible for more than 90 % of ligand binding activity of Mac-1, prefers ligands enriched in basic amino acids, not acidic amino acids. This contradicts the canonical ligand binding mechanism of α I-domains, which requires an acidic amino acid in the ligand to facilitate metal mediated binding to the domain. Lack of acidic amino acids in these ligands hints the existence of a novel ligand binding mechanism for α_M I-domain. In the present study, we analyzed interactions of α_M I-domain with two of its cationic ligands using solution NMR and microscale thermophoresis (MST). Our data indicate that α_M I-domain bind these ligands in a metal-independent manner and the binding site is located near α_M I-domain's metal ion dependent adhesion site (MIDAS). We believe this is made possible by the weak metal affinity of α_M I-domain's MIDAS, which leaves it metal-free under physiological conditions, allowing acidic amino acids in MIDAS to interact with positively charged ligands. Consistent with this is the observation that high concentrations of divalent cations have inhibitory effect on binding of the cationic ligands and one cationic ligand, the chemokine PF4, actually prevents binding of divalent cations to MIDAS. We also

determined that the binding of PF4 does not change the conformation of α_M I-domain. This implies activation of Mac-1 by these ligands should be a consequence of ligand induced integrin clustering.

4.2 Introduction

α_M β_2 (Mac-1, CR3, CD11b/CD18) is a member of the integrin receptor family highly expressed in macrophages and neutrophils. Its function is vital to a number of important immunological activities but is especially crucial to opsonization and trafficking of macrophages and neutrophils. Integrins are heterodimeric protein complexes made up of an α and a β subunit. They act as adhesion receptors that connect intracellular structures with the extracellular environment. Because of their importance, activities of integrins are closely regulated. In particular, integrins in the inactive form have lower affinity for their ligands than integrins in the active form. Conversion of inactive integrins into the active form can be triggered by intracellular as well as extracellular signals. These pathways are referred to as inside-out or outside-in pathways depending on the origin of the signal. The mechanism of inside-out pathways is relatively well understood. Specifically, activation of certain intracellular kinases is believed to lead to phosphorylation of cytoplasmic domains of the α and β subunits as well as recruitment of cytoskeletal proteins such as talin to the integrin, causing the cytoplasmic domains to separate and the ectodomains to change from a folded to extended conformation. The consequence of these changes is an increase in the integrin's affinity for its ligands (1). The exact mechanism of outside-in signaling is less well understood, but it is accepted

that binding of some ligands induces clustering of integrins, leading to activation of intracellular kinases such as Src (2).

Ligand specificity is an important determinant of integrin activity. Mac-1 belongs to a class of integrins that bind ligands mostly through an extra domain on the tip of their α subunits. This domain is a metal-binding Rossmann fold domain and is commonly referred to as the α I-domain. The canonical ligand binding mechanism of α I-domains relies on cooperative coordination of a divalent cation by residues in α I-domain and acidic amino acids in the ligand (1). Because the metal ion is important for ligand binding and adhesion, the metal binding site in I-domains is commonly known as the metal ion dependent adhesion site (MIDAS). This has been observed in structures of α I-ligand complexes (3-6). In the binding interface, ligand donates an Asp or Glu to coordinate the metal ion in MIDAS, as shown in Figure 4.1. So far, this canonical ligand-binding mechanism can explain ligand specificity of most α I-domains. However, there are notable exceptions. For instance, α_2 I-domain is known to bind a cyclic peptide composed entirely of positively charged amino acids (7). More recently, the ligand specificity of Mac-1 ($\alpha_M\beta_2$) was also shown to be outside of the scope specified by the canonical mechanism.

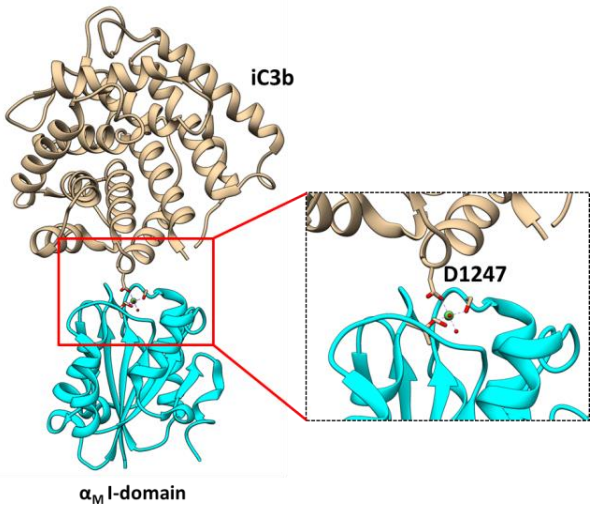

Figure 4.1 Crystal Structure of α_M I-domain with C3d, Complement Component C3d Fragment.
D1247 in C3d (brown) directly coordinates Ni^{2+} ion in the MIDAS of α_M I-domain (cyan). The interaction interface is enlarged for clear visualization. The ribbon structure is produced from pdb: 4m76.

Mac-1 is one of the most promiscuous integrins known. Mac-1 binds ligands as distinct as fibrinogen, vitronectin, ICAM-1, iC3b, E-selectin and heparin (8). A systematic peptide library screening study showed α_M I-domain, which is responsible for ~ 90 % of Mac-1's ligand binding activity, preferentially binds to peptides containing basic and hydrophobic amino acids, not acidic amino acids. This indicates α_M may utilize a yet-uncharacterized ligand binding mechanism. Using the consensus Mac-1 binding motif identified in the study, several new Mac-1-binding ligands have been discovered, including LL-37 (9), dynorphin-A (10), pleiotrophin (PTN) (11) and platelet factor 4 (PF4/CXCL4) (12), all of which are highly cationic peptides.

We have been interested in characterizing this novel ligand-binding mechanism of α_M I-domain. Our hypothesis is based on the fact that cationic proteins such as PTN bind

their receptors mainly through electrostatic interactions with acidic amino acid clusters on receptors. Analysis of the electrostatic potential on the surface of α_M I-domain revealed that the most negatively charged region on the domain is in fact around the metal-free MIDAS, which possesses several acidic amino acids involved in metal coordination. Although binding of divalent cation to MIDAS does neutralize the charges, Ca^{2+} and Mg^{2+} affinity of wild type α_M I-domain has Kd in the mM range (13), significantly lower than other α I-domains. This means a large fraction of α_M I-domain may remain in the metal-free state under physiological conditions. Based on these observations, we believe that MIDAS is the binding site of these cationic ligands and the interaction occurs in a metal-independent manner. To confirm this, we have studied interactions of α_M I-domain with both PTN and PF4 using solution NMR spectroscopy and microscale thermophoresis (MST). Our data show wild type α_M I-domain binds PTN and PF4 in a metal-independent fashion, and both ligands bind close to the MIDAS. In addition, MST results indicate high Mg^{2+} concentrations significantly lower α_M I-domain's affinity for both PTN and PF4, indicating existence of competitive binding between these ligands and metal ions. This was confirmed by NMR data that showed that presence of PF4 inhibited Mg^{2+} binding. Finally, the binding of these cationic ligands does not appear to change the conformation of wild type α_M I-domain significantly. These data are a first step in understanding the unique mechanism these ligands use to modulate Mac-1 activity.

4.3 Materials and Methods

1, Expression and purification of proteins

The open reading frame (ORF) of the wild type α_M I domain (E131-T324) was cloned into the pHUE vector as a fusion protein with His-tagged ubiquitin at its 5' end (14). BL21 (DE3) cells transformed with expression vectors were grown in M9 medium at 37 °C to an OD_{600} of ~ 0.8, at which point the culture was induced with 0.5 mM IPTG and harvested after overnight incubation at room temperature (23°C). To prepare isotopically labeled proteins, $^{15}NH_4Cl$ and/or ^{13}C glucose was added into M9 media. Post-induction cell cultures were then harvested, resuspended in lysis buffer (20 mM sodium phosphate, 0.5 M Nacl 10 mM imidazole, 5% glycerol, 0.01% NaN_3), treated with 1mg/mL lysozyme for 20 min and sonicated. After centrifugation, supernatant was collected and subjected to Ni-affinity chromatography with 5-mL HisTrap column (GE Life Sciences). To elute the protein, an imidazole gradient of 35 to 500 mM was applied at a flow-rate of 3 mL/min. Eluent fractions containing the fusion proteins (His-tagged-ubiquitin-integrin α_M I domain) were then buffer exchanged into 25 mM Tris and 100 mM NaCl, pH 8.0 and treated with 1/20 molar equivalent of the His-tagged ubiquitinase USP2 catalytic core domain overnight at room temperature to cleave ubiquitin from the fusion protein (14). To separate cleaved α_M I domain from His-tagged ubiquitin, His-tagged USP2 and undigested fusion proteins, digestion mixture was passed down a second Ni-affinity column. Flow-through was collected and applied to a Superdex 75 size exclusion chromatography column (GE Life Sciences) for further purification. Purity of the protein in each fraction was verified using SDS-PAGE analysis.

PTN (T47C & S106C) expression and purification schemes were performed according to previously reported protocols (15). Briefly, pET-15b vector harboring human PTN ORF was transformed into Origami B (DE3) cells (Novagen, Madison, WI, USA). Cells were grown in M9 medium at 37 °C to an OD_{600} of 0.5 when 0.25 mM IPTG was added before overnight culture at room temperature. Cells were harvested, re-suspended, treated with lysozyme and sonicated in the same way as mentioned above for α_M I domain. After centrifugation, supernatant was applied onto 5mL HiTrap SP HP column (GE Healthcare Life Sciences) and eluted with 1 M NaCl gradient.

Cloning and culture of PF4 (S26C) is the same as PTN. Purification was accomplished using a 5mL HisTrap Heparin HP affinity column (GE Life Sciences) and eluted with a 0.1 to 3 M NaCl gradient. PF4 fractions were buffer exchanged and concentrated in 20 mM acetate, 150 mM NaCl buffer (pH 5.0).

2, NMR data acquisition and backbone assignment

All data were collected on Bruker AVANCE 600 MHz and 850 MHz spectrometers equipped with cryo-probes. All NMR samples contain 0.15-1 mM α_M I domain in 20 mM HEPES and 100 mM NaCl (pH 7.0). For backbone assignment, HNCACB, HNCOCACAB, HNCO and HNCACO spectra were collected on $^{2}H/^{13}C/^{15}N$ integrin samples. In addition, $^{13}C/^{15}N$ integrin was used to collect HNCA, HNCOCA, HNCO and HNCACO spectra. To assist backbone assignment, CCCONH and ^{15}N-edited NOESY spectra were also acquired. All NMR data were processed with NMRPipe (16) and analyzed with NMRView (17).

To probe the PF4-induced chemical shift change, ^{1}H-^{15}N HSQC spectra were acquired for a sample containing 150 uM ^{15}N α_M I domain only and another sample containing 500 uM PF4 and 150 uM ^{15}N α_M I domain at 0 and 10 mM Mg^{2+}. Chemical shift changes on ^{1}H and ^{15}N dimensions of the two spectra were quantified using one single chemical shift value δ ($\delta = [\Delta\delta_H^2 + (0.2\ \Delta\delta_N)^2]^{1/2}$) (18).

To examine the competition of Mg^{2+} and PF4, ^{1}H-^{15}N HSQC spectra of 150 uM ^{15}N α_M I domain were collected at 0 and 10 mM Mg^{2+}. The same spectra were acquired with 150 uM ^{15}N α_M I domain and 500 uM of PF4 at 0, 10 and 50 mM Mg^{2+}.

3, Paramagnetic relaxation enhancement (PRE)

To paramagnetically label PTN, purified PTN was immediately buffer exchanged to PBS buffer and mixed with 10 molar equivalents of MTSL (1-Oxyl-2,2,5,5-tetramethylpyrroline-3-methyl) methanethiosulfonate (Santa Cruz Biotechnology) for overnight incubation. Then the mixture is buffer exchanged to 10 mM MES, 150 mM NaCl buffer (pH 6.0) to remove unreacted MTSL. MTSL-labeled PF4 was created in a similar fashion. Specifically, MTSL was added directly to the combined PF4 fractions for overnight labeling before being removed by buffer exchanging the mixture into 20 mM acetate, 150 mM NaCl buffer (pH 5.0). The MTSL labeling efficiency was verified by comparing 1D ^{1}H NMR spectra before and after addition of ascorbic acid.

To measure PTN-induced PRE perturbations on α_M I domain, two samples (~ 300 uL, pH 7.0) samples containing 150 uM ^{15}N α_M I domain and 900 uM MTSL-tagged S106C or T47C PTN were prepared. 2.8 uL 0.5M ascorbic acid was added to one sample to reduce the radical to its diamagnetic form (19). pH of both samples was checked to

ensure absence of artifacts due to pH difference. PRE effects from MTSL-tagged PTNs were analyzed by comparing ^{1}H-^{15}N HSQC spectrum of diamagnetic sample with that of paramagnetic sample. The experiments were repeated with no Mg^{2+} or with 10 mM Mg^{2+}. To investigate the effect of Mg^{2+}on ligand affinity, 150 uM of ^{15}N α_M I domain and 150 uM MTSL-tagged S106C PTN were mixed without Mg^{2+} or with 50 mM Mg^{2+}. PF4 experiments were performed similarly with the exception that only 500 uM MTSL-tagged PF4 S26C added to 150 uM ^{15}N α_M I domain at pH 6.6. pH of all samples were checked to rule out artifacts from pH variations.

4, Microscale thermophoresis (MST)

The binding affinity of PTN or PF4 to wild type α_M I-domain was determined by MST in the presence and absence of Mg^{2+}. The MST experiment was performed using Monolith NT.115 (Nanotemper). The protein was randomly labeled with DyLight 488 NHS Ester dyes (Thermo Scientific) through amine groups on the protein following the instructions from manufacturer. For optimal labeling efficiency, the protein was buffer exchanged to 0.05M sodium borate buffer at pH 8.5 and concentrated to 5mg/mL. The DyLight 488 NHS-Ester was dissolved in DMF. Protein was then mixed with 5 molar equivalents of DyLight 488 NHS-Ester and incubated at room temperature for 1 hour. The unreacted dyes were removed from labeled protein by buffer exchanging the protein to 20mM HEPES and 100mM NaCl pH 7.0 buffer. The degree of labeling was calculated based on the protocol from manufacturer and there are 2.7 moles dye per mole protein. For PTN titrations, the samples were prepared in the buffer of 20mM HEPES, 100mM NaCl, 0.05% Tween 20, pH 7.0 with varied concentration of Mg^{2+}(no Mg^{2+}, 1mM Mg^{2+}

or 50mM Mg^{2+}) For PF4 titration, the samples were prepared in same buffer with pH 6.0 to prevent PF4 precipitations. α_M I-domain mutants were prepared in the same way as the WT α_M I-domain. Each MST sample contains ~ 10 µL of 50 nM DyLight 488-labeled α_M I-domain in the presence of different concentrations of PTN or PF4 and placed in Standard treated capillaries (Nanotemper). Data was collected from three measurements and calculated for the standard deviation as error. The binding constant Kd was calculated by fitting the plot of normalized changes in fluorescence due to thermophoresis (ΔF_{norm}) vs concentrations of the ligand using the equation $f(L) = Unbound + \frac{(Bound-Unbound)\times(L+P+Kd-\sqrt{(l+P+Kd)^2-4\times L\times P})}{2\times P}$ where Bound is the MST response value of α_M I-domain fully saturated with the ligand, Unbound is the response value of α_M I-domain in the absence of the ligand, L is the ligand concentration, P is the concentration of α_M I-domain.

4.4 Results

1, α_M I-domain's interaction with PTN & PF4 is metal-independent

Divalent cations such as Ca^{2+} or Mg^{2+} are usually essential to ligand binding activities of integrins. However, absence of acidic amino acids in many α_M ligands begs the question of whether α_M I-domain's interactions with these ligands are metal mediated. To test this hypothesis, we measured the affinity of α_M I-domain for PTN and PF4 using microscale thermophoresis (MST). Both PTN and PF4 induced significant changes in thermophoresis of fluorescently labeled α_M I-domain (Figure 4.2). Both proteins also caused α_M I-domain to migrate towards the heat source, indicating the complex they form with α_M I-domain have similar physical properties. However, the affinity of α_M I-domain

for PTN is slightly higher than that for PF4 (Kd of ~1 and ~6 µM, respectively) More importantly, both proteins bind α_M I-domain even in the absence of Mg^{2+} and addition of physiological concentration of Mg^{2+} (1 mM) did not change the affinity (Figure 4.2). This implies metal is not essential to interactions of these ligands with α_M I-domain.

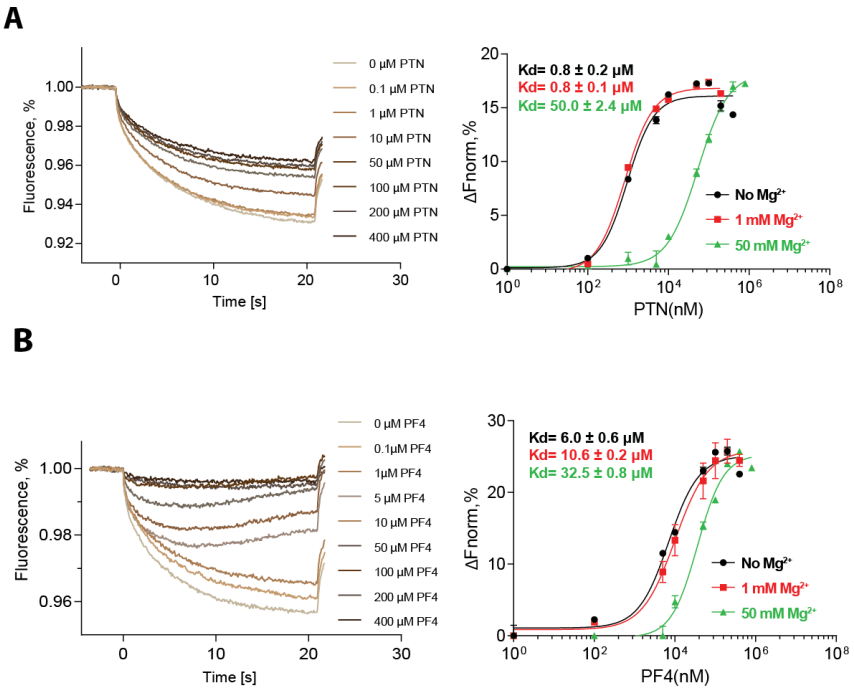

Figure 4.2 MST Analysis of α_M I-domain's Interactions with PTN and PF4.
(A), Thermophoresis of Dylight 488 labeled α_M I-domain was measured at different concentrations of PTN. Left panel is the fluorescent time traces during thermophoresis. Right panel is the binding curves obtained from fitting the thermophoresis signals at different Mg^{2+} concentrations. (B), Thermophoresis of Dylight 488 labeled α_M I-domain was measured at different concentrations of PF4. Left panel is the fluorescent time traces during thermophoresis. Right panel is the binding curves obtained from fitting the thermophoresis signals at different Mg^{2+} concentrations.

Because Mg^{2+} affinity of α_M I-domain is relatively low (Kd ~ 1 mM) (13), MIDAS in α_M I-domain is likely not fully saturated at physiological Mg^{2+} concentrations. In order to investigate the effect of metal-saturation on the binding of PTN and PF4 α_M I-domain, we also measured α_M I-domain's affinity for these ligands in the presence of 50

mM Mg^{2+}. Surprisingly, data showed higher Mg^{2+} concentration significantly lowered the affinity of α_M I-domain for these ligands. In particular, α_M I-domain's Kd for PTN increased from 1 μM to 50 μM while its Kd for PF4 increased from 6 μM to 35 μM (Figure 4.2). To ensure the effect is not entirely due to change in ionic strength, we also carried out control experiments in which NaCl concentration in the buffer is increased by 100 mM. The results showed ionic strength alone only accounts for ~ 50 % of the decrease in affinity in the case of PTN (Figure 4S1). Similar analysis on PF4's interaction with α_M I-domain showed the increase in ionic strength can account for all the decrease in α_M I-domain's affinity for PF4. These results imply the interactions between the cationic ligands and α_M I-domain relies mainly on electrostatic interactions and divalent metal ions such as Mg^{2+} have high specificity as competitive inhibitors of PTN, contrary to other ligands that bind α_M I-domain through the metal.

2, NMR analysis of PTN-α_M I-domain interactions

To determine the binding site of the cationic ligands on α_M I-domain, we initially attempted chemical shift perturbation mapping, which uses environmental sensitivity of amide hydrogen and nitrogen chemical shifts to locate residues at the ligand binding interface. However, no significant changes in the ^{15}N-HSQC spectrum of α_M I-domain were induced even with high concentrations of PTN (~ six molar equivalents). This is typical of interactions that are transient and dynamic in nature. To increase the sensitivity at which ligand binding can be detected, we created paramagnetically tagged PTN variants by mutating S106 or T47 to cysteine, which can be conjugated to the cysteine reactive paramagnetic compound MTSL (*S*-(1-oxyl-2,2,5,5-tetramethyl-2,5-dihydro-1H-

pyrrol-3-yl)methyl methanesulfonothioate). Similar to NOE, paramagnetic radicals have strong dipolar interactions with nuclei in a distance dependent manner. However, because electron has a larger gyromagnetic ratio than protons, paramagnetic effects have a longer range than NOE. The presence of such a paramagnetic center in the vicinity of other atoms increases the transverse relaxation rates (R_2) of these atoms, resulting in considerable signal intensity loss. This effect is commonly referred to as paramagnetic relaxation enhancement, or PRE. The long effective range of PRE makes it an ideal technique for probing transient and dynamic interactions between biomolecules.

3, NMR analysis of PTN-α_M I-domain interactions

To determine the binding site of the cationic ligands on α_M I-domain, we initially attempted chemical shift perturbation mapping, which uses environmental sensitivity of amide hydrogen and nitrogen chemical shifts to locate residues at the ligand binding interface. However, no significant changes in the ^{15}N-HSQC spectrum of α_M I-domain were induced even with high concentrations of PTN (~ six molar equivalents). This is typical of interactions that are transient and dynamic in nature. To increase the sensitivity at which ligand binding can be detected, we created paramagnetically tagged PTN variants by mutating S106 or T47 to cysteine, which can be conjugated to the cysteine reactive paramagnetic compound MTSL (*S*-(1-oxyl-2,2,5,5-tetramethyl-2,5-dihydro-1H-pyrrol-3-yl)methyl methanesulfonothioate). Similar to NOE, paramagnetic radicals have strong dipolar interactions with nuclei in a distance dependent manner. However, because electron has a larger gyromagnetic ratio than protons, paramagnetic effects have a longer range than NOE. The presence of such a paramagnetic center in the vicinity of other

atoms increases the transverse relaxation rates (R_2) of these atoms, resulting in considerable signal intensity loss. This effect is commonly referred to as paramagnetic relaxation enhancement, or PRE. The long effective range of PRE makes it an ideal technique for probing transient and dynamic interactions between biomolecules.

To carry out these PRE experiments, two samples of ^{15}N-labeled α_M I-domain mixed with six molar equivalents of MTSL-PTN were prepared. MTSL in one of the samples was kept in the paramagnetic state while MTSL in the other was reduced to the diamagnetic nitroxyl form using ascorbic acid. ^{15}N HSQC spectrum was acquired for each sample and peak intensity of each signal was then tabulated. Figure 4.3A shows sections from HSQC spectra of α_M I-domain in the presence of paramagnetic and diamagnetic S106C-tagged MTSL-PTN. S106 is located in the C-terminal domain (CTD) of PTN and PRE effects from this mutant are indicative of closeness of the CTD to α_M I-domain. This version of MTSL-PTN produced significant PRE effects on residues close to MIDAS. Specifically, G207 in the second MIDAS segment has the most significant PRE with an intensity decrease of > 90 % in the presence of paramagnetic MTSL-PTN. Residues G247 also showed measurable decreases in its intensity, but to a lesser degree (Figure 4.3B). Since both residues are close to MIDAS (Figure 4.3C), these results indicate MIDAS is the primary binding site for PTN. A control experiment has also been carried out using free MTSL to ensure the paramagnetic effect is not because of non-specific interactions between MTSL and α_M I-domain. As expected, free MTSL does not produce the strong paramagnetic perturbation observed with MTSL-labeled PTN (Figure 4S2).

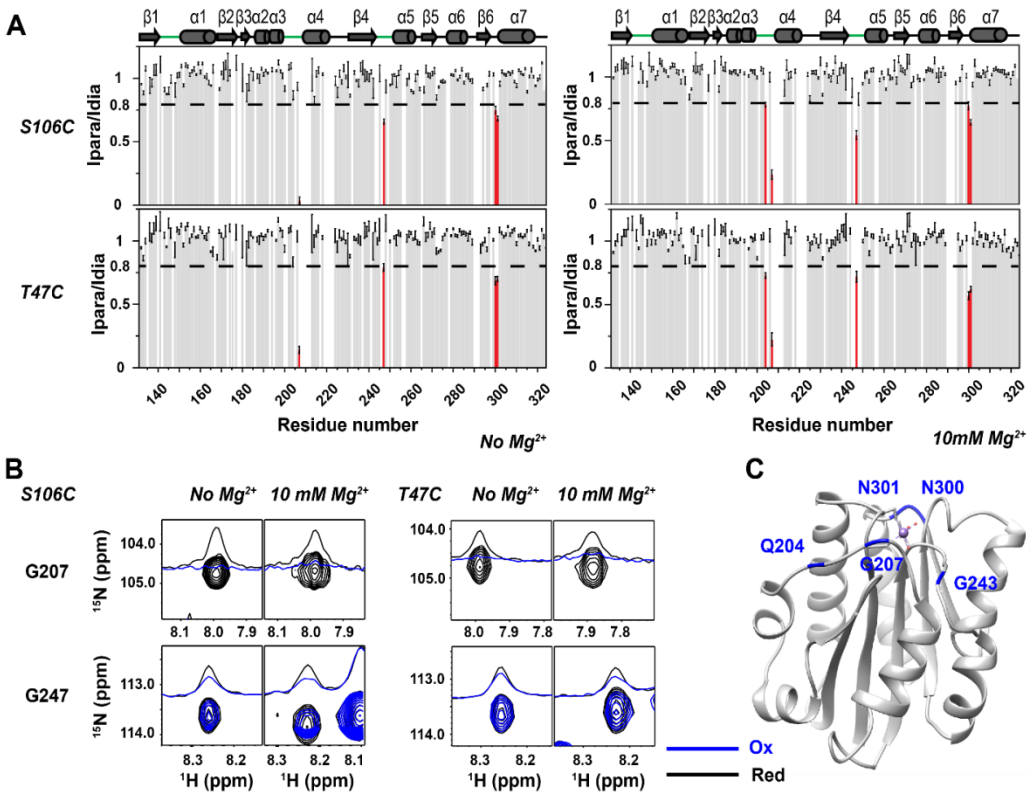

Figure 4.3 Effects of Paramagnetic PTN on HSQC of α_M I-domain.
(A), Residue specific intensity decreases induced by MTSL-labeled PTN. Secondary structures of α_M I-domain as well as segments forming the MIDAS (in green) are indicated on top of bar charts. Uncertainty in intensity ratio is calculated using the formula $\frac{I_{para}}{I_{dia}}\sqrt{(\frac{\Delta I_{dia}}{I_{dia}})^2+(\frac{\Delta I_{para}}{I_{para}})^2}$. (B), Sections of α_M I-domain ^{15}N HSQC spectra in the presence of either paramagnetic (blue) or diamagnetic (black) MTSL-labeled PTN. (C) Ribbon representation of α_M I-domain showing the positions of residues with the strongest PRE.

To carry out these PRE experiments, two samples of ^{15}N-labeled α_M I-domain mixed with six molar equivalents of MTSL-PTN were prepared. MTSL in one of the samples was kept in the paramagnetic state while MTSL in the other was reduced to the diamagnetic nitroxyl form using ascorbic acid. ^{15}N HSQC spectrum was acquired for each sample and peak intensity of each signal was then tabulated. Figure 4.3A shows

sections from HSQC spectra of α_M I-domain in the presence of paramagnetic and diamagnetic S106C-tagged MTSL-PTN. S106 is located in the C-terminal domain (CTD) of PTN and PRE effects from this mutant are indicative of closeness of the CTD to α_M I-domain. This version of MTSL-PTN produced significant PRE effects on residues close to MIDAS. Specifically, G207 in the second MIDAS segment has the most significant PRE with an intensity decrease of > 90 % in the presence of paramagnetic MTSL-PTN. Residues G247 also showed measurable decreases in its intensity, but to a lesser degree. Since both residues are close to MIDAS, these results indicate MIDAS is the primary binding site for PTN. A control experiment has also been carried out using free MTSL to ensure the paramagnetic effect is not because of non-specific interactions between MTSL and α_M I-domain. As expected, free MTSL does not produce the strong paramagnetic perturbation observed with MTSL-labeled PTN (Figure 4S2).

PTN is composed of two structured domains with similar folds (15). Previous study showed the N-terminal domain (NTD) and CTD can bind α_M I-domain independently, but CTD's affinity for α_M I-domain is higher than that of NTD (11). To determine if NTD of PTN binds to the same site on α_M I-domain as CTD, we also prepared the T47C PTN mutant, which allows us to place the MTSL tag on NTD. Similar PRE experiments showed the T47C mutant perturbed the same set of α_M I-domain residues as the S106C mutant (Figure 4.3). Interestingly, the magnitude of PRE from NTD-tagged PTN is similar to that of the CTD-tagged mutant even though NTD is known to have a lower affinity for α_M I-domain than CTD. This result is likely due to several factors. Specifically, the location of the NTD MTSL tag may be closer to α_M I-

domain than the CTD MTSL tag, allowing it to produce similar levels of perturbation despite its lower affinity. It is also possible that NTD and CTD in wild type PTN is not as independent as once assumed, thereby allowing NTD in wild type PTN to have as high an affinity for α_M I-domain as CTD in wild type PTN. It is also possible that, because PTN's concentration is high, NTD can saturate α_M I-domain even with its lower affinity.

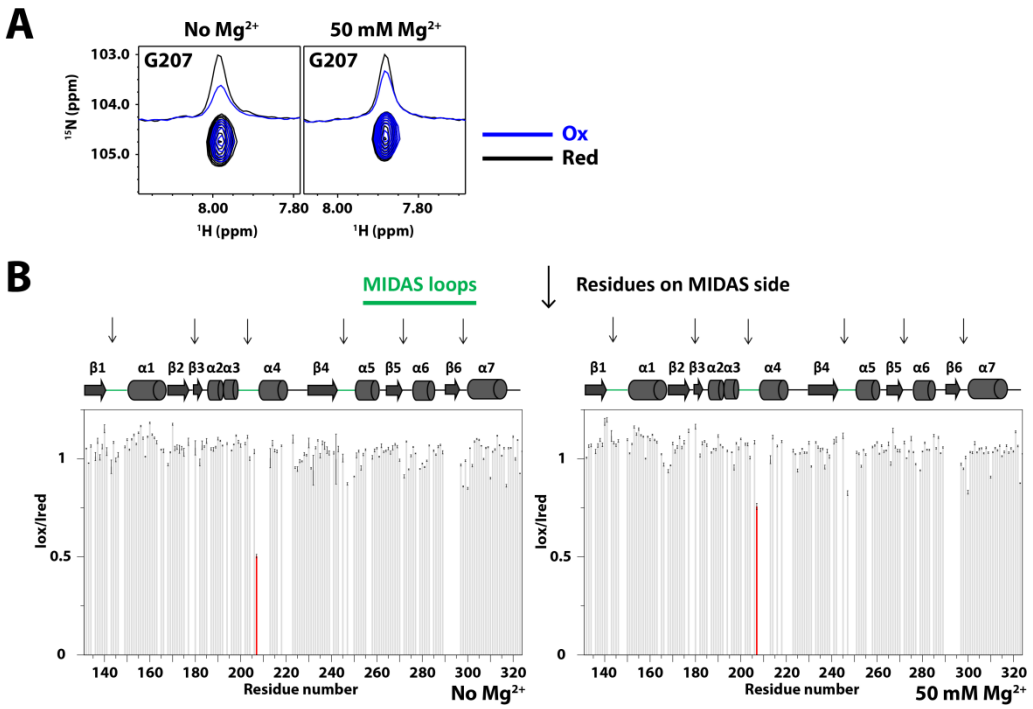

Figure 4.4 Effects of 50 mM Mg^{2+} on PTN's Interaction with α_M I-domain.
(A), Sections of α_M I-domain HSQC spectra in the presence of one molar equivalents of either paramagnetic (blue) or diamagnetic (black) PTN whose CTD contains the MTSL tag. 50 mM Mg^{2+} induced significant decreases in the observed PRE G207. (B), Residue specific intensity decreases induced by CTD MTSL-labeled PTN in the absence and presence of 50 mM Mg^{2+}. Secondary structures of α_M I-domain as well as residues and regions forming the MIDAS are indicated on top of bar charts. G207 is shown in red. Uncertainty in intensity ratio is calculated using the formula $\frac{I_{para}}{I_{dia}}\sqrt{(\frac{\Delta I_{dia}}{I_{dia}})^2+(\frac{\Delta I_{para}}{I_{para}})^2}$.

MST results showed high Mg^{2+} concentrations can inhibit the binding of PTN to α_M I-domain. To confirm these data, we also investigated the effect of Mg^{2+} on

interactions of α_M I-domain with PTN using NMR. Interestingly, even though MST showed 50 mM Mg^{2+} weakens PTN-α_M I-domain interactions considerably, this effect was not initially observed in the PRE experiments. We attribute this to the high concentration of PTN used in NMR experiments, which leaves most of α_M I-domain in the PTN-bound form even with a binding Kd of 50 µM. On the other hand, the fraction of PTN-bound α_M I-domain decreases to only 54 % if the PTN concentration is reduced to just one molar equivalent. This difference is sufficiently large to be detected by NMR. We therefore compared signal intensities of α_M I-domain in the presence of only one molar equivalent of either paramagnetic or diamagnetic MTSL-PTN. The data showed presence of 50 mM Mg^{2+} reduced perturbation to G207 significantly as PRE-related intensity decrease reduced from ~50 % to 25 % when Mg^{2+} concentration is high (Figure 4.4). This provides additional support for competitive binding between cationic peptides and Mg^{2+} ions.

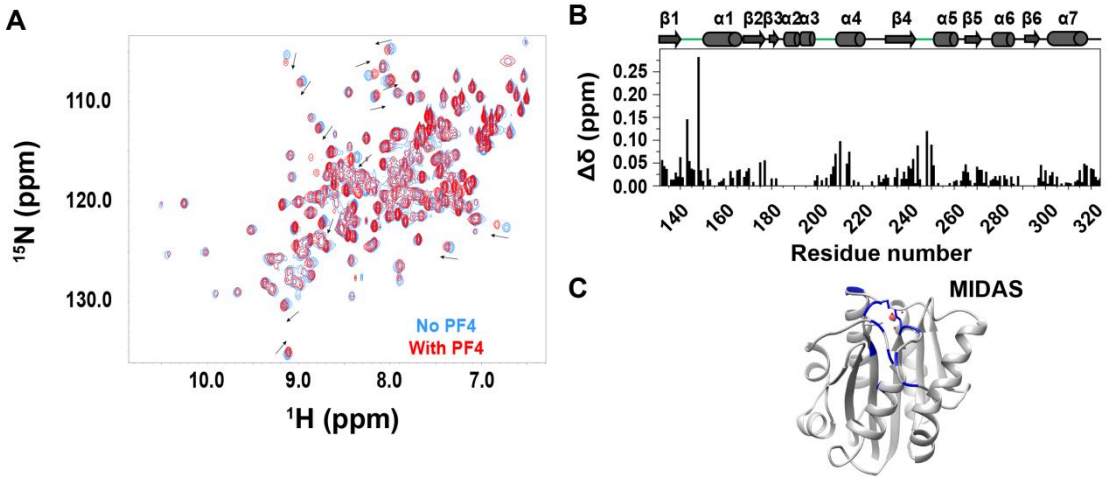

Figure 4.5 PF4-induced Chemical Shift Changes in ^{15}N HSQC Spectrum of α_M I-domain. (A), ^{15}N-HSQC spectra of α_M I-domain in the presence (red) and

absence (blue) of 3.3 molar equivalents of PF4. No Mg^{2+} is present in the buffer. (B), Residue specific chemical shift changes in α_M I-domain. Chemical shift changes are calculated as $\sqrt{\Delta H^2 + (0.25 * \Delta N)^2}$. Secondary structures of α_M I-domain as well as residues and regions forming the MIDAS are indicated on top of bar charts. (C), Ribbon representation of α_M I-domain showing positions of residues with significant PF4-induced chemical shift changes.

4, NMR analysis of PF4-α_M I-domain interactions

PF4 is another highly positively charged protein that has been identified as a potent ligand of Mac-1 capable of inducing Mac-1-dependent activation of macrophage and neutrophils (12). We examined interactions of PF4 with α_M I-domain using the same suite of NMR experiments used to study PTM-α_M I-domain interactions. Interestingly, unlike PTN, PF4 did induce measurable changes in the ^{15}N HSQC spectrum of α_M I-domain (Figure 4.5). Most residues perturbed by PF4 are also located around MIDAS, indicating the PF4 binding site is also close to MIDAS. In addition, the set of residues perturbed by PF4 overlaps significantly with the set of residues perturbed by Mg^{2+} binding (Figure 4S3). Chemical shift mapping also revealed that MIDAS residues, especially three loops containing direct coordinating residues, are the Mg^{2+} binding sites as they have the most significant chemical shift change upon metal bindings. The perturbation pattern is similar to α_1 I domain (23). This is also consistent with MIDAS being the binding site for PF4.

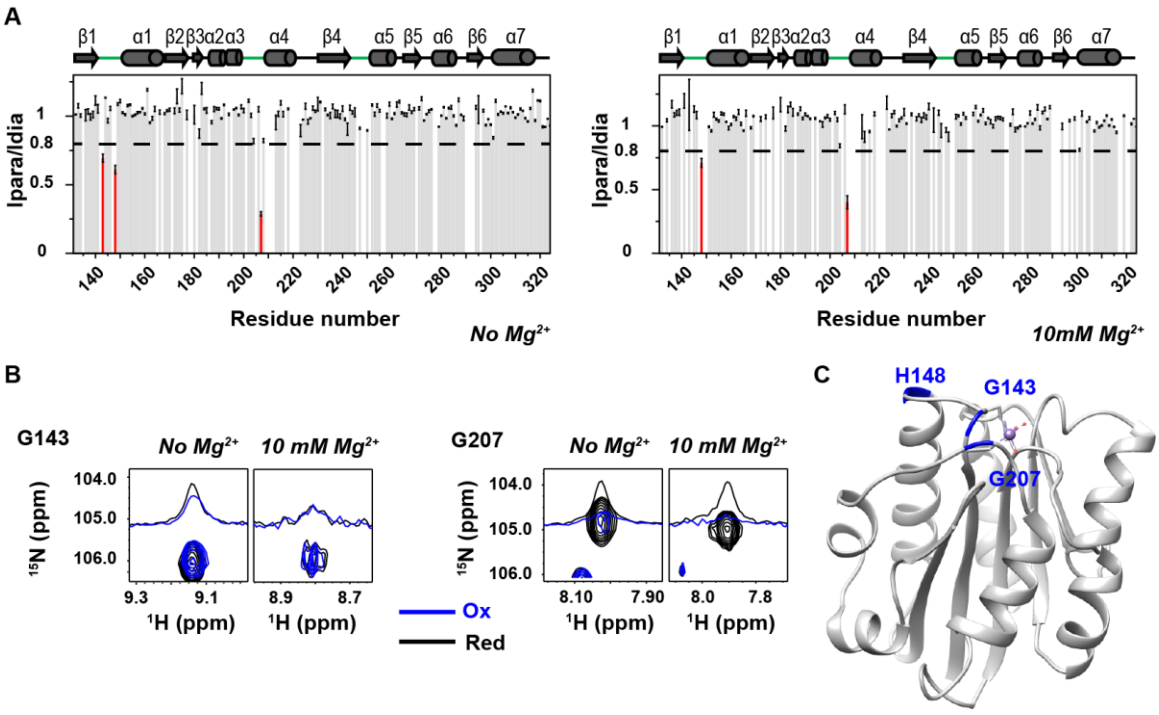

Figure 4.6 Effects of Paramagnetic PF4 on HSQC of α_M I-domain.
(A), Residue specific intensity decreases induced by CTD MTSL-labeled PTN. Note that 10 mM Mg^{2+} does not have a significant effect on the binding of these ligands. Secondary structures of α_M I-domain as well as residues and regions forming the MIDAS are indicated on top of bar charts. Residues having intensity decrease greater than 15 % are shown in red. Uncertainty in intensity ratio is calculated using the formula $\frac{I_{para}}{I_{dia}}\sqrt{(\frac{\Delta I_{dia}}{I_{dia}})^2+(\frac{\Delta I_{para}}{I_{para}})^2}$. (B), Sections of α_M I-domain HSQC spectra in the presence of 3.3 molar equivalents of either paramagnetic (blue) or diamagnetic (black) PF4. (C), Ribbon representation of α_M I-domain showing the positions of residues with the strongest PRE.

To confirm results from chemical shift mapping, we probed α_M I-domain with a PF4 variant containing the S17C mutation, which can anchor the paramagnetic MTSL tag close to the N-terminus of the protein. Similar to PTN, addition of MTSL-labeled PF4 strongly perturbed residue G207 close to the MIDAS (Figure 4.6). Residue G143 was also perturbed significantly by MTSL-labeled PF4. Once again, both residues are close to

MIDAS and the perturbation pattern agrees with the hypothesis that MIDAS is the binding site for cationic ligands.

To understand how Mg^{2+} ions affect PF4-α_M I-domain interaction, we measured the effect of different concentrations of Mg^{2+} on interactions between α_M I-domain and PF4. Similar to PTN, 10 mM Mg^{2+} does not change the PRE magnitude elicited by MTSL-labeled PF4. However, 10 mM Mg^{2+}, which was sufficient to completely eliminate signals from metal free α_M I-domain in the presence of six molar equivalents of PTN, produced two sets of signals in α_M I-domain's ^{15}N HSQC spectrum even when less than four equivalents of PF4 are present. Comparison with the spectrum of metal free α_M I-domain in the presence of PF4 showed signal doubling is the result of incomplete Mg^{2+} saturation since one set of signals corresponds to metal free α_M I-domain while the other set agrees with the Mg^{2+}-bound form of α_M I-domain (Figure 4.7). The reason for signal doubling was confirmed when two sets of signals coalesced into a single set of signals when Mg^{2+} ion concentration was increased to 50 mM. These results indicate PF4 interferes with Mg^{2+} binding and are consistent with MIDAS being the binding site for both PF4 and the Mg^{2+} ion.

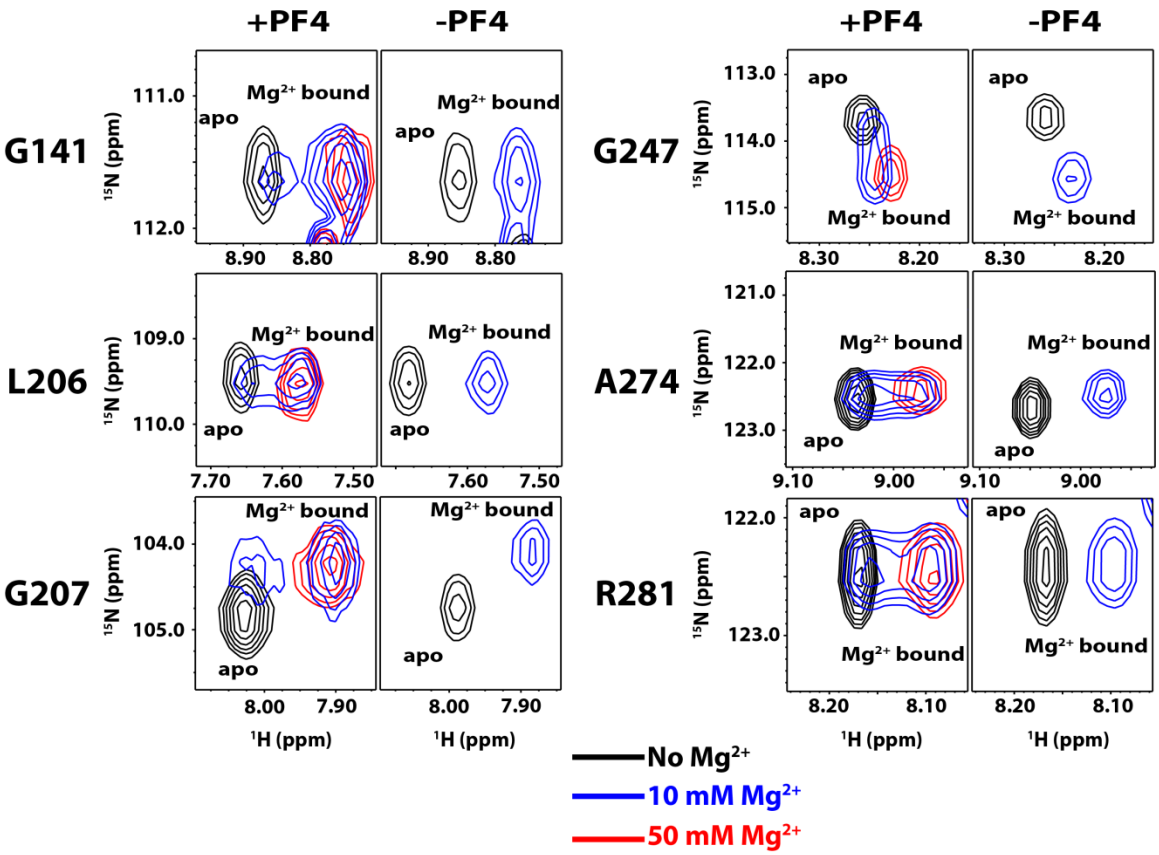

Figure 4.7 PF4 Inhibits Mg^{2+} Binding of α_M I-domain.
Selective signals in the HSQC of α_M I-domain at 0, 10 and 50 mM Mg^{2+}. These residues display double resonances in the presence of 10 mM Mg^{2+}. The chemical shifts of the two resonances are consistent with existence of a significant population of Mg^{2+}-free α_M I-domain. Signals from this population were not seen at 50 mM Mg^{2+}.

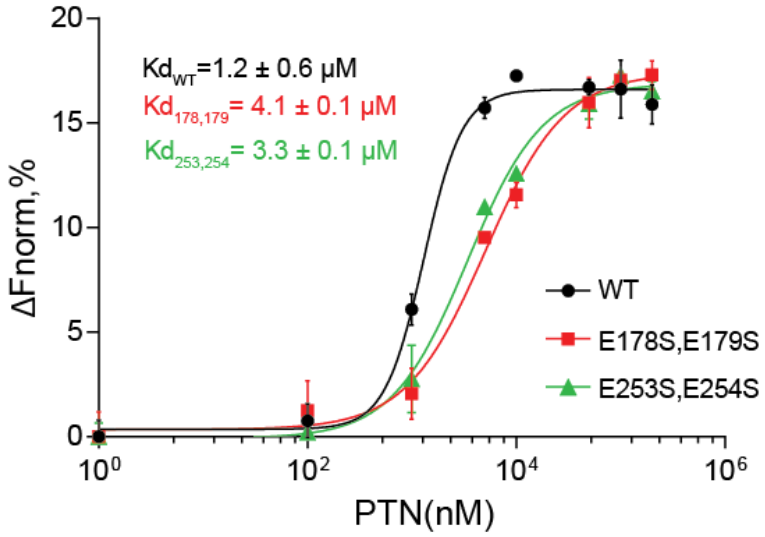

Figure 4.8 Effects of Acidic Amino Acid Mutations on the Binding Affinity of PTN to α_M I-domain.
MST-derived binding curves of PTN to E178,179S α_M I-domain as well as E253S/D254S α_M I-domain. Both sets of mutations measurably reduce affinity of α_M I-domain for PTN.

5, Conformation of α_M I-domain is not changed by ligand binding

Activation of Mac-1 leads to conformation changes in α_M I-domain that includes a shift of the C-terminal helix away from MIDAS (24). This conformation change is believed to be crucial to increasing the ligand affinity of α_M I-domain in metal-mediated interactions. To understand whether the binding of cationic ligands can produce similar changes in the conformation of α_M I-domain, we mutated residue G321 at the C-terminus of α_M I-domain to cysteine. This allows attachment of MTSL to the C-terminus of α_M I-domain. Our hypothesis is that shift of the C-terminal helix away from the protein should lead to a decrease in its paramagnetic effect on nearby residues, which can be easily detected by NMR. To test this, we measured intramolecular PRE of the MTSL tag on α_M

I-domain in the presence and absence of four molar equivalents of PF4. Figure 4.9 shows the results from these experiments. It is clear that presence of PF4 did not have a significant effect on intramolecular PRE from the MTSL tag, indicating PF4 binding does not change the conformation of α_M I-domain.

4.5 Discussion

MST experiments carried out in this study demonstrated for the first time that, not only are cationic ligands' interactions with α_M I-domain independent of divalent cations, high concentrations of divalent cations in fact inhibit binding of these ligands to α_M I-domain. Solution NMR studies of the same systems have convincingly identified MIDAS as the binding site of these ligands. This is not a surprise because many of the cationic ligands are known to seek out negatively charged regions on receptors and MIDAS in α_M I-domain has several negatively charged amino acid clusters in its vicinity. The dominance of electrostatic interactions between α_M I-domain and the ligands explains why high divalent cation concentrations inhibit the binding. It is worth noting that, although there is one report of α2 I-domain MIDAS being the binding site of a cationic peptide (7), this is the first study to demonstrate ligands can bind α I-domains using a completely metal independent mechanism. This mechanism differs significantly from the canonical ligand binding mechanism of integrin I-domains, which stipulates that ligands must bind I-domain through divalent cation mediated interactions that involve acidic amino acids from both the ligand and α I-domain MIDAS, thereby allowing the metal to act as a glue between the ligand and α I-domain. In contrast to the canonical mechanism, interactions between cationic ligands and α_M I-domain are unaffected by the absence of

divalent cations and physiological concentrations of Mg^{2+} does not increase ligand binding at all. At high Mg^{2+} concentrations, the affinity of α_M I-domain for cationic ligands is weakened considerably as Mg^{2+} is able to compete for the same binding site as the cationic ligands. Additional experiments carried out using α_M I-domain mutants missing some of the acidic amino acid clusters around MIDAS show these amino acids do indeed participate in binding. Interestingly, two of the amino acids investigated, E253 and D254, were also identified as important in defining α_M I-domain's ligand specificity in a previous study (8). It should also be noted that basic amino acids in ligands do play important roles in αL I-domain's interaction with ICAM-1 as well as in α_M I-domain's interaction with iC3b, even though both interactions follow the canonical mechanism as well (6,25). However, it appears that α_M I-domain has also evolved to have a sufficient amount of electronegativity around its MIDAS to bind ligands without the help of divalent cations.

These cationic ligands are by no means equivalent to each other. Although both PTN and PF4 bind to the same site on α_M I-domain. There are significant differences in how they interact with α_M I-domain. In particular, PF4 was able to prevent Mg^{2+} binding to α_M I-domain to a significant degree. Because lowered Mg^{2+} affinity would make Mg^{2+} less effective in neutralizing MIDAS, this may explain why Mg^{2+}-induced decreases in PF4 affinity has the same magnitude as NaCl. PF4 was also able to elicit considerable chemical shift changes in the ^{15}N HSQC spectrum of α_M I-domain, which PTN was not able to do. This indicates PF4's interaction with α_M I-domain may be more specific and stable than that of PTN.

All experiments in this study were conducted using wild type α_M I-domain, which adopts the inactive conformation. The fact that these cationic ligands are able to bind the domain even when it is in the inactive conformation implies their affinity for the active conformation of the α_M I-domain should be even higher. Our previous biolayer interferometry studies of both PTN and PF4's interactions with active and inactive α_M I-domain showed this is indeed the case (11,12). However, this does not mean only activated α_M I-domain can bind the ligands. In particular, both PTN and PF4 are avid binders of glycosaminoglycans and are believed to be displayed in oligomeric or aggregated forms in the extracellular space as a result of these interactions (26,27). These large multivalent aggregates would have much higher affinity for inactive α_M I-domain as a result of avidity of interaction. This potentially makes inactive Mac-1 a viable receptor for the ligands. The fact that these ligands are immobilized on cell surface or in the extracellular matrix is also consistent with current model of integrin activation (28). It is also interesting to note that there is currently no evidence that binding of these ligands to α_M I-domain can shift the conformational equilibrium of α_M I-domain towards the active conformation despite numerous cell-based assays showing these ligands are capable of activating Mac-1 (11,12). One possible mechanism by which these ligands can activate Mac-1 is through ligand-induced Mac-1 clustering. Oligomeric forms of these ligands can bind multiple integrin receptors, potentially inducing their clustering. Since it is well known that clustering of integrins is essential to activation of integrin associated Src family of phosphotyrosine kinases and subsequently to activation of other pathways

(2,29), binding of Mac-1 to the oligomeric forms of these cationic ligands should activate intracellular signaling even if the receptors may not be in the active form.

I-domain should be even higher. Our previous biolayer interferometry studies of both PTN and PF4's interactions with active and inactive α_M I-domain showed this is indeed the case (11,12). However, this does not mean only activated α_M I-domain can bind the ligands. In particular, both PTN and PF4 are avid binders of glycosaminoglycans and are believed to be displayed in oligomeric or aggregated forms in the extracellular space as a result of these interactions (26,27). These large multivalent aggregates would have much higher affinity for inactive α_M I-domain as a result of avidity of interaction. This potentially makes inactive Mac-1 a viable receptor for the ligands. The fact that these ligands are immobilized on cell surface or in the extracellular matrix is also consistent with current model of integrin activation (28). It is also interesting to note that there is currently no evidence that binding of these ligands to α_M I-domain can shift the conformational equilibrium of α_M I-domain towards the active conformation despite numerous cell-based assays showing these ligands are capable of activating Mac-1 (11,12). One possible mechanism by which these ligands can activate Mac-1 is through ligand-induced Mac-1 clustering. Oligomeric forms of these ligands can bind multiple integrin receptors, potentially inducing their clustering. Since it is well known that clustering of integrins is essential to activation of integrin associated Src family of phosphotyrosine kinases and subsequently to activation of other pathways (2,29), binding of Mac-1 to the oligomeric forms of these cationic ligands should activate intracellular signaling even if the receptors may not be in the active form.

CHAPTER 5

CONFORMATIONAL DYNAMICS OF INTEGRIN α_M I-DOMAIN

5.1 Abstract

Mac-1 has a broad spectrum of ligands and is one of the most promiscuous members of the integrin family. α I-domain, as the primary ligand binding site, has interesting conformational dynamics not seen in other α I-domains. Using NMR relaxation dispersion experiments, μs-ms timescale motions were discovered in α_M I-domain. Specifically, the slow motions are intrinsic in MIDAS, the ligand binding site of the α I-domain. Mg^{2+} induced motions at similar time scales are also found in the crucial α7 helix. These motions hint at a possible role played by dynamics in ligand binding as well as integrin activation.

5.2 Introduction

Proteins are macromolecules with intrinsic and functional motions. The motions include both backbone and side chain bond rotations that can modulate important events such as allosteric regulation, ligand interactions etc. The dynamics processes fall into different time regimes. They can range from picosecond to nanosecond (ps-ns) and microsecond to millisecond (μs-ms). Nuclear magnetic resonance (NMR) has emerged as a powerful tool as it is capable of probing a wide range of motional timescales with different experiments (1,2). Figure 5.1 displays an overview of protein motion timescales and specific NMR experiments for them. The most frequently explored motions are fast (ps-ns) and slow (μs-ms).

Briefly, fast motions (ps-ns) are probed with R_1, R_2 and heteronuclear NOE (nuclear Overhauser effect) experiments. R_1 refers to longitudinal relaxation rate of magnetization along the static magnetic field from excited state to equilibrium while R_2 represents transverse relaxation rate of transverse magnetization coherence dephasing (3). Both R_1 and R_2 relaxations stem from variations in local magnetic field due to chemical shift anisotropy (CSA) and dipolar coupling, and are dependent on both global and internal motions of proteins (4,5). The NOE is the steady state NOE enhancement due to dipolar cross relaxation, which is also dependent on protein motion (6). In practices, R_1, R_2 and heteronuclear NOE are measured in combination and the data can be subjected to the Lipari-Szabo model free analysis (7,8). The order parameter S^2 , a parameter for local motion amplitude, and correlation time τ_c for each residue can be obtained through such an analysis (9). This approach was explored in Chapter 2 to examine the effect of glycosaminoglycan bindings on the conformational dynamics of DBPB.

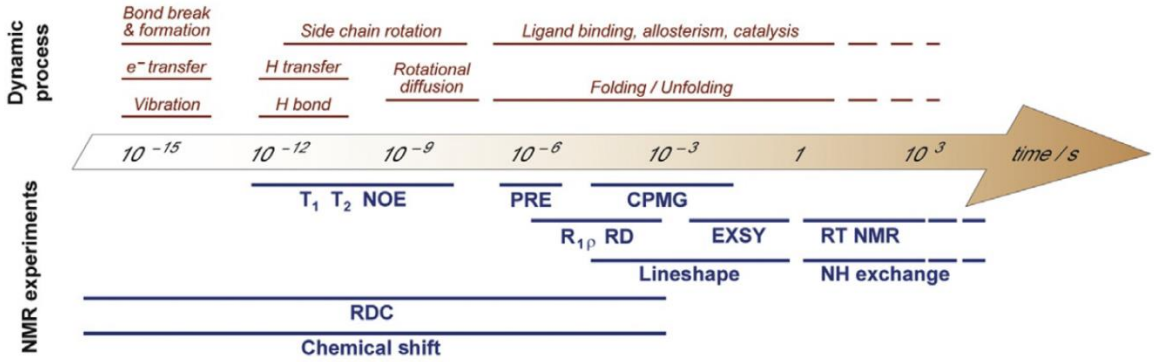

Figure 5.1 Protein Motions at Various Timescales and NMR Techniques for Each Timescale
Reprinted with permission from Ortega, G., Pons, M., and Millet, O. (2013) Protein functional dynamics in multiple timescales as studied by NMR spectroscopy. Advances in protein chemistry and structural biology 92, 219-251. Copyright (2013) Elsevier. See Appendix J.

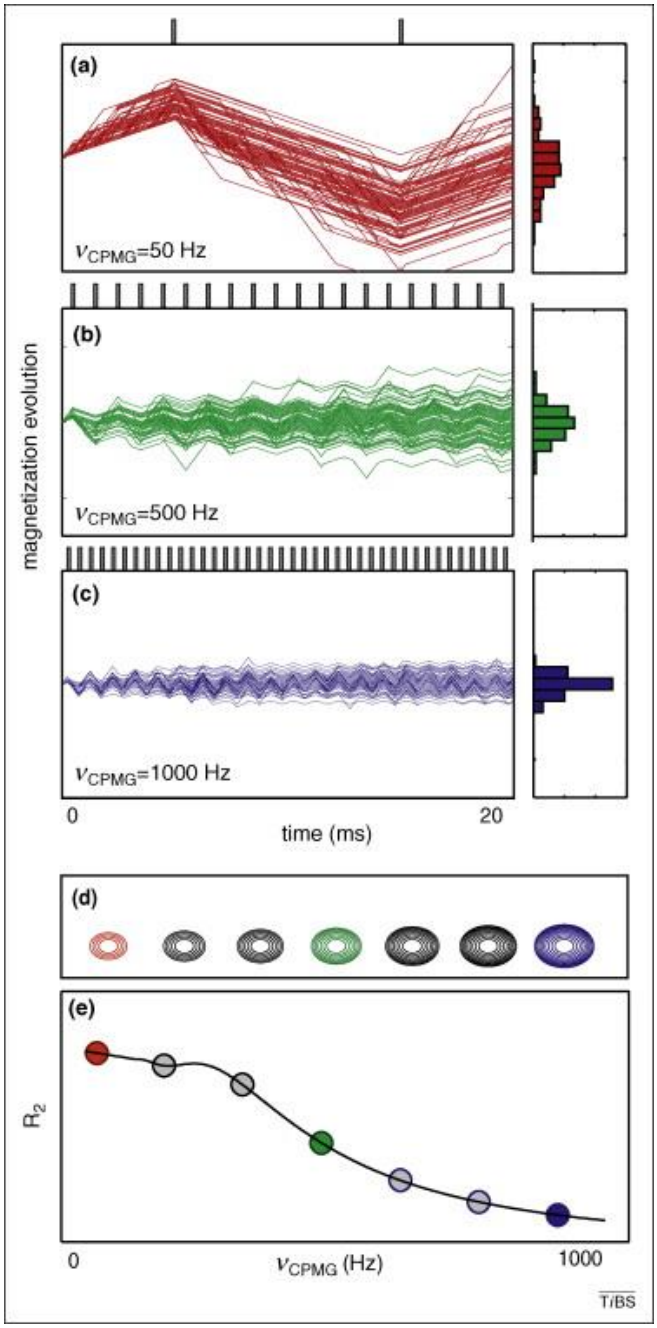

Figure 5.2 Signal Intensity Changes under Various ν_{CPMG} in CPMG Relaxation Dispersion Experiments.
(a-c), signal traces simulated for group of nuclei exchanging between two states with different chemical shifts during 20 ms of relaxation delay (T_{CPMG}). Vertical bars are 180° refocusing pulses. (d), Signal intensity increase with higher ν_{CPMG} in simulation. (e), R_2 is plotted against $\nu_{CPMG}=1/(2\tau_{cp})$. τ_{cp} is the delay between consecutive 180° refocusing pulses.
Reprinted with permission from Mittermaier, A. K., and Kay, L. E. (2009) Observing

biological dynamics at atomic resolution using NMR. Trends in biochemical sciences 34, 601-611. Copyright (2009) Elsevier. See Appendix K.

Other than CSA and dipolar coupling, R_2 rate can also be influenced by slow time scale conformational and chemical exchanges. In particular, changes in conformation and chemical state may cause spins to constantly switch between different magnetic environments and thus have different chemical shifts. Exchanges might also arise from ligand bindings. If the exchange happens at the appropriate NMR time scale (μs-ms), it leads to faster loss of magnetic moment coherence, thereby increasing the R_2 of the atom. This additional term to the intrinsic transverse relaxation rate R_2^0, R_{ex}, leads to a larger transverse relaxation rate R_2 and therefore line broadening (10). The calculation of R_2 in NMR spectra with chemical exchange processes is described by the Bloch-McConnell Equations (11). Abergel et al. proposed approximate solutions to the Bloch-McConnell Equations for a two-state chemical exchange model as follows (12):

$$R_2 = \overline{R_2^0} + p_A p_B \Delta\omega^2 k_{ex} \times \left[\frac{k_{ex}^2 + \Delta\omega^2}{\left[k_{ex}^2 + \Delta\omega^2\right]^2 - p_A p_B (5k_{ex}^2 + \Delta\omega^2)\Delta\omega^2} \right]$$

$$\Omega = \bar{\Omega} - p_A p_B (p_A - p_B)\Delta\omega^3 \times \left[\frac{k_{ex}^2 + \Delta\omega^2}{\left[k_{ex}^2 + \Delta\omega^2\right]^2 - p_A p_B (7k_{ex}^2 + 3\Delta\omega^2)\Delta\omega^2} \right]$$

in which, $\overline{R_2^0} = p_A R_{2A} + p_B R_{2B}$, $\bar{\Omega} = p_A \Omega_A + p_B \Omega_B$; R_2 and Ω are the transverse relaxation rate and resonance frequency of the dominant signal respectively; ρ_A and ρ_B are populations of the major (A) and minor (B) states; $\Delta\omega$ is the difference between Ω_A and Ω_B, where Ω_A and Ω_B are resonance frequencies in states A and B without chemical exchange; R_{2A} and R_{2B} are the intrinsic transverse relaxation rates of A and B states.

Unlike the intrinsic R_2^0, effect of R_{ex} can be greatly mitigated if spins can be refocused in time through application of 180^o refocusing pulses. This provides a method by which motions at this timescale (μs-ms) can be quantified using the well-established Carr-Purcell-Meiboom-Gill (CPMG) scheme in experiments commonly referred to as relaxation dispersion (RD) experiments (13,14). Figure 5.2 illustrates how resonance signal intensity changes in response to varying ν_{CPMG} [reprinted from (15)]. An advantage of CPMG technique is that information on the functionally critical minor state (low populated) can be obtained by observing only the major state. This is extremely convenient since the minor state is often not observable in NMR spectra (2). The constant-time CPMG experiment is exploited to investigate the μs-ms motions of integrin α_M I-domain in the current study.

Conformational changes in integrin α I-domains are central to ligand bindings and activation (16,17). Specifically, during activation, α I-domain undergoes conformational changes, of which the most distinctive is the downward shift of the C-terminal α7 helix (16). The changes in the conformation of the α I-domain is accompanied by a drastic increase in the ligand affinity of α I-domains, making this a crucial event in the activation of integrins. Like other integrin α I-domains, α_M I-domains can reside either in the low ligand affinity state or the high ligand affinity state, as evidenced by crystal structures (18,19). This is also supported by studies using conformation-specific antibodies (20,21). Additional studies on the α_M I-domain has shown that residue I316 in the α7 helix has extensive interactions with a hydrophobic patch on the protein core, thereby stabilizing the position of the helix. To activate the α I-

domain, these hydrophobic interactions are disrupted so the position of α7 helix can be shifted away from the MIDAS. This observation has been exploited to produce α_M I-domain variants that stay in the high ligand affinity form, termed as "active" state. Specifically, α7 helix can be truncated from I316 to C terminus to disrupt the hydrophobic interactions; similar effects can also be produced with the I316G mutation; introduction of a disulfide bond between the α7 helix and the protein core can also increase ligand affinity of the domain (22-24). The disulfide bond lock α_M I-domain in active conformation by pushing down α7 helix, while truncation and mutation of I316 release the isoleucine from the hydrophobic socket to destabilize the inactive conformation. Crystal structures confirm the isoleucine displacement (22). The hydrophobic pocket with the buried isoleucine is also observed in the extracellular domains of inactive/bent-closed $\alpha_x\beta_2$ (25). These observations imply that engagement of α7 helix in the hydrophobic pocket is critical for activation regulation. In fact, α7 helix is not the only structural component with mobility. Mutations outside of the hydrophobic pocket on the surface close to N/C linkers were also reported to activate integrin α_M I-domains (21). In addition, residues in metal dependent adhesion site (MIDAS) were also suspected to be highly dynamic (19,26). This is especially crucial to the promiscuity of α_M I-domain, which needs to interact with different ligands (27,28). It is thus intuitive to assume local conformations in α_M I MIDAS are delicately and accurately tuned in an adaptive process to expose different residues for respective ligands. The first investigation of conformational dynamics in α I-domains using NMR techniques was reported by Nunes et al. (29). In their studies, using CPMG relaxation dispersion

experiments, μs-ms timescale dynamics were identified for residues in and close to MIDAS. They proposed that Mg^{2+} induced dynamics are critical for ligand interactions, structural arrangement and functions. As revealed in Chapter 3, significant unequal signal intensities were observed for α_M I-domain. This is indicative of the occurrence of conformational changes at μs-ms time scale. CPMG experiments are well suited for investigating dynamics on the slow timescale. Current work focuses on preliminary analysis of α_M I-domain dynamics with or without Mg^{2+} to probe intrinsic and Mg^{2+} induced motions. Our data indicate MIDAS residues exhibit strong motions in the μs-ms time scale, which is consistent with the need for α_M I-domain to interact with different ligands. We also noticed that Mg^{2+} binding led to increased dynamics in the α7 helix, which may provide mechanistic insights into the effect of divalent cations on integrin activation.

5.3 Materials and Methods

1, Integrin α_M I-domain expression and purification

Expression and purification of integrin α_M I-domain are previously described in Chapters 3 and 4.

2, CPMG relaxation dispersion (RD) experiments

CPMG data were recorded on 600 and 850 MHz Bruker AVANCE spectrometers with cryo-probes. Samples contain 0.5-1.0 mM ^{15}N integrin α_M I-domain and 10% D_2O in 20 mM HEPES, 150 mM NaCl buffer (pH 7.0) with or without 50 mM Mg^{2+}. ^{15}N RD experiments were performed using the relaxation compensated CPMG pulse sequences

developed by Loria et al. (30). The constant relaxation delay is 40 ms. Spectra of a reference and CPMG field strengths of 100, 150, 200, 250, 300, 400, 600 and 800 Hz were collected for apo (No Mg^{2+}) samples at 600 and 850 MHz. For 50 mM Mg^{2+} samples, the CPMG field strengths are 50, 100, 150, 200, 250, 300, 400, 600 and 800 Hz on the 600 MHz spectrometer, and 50, 100, 150, 200, 300, 500, 800 and 800 Hz on the 850 MHz spectrometer. Experiments were repeated for two υ_{CPMG} points for error analysis.

RD data were processed with NMRPipe and analyzed with NMRView (31,32). Peak intensities were extracted from ^{15}N HSQC spectra. R_2^{eff} is formulated as the equation $R_2^{eff}=1/T_{CPMG}\times\ln(I_0/I\upsilon_{CPMG})$. I_0 and $I\upsilon_{CPMG}$ are signal intensity in the reference spectrum and signal intensity when CPMG pulse is applied respectively. T_{CPMG} is the constant time delay (40 ms). Errors are the propagation of the signal-to-noise ratios of repeated measurements. Data were fitted using the GUARDD program (33). GUARDD fits data to the Carver-Richards equation, which defines how exchange contribution to transverse relaxation (R_{ex}) depends on the frequency of 180° refocusing pulses (υ_{CPMG}) (34). Fitting follows a two-state model described by the following equations (35):

$$R_2\left(\frac{1}{\tau_c}\right) = R_2^0 + \frac{1}{2}\left(k_{ex} - \frac{1}{\tau_c}cosh^{-1}\left[D_+cosh(\eta_+) - D_-cosh(\eta_-)\right]\right)$$

$$D_\pm = \frac{1}{2}\left(\pm 1 + \frac{\psi + 2\Delta\omega^2}{\left(\psi^2 + \xi^2\right)^{\frac{1}{2}}}\right)$$

$$\eta_\pm = \frac{\tau_{cp}}{\sqrt{2}}\left(\left(\psi^2 + \xi^2\right)^{\frac{1}{2}} \pm \psi\right)^{\frac{1}{2}}$$

$\psi\ k_{ex}^2 - \Delta\omega^2, \qquad \xi = -2\Delta\omega(p_A - p_B)$

In the above equations, p_A and p_B are populations for the major and minor states respectively. $\Delta\omega$ is the chemical shift difference between the two states. k_{ex} is the overall exchange rate. τ_{cp} is the time delay between 180° refocusing pulses ($\nu_{CPMG}=1/2\tau_{cp}$). R_2^0 is the intrinsic transverse relaxation rate.

R_{ex} is estimated using the equation: $R_{ex} \approx 1/T_{CPMG} \times \ln(I\tau_{cp1}/I\tau_{cp2})$, where $I\tau_{cp1}$ and $I\tau_{cp2}$ are resonance intensities when the highest and lowest CPMG frequencies are applied respectively. The approximations of R_{ex} were previously reported (35).

5.4 Results

1, μs-ms dynamics in Mg^{2+}-free state

To investigate the intrinsic conformational dynamics of integrin α_M I-domain, data on the apo sample was first collected. ^{15}N CPMG relaxation dispersion analysis is well suited to probe μs-ms motions in backbone amide nitrogen atoms (36,37). Without Mg^{2+}, a number of residues exhibit changes in R_{2eff} under different 180° refocusing pulse frequencies (υ_{CPMG}). As shown in figure 5.3, residues with high R_{ex} values are mostly located in MIDAS (the top surface) and the bottom surface where N and C termini are in the apo sample. This is clearly an indication that slow timescale motions exist. Residues were first fitted individually and then group-fitted by similar exchange rates and locations. The exchanged residues are concentrated in three regions, MIDAS, α7 helix and N/C termini region. Figure 5.4 illustrates relaxation dispersion profiles of residue in MIDAS. For apo samples, two groups of motions are observed in MIDAS. The first group includes

D140, Q204 and E244 while G272 is in the second group. Q204 and E244 are on MIDAS loops that contain directly metal coordinating residues. D140 is one of the five coordinating residues while G272 is slightly away from metal coordination site. Group fitting yields exchange rates (k_{ex}) of ~ 700 s^{-1} and ~ 1600 s^{-1} respectively for the two groups. Population of the major state (p_A) is ~ 94.0 % for the first group and ~ 98.5 % for G272. If the molecule has an overall concerted chemical exchange process, CPMG fittings would produce similar k_{ex} and p_A for all exchanged residues. Present results with different exchange parameters clearly suggest that multiple dynamics processes exist.

As shown in Figure 5.5, most residues on α7 helix, don't display relaxation dispersion, except for F317 and A318. L305, I308, Q309 and K315 do not have motions in the range (μs-ms) that are detectable in CPMG experiments. F317 and A318 are close to the hydrophobic pocket that stabilizes the inactive conformation (22). Group fittings of F317 and A318 produce a k_{ex} of ~ 240 s^{-1}, which represents rather slow motions. p_A for the two residues is ~ 96.5 %.

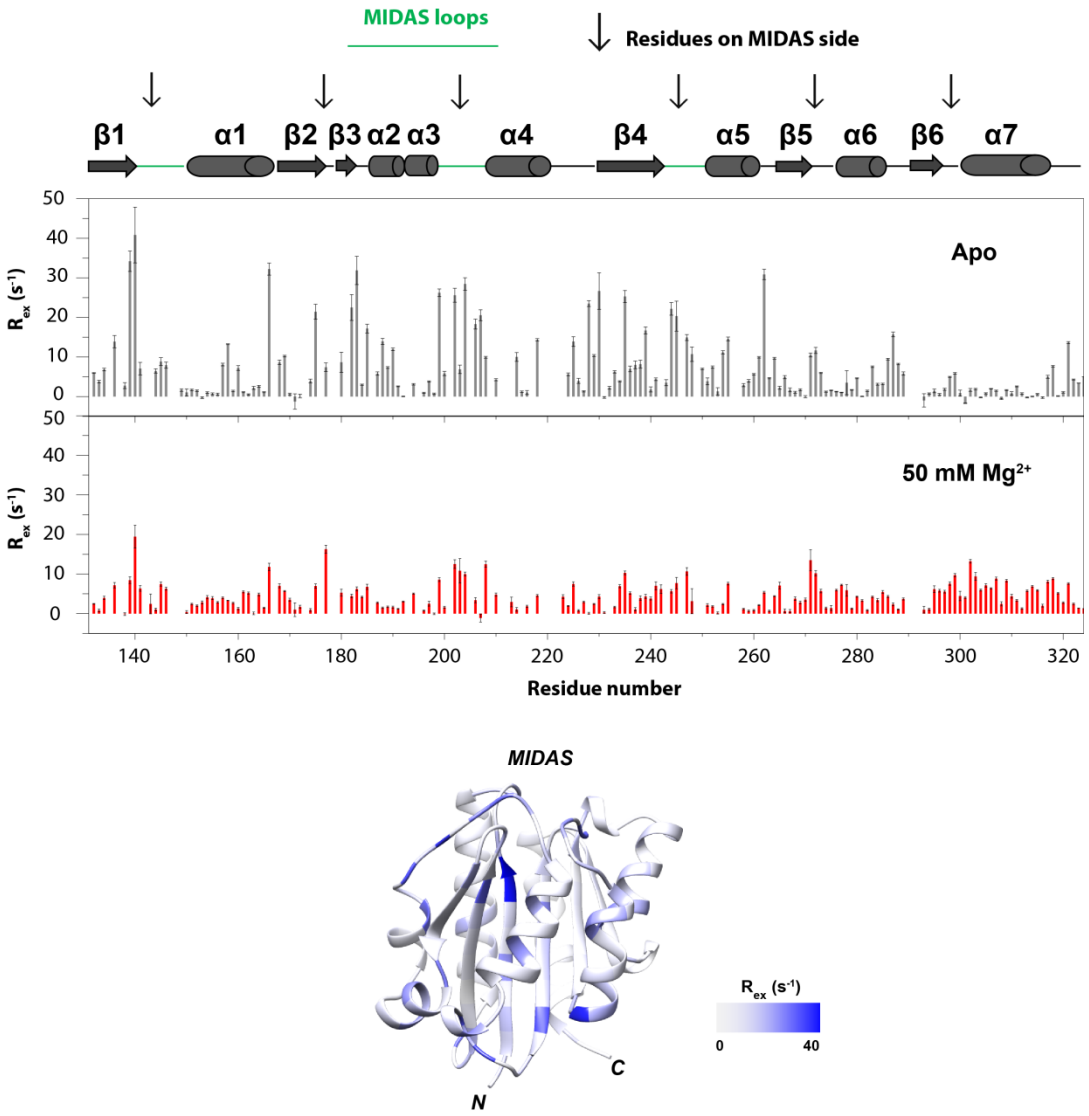

Figure 5.3 Effects of Mg^{2+} on R_{ex}.
Upper panels display R_{ex} obtained at 850 MHz from relaxation dispersion experiments for apo (gray bars) and 50 mM Mg^{2+}(red bars) containing samples. Secondary structures of α_M I-domain are placed on the top. Lower panel shows the ribbon representation of α_M I-domain with residues color-coded according to R_{ex} values (pdb: 1jlm).

As shown in Figure 5.3, other than MIDAS, some residues in the bottom surface of α_M I-domain also have high R_{ex} values. CPMG fittings suggest slow dynamics (k_{ex}= ~ 260 s^{-1}) for K235 and E262 in the bottom surface. E262 is on the α5-β5 loop while K235

is on the β4 strand close the hydrophobic pocket of α7 helix. p_A for the two residues is ~ 91.7 %. Relaxation dispersion profiles of the two residues are displayed Figure 5.6. All exchange parameter fits can be found in Table 5.1

2, μs-ms dynamics in Mg^{2+} bound state

Previous isothermal titration calorimetry (ITC) analysis (38) and Mg^{2+} titration in Chapter 3 both suggest that α_M I-domain has low affinity for Mg^{2+} (Kd=1.3 ± 0.3 mM). 50 mM Mg^{2+} was added to α_M I-domain samples to saturate Mg^{2+} bindings. Just like apo samples, two groups of motions with different exchange rates are also identified in MIDAS for Mg^{2+} containing samples, with one group faster than the other. Group fittings of D140, Q204 and E244 yields a k_{ex} of ~ 1100 s^{-1}. G272 in the second group has a k_{ex} of ~ 2100 s^{-1}. MIDAS residues collectively experience faster exchange in the presence of Mg^{2+}. Effects of Mg^{2+} on MIDAS dynamics are also reflected by exchange contributions to transverse relaxation (R_{ex}). For all MIDAS residues, R_{ex} is universally higher in apo samples than in Mg^{2+} containing samples. For D140, Q204 and E244, all of which are close to the Mg^{2+} binding site, R_{ex} in the apo sample is ~ 2-3 folds higher than that of the Mg^{2+} saturated sample. R_{ex} in the apo state is also higher, though not as much, for G272, which is distal to Mg^{2+} coordination site. Higher R_{ex} in the apo state most likely indicates faster exchange is induced by Mg^{2+}.

For α7 helix, Mg^{2+} has more significant effects on conformational dynamics. μs-ms motions were observed for many residues along the C-terminal helix in Mg^{2+} bound state. All residues in Figure 5.5 have shown fast exchange rates at the μs-ms time

scale with Mg^{2+}. In the first half of the helix, fittings yield a k_{ex} of ~ 1500 s^{-1} for F302, E303, L305 and Q309. Towards the end of the helix, K315, F317 and A318 are group-fitted, producing a k_{ex} of ~ 1000 s^{-1} and a p_A of ~ 98.2%. Comparison of apo and Mg^{2+} data concludes that Mg^{2+} induces fast dynamics (k_{ex} > 1000 s^{-1}) throughout α7 helix, which is more obvious for the first half of the helix that show no detectable relaxation dispersion in apo states. For residues close to the end of the helix, Mg^{2+} increases local exchange rates (k_{ex}) from ~ 270 to ~ 1000 s^{-1}. This is further supported by increased R_{ex} values in the presence of Mg^{2+}, as shown in Figure 5.3.

Interestingly, just like for MIDAS residues, Mg^{2+} also induces faster exchange processes in the bottom surface of α_M I-domain. With Mg^{2+}, K235 and E262 exhibit an exchange rate (k_{ex}= ~ 480 s^{-1}), almost twice as high as what's observed for apo samples (k_{ex}= ~ 260 s^{-1}). R_{ex} reveals a 3-4 fold decrease when Mg^{2+} is present. This is inconsistent with faster exchanges induced by Mg^{2+}. p_A is ~95.8% for K235 and E262. Relaxation dispersion profiles for the two residues are shown in Figure 5.6. All fitted parameters are listed in Table 5.1.

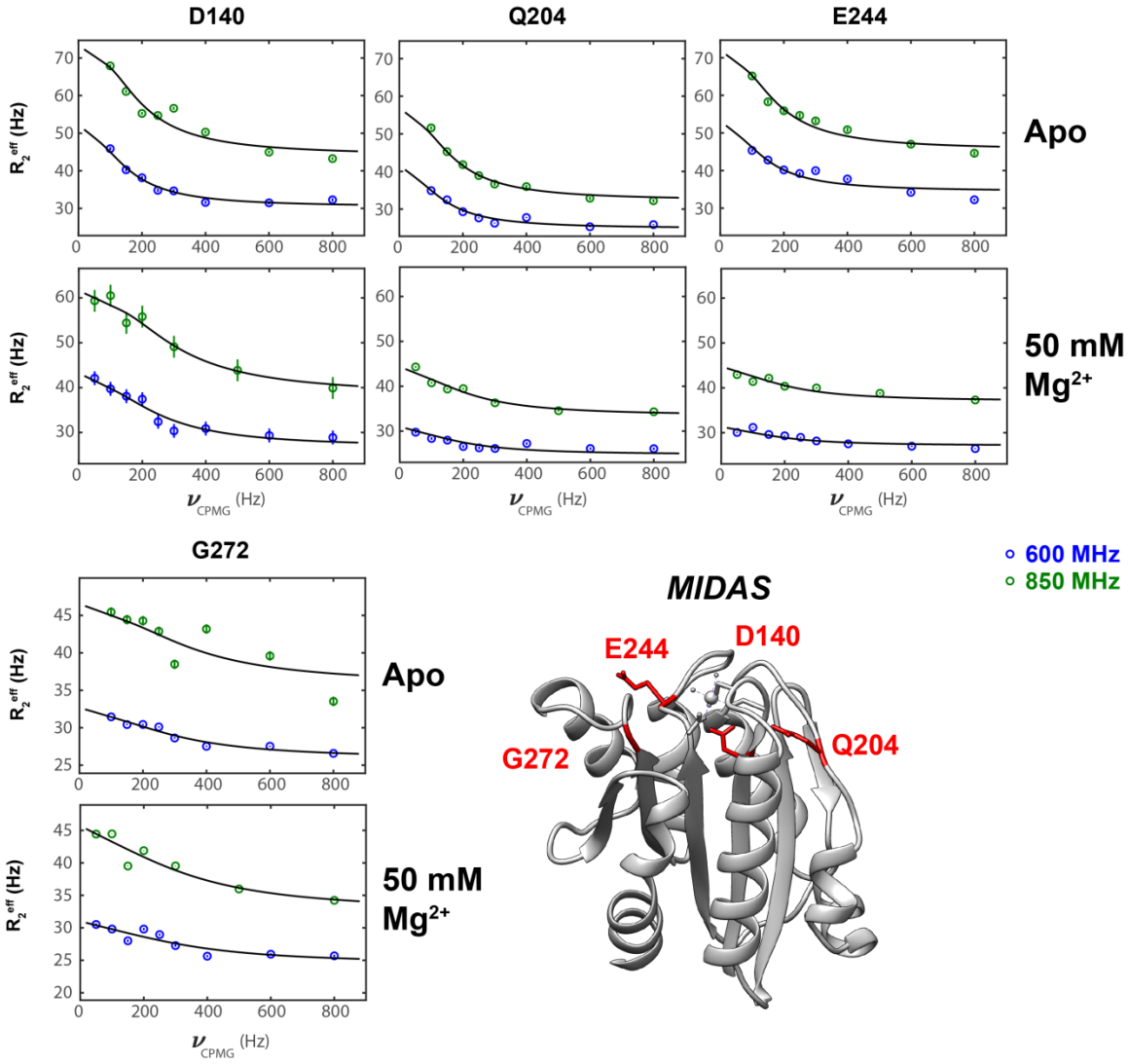

Figure 5.4 Relaxation Dispersion Profiles of Residues in MIDAS in Apo and Mg^{2+} Bound States.

The upper two panels are D140, Q204 and E244 with faster exchange rates (k_{ex}) than G272 in lower two panels. These four residues are colored red in α_M I-domain structure (pdb: 1jlm).

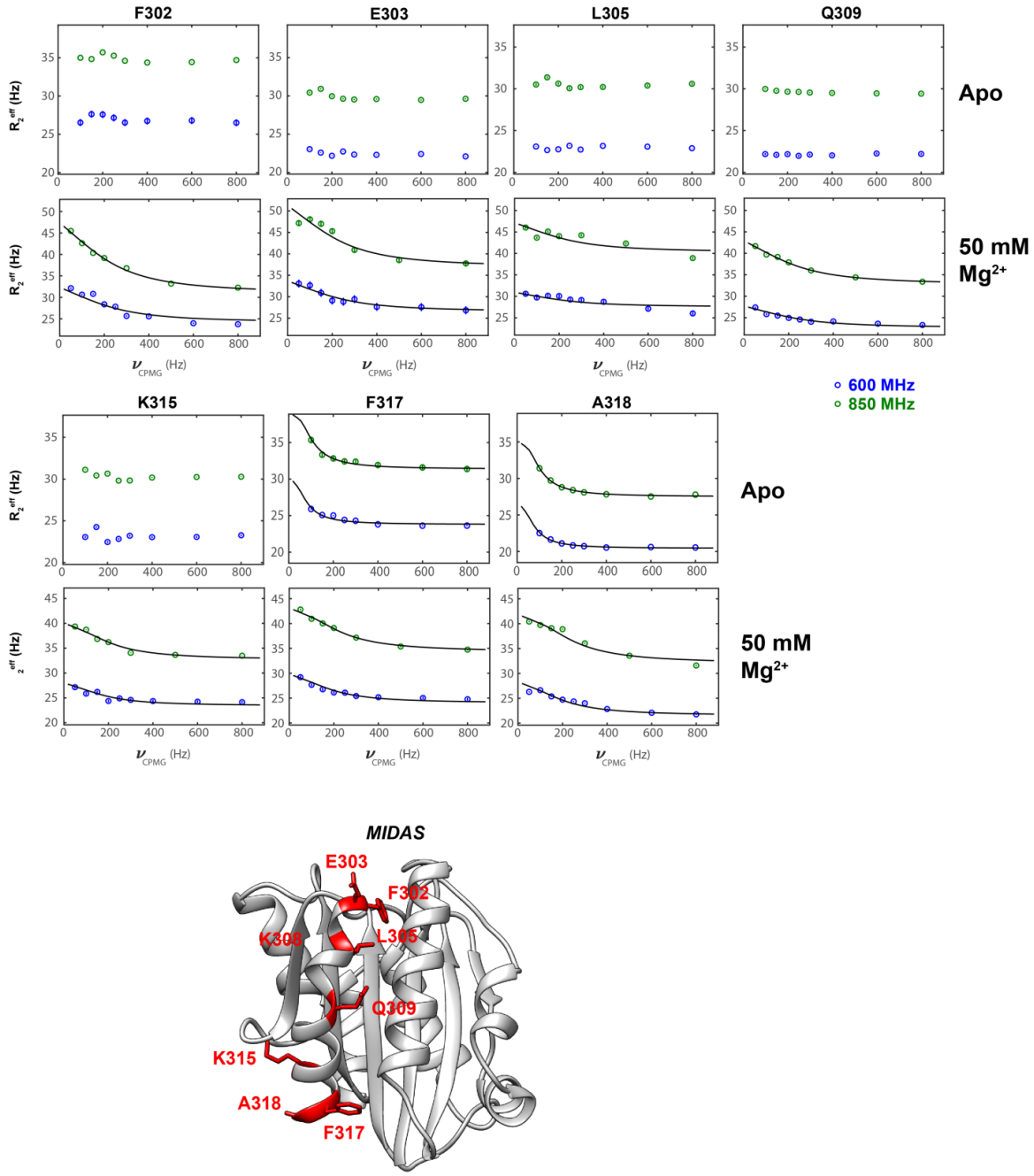

Figure 5.5 Relaxation Dispersion Profiles of Residues in C-terminal α7 helix in Apo and Mg^{2+} Bound States.
The upper two panels are F302, E303, L305 and Q309 while the lower two panels are K315, F317 and A318. These residues are colored red in α_M I-domain structure (pdb: 1jlm).

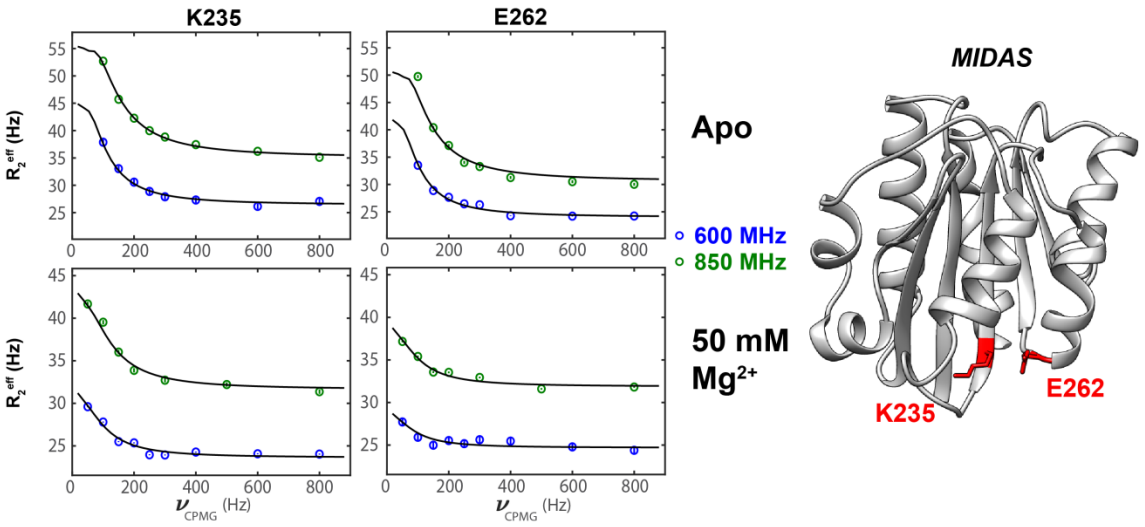

Figure 5.6 Relaxation Dispersion Profiles of Residues in the Bottom Surface of α_M I-domain.
K235 and E262 were group-fitted for apo (upper) and Mg^{2+} (lower) samples. The two residues are colored red in α_M I-domain structure (pdb: 1jlm).

5.5 Discussion

Integrin has been extensively studied in structural biology as large scale structural rearrangement is involved upon integrin activation (16). Studies using X-ray crystallography, electron microscopy (EM) and super-resolution microscopy revealed conformational changes in integrin (25,39-44). As the ligand binding site, α I-domains also undergo conformational changes that relay ligand binding signals to the rest of integrin molecules (16). Current work focuses on α_M I-domain of Mac-1, one of the most promiscuous members of the integrin family. MIDAS, as the ligand binding site in α_M I-domain, was found to expose different sets of residues for different ligands (27). In order to selectively present residues, MIDAS needs to be highly dynamic to adopt multiple local conformations. So far the only NMR CPMG relaxation dispersion analysis on α I-domains is on α_1 I-domain. In that study, Mg^{2+} was found to induce μs-ms motions on

MIDAS residues and residues close to a salt bridge distal to MIDAS. It turns out that these dynamics are functional as mutations of the exchanged residues affect collagen bindings of α_1 I-domain (29). This study serves as a model to explore and compare the conformational dynamics of α_M I domain with α_1 I-domain.

Table 5.1 GUARDD Group Fits of ^{15}N CPMG Relaxation Dispersion Curves Recorded at 600 and 850 MHz for Apo and Mg^{2+} Bound Samples of Integrin α_M I-domain.

MIDAS residues are labeled with asterisks (*); α7 helix residues are labeled with daggers (†); Residues in the N/C bottom surface are labeled with double-daggers (‡).

	k_{ex} (s^{-1})	p_A(%)	Residue (^{15}N)	R_{ex} (s^{-1}) 600 MHz	R_{ex} (s^{-1}) 850 MHz	Δω N (ppm)
Apo	702.6 ± 169.5	94.0 ± 5.5	D140*	25.2 ± 5.2	40.8 ± 7.0	1.9 ± 0.5
			Q204*	16.9 ± 1.8	28.4 ± 1.6	1.5 ± 0.3
			E244*	14.5 ± 1.4	22.2 ± 1.6	1.6 ± 0.3
	1627.3 ± 702.4	98.5 ± 17.3	G272*	5.9 ± 0.9	11.7 ± 0.8	2.6 ± 1.4
	276.3 ± 196.7	96.5 ± 17.0	F317†	3.5 ± 0.6	5.0 ± 0.4	1.1 ± 0.8
			A318†	3.6 ± 0.3	7.7 ± 0.2	1.0 ± 0.9
	267.3 ± 122.0	91.7 ± 9.4	K235‡	18.1 ± 1.8	25.3 ± 1.5	1.7 ± 0.5
			E262‡	19.2 ± 1.6	30.9 ± 1.3	1.6 ± 0.3
Mg^{2+}	1163.2 ± 307.9	96.7 ± 9.7	D140*	12.2 ± 4.2	15.6 ± 5.8	2.7 ± 0.9
			Q204*	3.4 ± 0.8	8.0 ± 1.0	1.4 ± 0.6
bound			E244*	3.6 ± 0.7	4.5 ± 0.9	1.1 ± 0.3
	2162.7± 1416.0	78.7 ± 18.8	G272*	4.7 ± 1.0	8.2 ± 1.3	0.8 ± 1.5
	1499.3 ± 166.2	70.0 ± 19.1	F302†	8.5 ± 0.9	10.6 ± 0.9	0.6 ± 0.4
			E303†	5.4 ± 1.4	7.5 ± 1.9	0.6 ± 0.4
			L305†	4.9 ± 0.7	5.7 ± 0.9	0.4 ± 0.2
			Q309†	4.1 ± 0.5	6.6 ± 0.6	0.5 ± 0.3
	982.7 ± 194.6	98.2 ± 0.5	K315†	2.8 ± 0.3	4.7 ± 0.4	1.6 ± 0.2
			K317†	4.8 ± 0.5	6.5 ± 0.7	1.8 ± 0.2
			A318†	4.6 ± 0.4	7.1 ± 0.5	2.1 ± 0.3
	485.2 ± 112.4	95.8 ± 7.2	K235‡	5.6 ± 1.0	8.2 ± 1.0	1.1 ± 0.2
			E262‡	2.7 ± 0.8	4.3 ± 0.6	0.7 ± 0.1

Our CPMG analysis of α_M I-domain reveals μs-ms dynamics of MIDAS residues in both apo and Mg^{2+} containing samples. This means that the μs-ms motions are inherent in α_M I MIDAS, which is different from α_1 I MIDAS, which only exhibit slow time scale motion after Mg^{2+} binding (29). Just like α_1 I dynamics is consistent with the

Mg^{2+}-dependent mechanism of α I-ligand interactions (16), the intrinsic dynamic nature of α_M I-domain may be crucial to the ligand promiscuity of the domain. However, there may be multiple ligand interaction mechanisms for the promiscuous Mac-1. For example, as discussed in Chapter 4, α_M I-domain interacts with cationic ligands in a newly discovered Mg^{2+} independent mechanism. The novel findings imply that motions, existing in MIDAS regardless of Mg^{2+}, are possibly functional for α_M I-domain's ligand interactions. To summarize, current results confirm that μs-ms conformational dynamics in α_M I MIDAS are intrinsic and present even without Mg^{2+}.

Although α7 helix motions were not discovered in α_1 I (29), they are significant in α_M I-domain. In Figure 5.4, other than F317 and A318, most residues in the C-terminal helix do not have relaxation dispersion in apo samples. F317 and A318 indeed display slow exchange rates (k_{ex} ~ 240 s^{-1}). Immediately preceding them is I316, which does not exhibit any relaxation dispersion effect. This is consistent with the fact that the residue is wedged in a hydrophobic pocket in the inactive conformation (22). In contrast, Mg^{2+} induces fast (> ~1000 s^{-1}) motions for an expanded list of residues in α7 helix. Movement of the C-terminal helix is considered a crucial event that links the α I-domain conformational changes with global structural rearrangements in integrin molecules (16). The movement, ascertained by crystal structures, activates α I-domains (18,19). Current data supports the C-terminal helix mobility as Mg^{2+} induced fast dynamics spreads out along the helix. Studies have also indicated that divalent metal ions such as Mg^{2+} activate integrin and enhance α I-ligand interactions (16,45,46). It is likely that Mg^{2+} induced fast dynamics on the α7 helix is essential to ligand bindings and activation of the entire

protein that follows. More dynamics and functional studies can be done to investigate the C-terminal helix motions.

In the bottom of α_M I-domain, slow motions (K235 and E262) were discovered, which are not found in α_1 I-domain (29). When Mg^{2+} is present, k_{ex} for these two residues is almost 2-fold higher than in the apo state. The bottom surface is on the opposite side from the ligand binding MIDAS. α_M I-domain is covalently attached to β propellers through N and C linkers in the bottom (16). It is also the interface of α and β subunits (16). Studies using activation-specific antibodies manifested that mutations in the bottom surface activate Mac-1 and increase ligand affinities (21). These activating mutations are actually very close to F235 and E262. It is possible that motions in the bottom region are crucial for activation. However, it is not clear how the bottom surface motions exactly contribute to activation and what regulatory roles the Mg^{2+} induced motions play. Further work is needed to confirm the functionality of the bottom dynamics. It should be noted that homodimeric interactions between MIDAS and N/C termini region (bottom) may exist, although much weaker in the current N/C truncated version, which is discussed in Chapter 3. It is not known if the bottom dynamics is a result of the weak homodimeric interactions.

Data fittings from GUARDD program reveal that k_{ex} values are systematically higher in the presence of Mg^{2+}, meaning Mg^{2+} bindings produce faster motions in α_M I-domain. This is consistent with R_{ex} values obtained for the apo and Mg^{2+} bound states. As displayed in Figure 5.3, most residues have larger R_{ex} values in the apo state with the only exception being residues in α7 helix, whose R_{ex} values are consistently smaller in

the apo state. Apparently, motions of most residues are in the μs-ms range in the apo state and become faster upon Mg^{2+} addition. However, with no Mg^{2+}, α7 helix is likely to be rigid, therefore has low R_{ex} values. Mg^{2+} induced more motion in the helix, bringing k_{ex} to the μs-ms range, which leads to relaxation dispersions and larger R_{ex} in α7 helix. To conclude, the R_{ex} plots suggest: 1, slow motions are intrinsic in α_M I-domain; 2, Mg^{2+} binding produce overall faster dynamics, including μs-ms motions in α7 helix. All these are consistent with the exchange parameters from fitting analysis (Table 5.1).

Due to the large scale conformational rearrangements, integrins and α I-domains are excellent models of protein dynamics studies (16). However, much is unknown about how protein motions are related with ligand bindings and global structural changes during integrin activation. Present investigations on α_M I-domain provide preliminary analysis of μs-ms dynamics using CPMG experiments. We unraveled motions unique for α_M I-domains, which are intrinsic dynamics in the MIDAS and the bottom surface, and Mg^{2+} induced dynamics in α7 helix. As to how these dynamics processes actually contribute to functions of α_M I-domains and Mac-1, more work is needed. This may involve mutating residues in MIDAS to modulate dynamics and monitor their effects on ligand affinity and/or ligand selectivity. Exchanged residues in α7 helix can be mutated in mammalian cells to probe whether cell adhesions and migrations are changed. In our studies, ps-ns range dynamics of α_M I-domain are missing as CPMG is tailored to probe slower μs-ms range dynamics only. In order to fill the gap, model-free S^2 analysis should be performed to explore the effects of Mg^{2+} on motions of such timescales (7,8).

CHAPTER 6

SUMMARY AND OUTLOOK

Work in the thesis aims to investigate interactions of glycosaminoglycan (GAG) binding proteins with their proteoglycan and non-proteoglycan receptors from a structural biology perspective. GAG-binding proteins (GBPs) encompass a variety of proteins with different biological functions, such as chemokines, growth factors and extracellular matrix (ECM) proteins (1). Such diverse families of proteins interact with various partners, including GAGs as well as other proteins. Chapter 2 explores GAG interactions of decorin binding protein B (DBPB). Chapters 3-5 discuss integrin α_M I-domain as a receptor for positively charged pleotrophin (PTN) and platelet factor 4 (PF4), which are GBPs.

6.1 Decorin Binding Protein B (DBPB) Interactions with GAGs.

The first structure of B31 DBPB structure was determined with NMR. Using biochemical and biophysical methods, lysine-rich C terminus was identified as the GAG-binding epitope. However, soluble mature form of DBPB was used here without the N-terminal triacyl-modified cysteine (2). The lipidation sequence anchors DBPs onto the spirochaete outer membrane. Lipidated form of DBPB may have different structures and/or oligomerization status from soluble unlipidated form. Although lipidation effects on DBPB are poorly understood, one study showed that the lipidated version of DBPA has considerably higher affinity for decorins than the unlipidated verion (3). Future work should be focused on the effects of lipidation on DBPB-GAG interactions. Current work indicated similar GAG affinities of DBPA and DBPB. However, DBPA is less conserved

in sequence than DBPB (4-6). Despite contributing similarly to infectivity, DBPA and DBPB have different effects on bacterial dissemination and tissue colonization (7). Further investigations using lipidated proteins may lead to deeper understandings of what contributes to the difference in virulence and overall infection.

6.2 Pleiotrophin and Platelet Factor 4 Interactions with Integrin α_M I-domain.

Pleiotrophin (PTN), a cytokine, and platelet factor 4 (PF4), a chemokine, are both highly positively charged proteins that bind GAGs strongly (8) (9). Current investigations revealed that the two cationic proteins interact with integrin α_M I-domain in a novel Mg^{2+}-independent mechanism. In particular, PTN and PF4 both bind to the metal ion dependent adhesion site (MIDAS) in α_M I-domain, a site commonly used to bind ligands in a metal-mediated fashion. However, binding of these cationic ligands at MIDAS does not require Mg^{2+} at all. In addition, PF4 interaction does not induce conformational change in α_M I-domain. It would be insightful to probe if intact integrin Mac-1 changes conformations upon PF4 or PTN binding. Atomic level structures of α_M I-PTN/PF4 complex would also provide more details of the interactions.

6.3 Integrin α_M I-domain Conformational Dynamics.

Integrins are known to have multiple conformations. Many of these significant conformational changes take place in the α I-domains (10-17). Using NMR relaxation dispersion experiments, intrinsic μs-ms motions in MIDAS residues were observed. In addition, Mg^{2+} induced increases in the kinetics of the motion in residues throughout the protein, but especially in α_M I MIDAS and α7 helix respectively. This is different from the observations on α_1 I-domain in which only Mg^{2+} induced μs-ms motions in MIDAS

were detected (18). It is not clear if the unique dynamics of α_M I-domain is functionally relevant. More work needs to be done to examine changes in ligand affinity in mutants lacking the dynamics. Studies also suggested that mutations in the bottom surface of α_M I-domain promote active conformations and ligand interactions (19). Whether the bottom mutations activate α_M I-domain by stimulating any dynamic processes is unknown. NMR relaxation dispersion experiments could be performed to investigate the effects of the bottom mutations on conformational dynamics of α_M I-domain. As α7 helix movement is a key event that connects conformational change of α I-domain to the global structural rearrangement of integrin proteins (17), it will be of great interest to probe the effects of the mutations on the conformational flexibility of intact integrins on cell surface. In particular, these mutations may change the potential energy required to convert the integrin from the bend to the extended conformation. Recent advances in super-resolution microscopy make it possible to perform optical measurements of conformational changes on such a large scale in integrins (20).

REFERENCES

Chapter 1 References

1. Kamhi, E., Joo, E. J., Dordick, J. S., and Linhardt, R. J. (2013) Glycosaminoglycans in infectious disease. *Biological reviews of the Cambridge Philosophical Society* **88**, 928-943

2. Linhardt, R. J., and Toida, T. (2004) Role of glycosaminoglycans in cellular communication. *Accounts of chemical research* **37**, 431-438

3. Kumar, V., Hassan, M. I., Tomar, A. K., Kashav, T., Nautiyal, J., Singh, S., Singh, T. P., and Yadav, S. (2009) Proteomic analysis of heparin-binding proteins from human seminal plasma: a step towards identification of molecular markers of male fertility. *Journal of biosciences* **34**, 899-908

4. Ori, A., Wilkinson, M. C., and Fernig, D. G. (2011) A systems biology approach for the investigation of the heparin/heparan sulfate interactome. *The Journal of biological chemistry* **286**, 19892-19904

5. Kjellen, L., and Lindahl, U. (1991) Proteoglycans: structures and interactions. *Annual review of biochemistry* **60**, 443-475

6. Lindahl, U., Lidholt, K., Spillmann, D., and Kjellen, L. (1994) More to "heparin" than anticoagulation. *Thrombosis research* **75**, 1-32

7. Capila, I., and Linhardt, R. J. (2002) Heparin-protein interactions. *Angewandte Chemie* **41**, 391-412

8. Smith, R. A., Meade, K., Pickford, C. E., Holley, R. J., and Merry, C. L. (2011) Glycosaminoglycans as regulators of stem cell differentiation. *Biochemical Society transactions* **39**, 383-387

9. Hacker, U., Nybakken, K., and Perrimon, N. (2005) Heparan sulphate proteoglycans: the sweet side of development. *Nature reviews. Molecular cell biology* **6**, 530-541

10. Li, J. P., and Vlodavsky, I. (2009) Heparin, heparan sulfate and heparanase in inflammatory reactions. *Thrombosis and haemostasis* **102**, 823-828

11. Parish, C. R. (2006) The role of heparan sulphate in inflammation. *Nature reviews. Immunology* **6**, 633-643

12. Taylor, K. R., and Gallo, R. L. (2006) Glycosaminoglycans and their proteoglycans: host-associated molecular patterns for initiation and modulation of

inflammation. *FASEB journal : official publication of the Federation of American Societies for Experimental Biology* **20**, 9-22

13. Afratis, N., Gialeli, C., Nikitovic, D., Tsegenidis, T., Karousou, E., Theocharis, A. D., Pavao, M. S., Tzanakakis, G. N., and Karamanos, N. K. (2012) Glycosaminoglycans: key players in cancer cell biology and treatment. *The FEBS journal* **279**, 1177-1197

14. Fuster, M. M., and Esko, J. D. (2005) The sweet and sour of cancer: glycans as novel therapeutic targets. *Nature reviews. Cancer* **5**, 526-542

15. Yip, G. W., Smollich, M., and Gotte, M. (2006) Therapeutic value of glycosaminoglycans in cancer. *Molecular cancer therapeutics* **5**, 2139-2148

16. Kisilevsky, R., Ancsin, J. B., Szarek, W. A., and Petanceska, S. (2007) Heparan sulfate as a therapeutic target in amyloidogenesis: prospects and possible complications. *Amyloid : the international journal of experimental and clinical investigation : the official journal of the International Society of Amyloidosis* **14**, 21-32

17. Papy-Garcia, D., Christophe, M., Huynh, M. B., Fernando, S., Ludmilla, S., Sepulveda-Diaz, J. E., and Raisman-Vozari, R. (2011) Glycosaminoglycans, protein aggregation and neurodegeneration. *Current protein & peptide science* **12**, 258-268

18. Aquino, R. S., Lee, E. S., and Park, P. W. (2010) Diverse functions of glycosaminoglycans in infectious diseases. *Progress in molecular biology and translational science* **93**, 373-394

19. Dinglasan, R. R., and Jacobs-Lorena, M. (2005) Insight into a conserved lifestyle: protein-carbohydrate adhesion strategies of vector-borne pathogens. *Infection and immunity* **73**, 7797-7807

20. Zhang, L. (2010) Glycosaminoglycan (GAG) biosynthesis and GAG-binding proteins. *Progress in molecular biology and translational science* **93**, 1-17

21. Esko, J. D., J, H. P., and Linhardt, R. J. (2015) Proteins That Bind Sulfated Glycosaminoglycans. in *Essentials of Glycobiology* (rd, Varki, A., Cummings, R. D., Esko, J. D., Stanley, P., Hart, G. W., Aebi, M., Darvill, A. G., Kinoshita, T., Packer, N. H., Prestegard, J. H., Schnaar, R. L., and Seeberger, P. H. eds.), Cold Spring Harbor (NY). pp 493-502

22. Cardin, A. D., and Weintraub, H. J. (1989) Molecular modeling of protein-glycosaminoglycan interactions. *Arteriosclerosis* **9**, 21-32

23. Sobel, M., Soler, D. F., Kermode, J. C., and Harris, R. B. (1992) Localization and characterization of a heparin binding domain peptide of human von Willebrand factor. *The Journal of biological chemistry* **267**, 8857-8862

24. Margalit, H., Fischer, N., and Ben-Sasson, S. A. (1993) Comparative analysis of structurally defined heparin binding sequences reveals a distinct spatial distribution of basic residues. *The Journal of biological chemistry* **268**, 19228-19231

25. Fromm, J. R., Hileman, R. E., Caldwell, E. E., Weiler, J. M., and Linhardt, R. J. (1995) Differences in the interaction of heparin with arginine and lysine and the importance of these basic amino acids in the binding of heparin to acidic fibroblast growth factor. *Archives of biochemistry and biophysics* **323**, 279-287

26. Fromm, J. R., Hileman, R. E., Caldwell, E. E., Weiler, J. M., and Linhardt, R. J. (1997) Pattern and spacing of basic amino acids in heparin binding sites. *Archives of biochemistry and biophysics* **343**, 92-100

27. Rostand, K. S., and Esko, J. D. (1997) Microbial adherence to and invasion through proteoglycans. *Infection and immunity* **65**, 1-8

28. Chen, T., Belland, R. J., Wilson, J., and Swanson, J. (1995) Adherence of pilus- Opa+ gonococci to epithelial cells in vitro involves heparan sulfate. *The Journal of experimental medicine* **182**, 511-517

29. Fagan, R. P., Lambert, M. A., and Smith, S. G. (2008) The hek outer membrane protein of Escherichia coli strain RS218 binds to proteoglycan and utilizes a single extracellular loop for adherence, invasion, and autoaggregation. *Infection and immunity* **76**, 1135-1142

30. Baron, M. J., Bolduc, G. R., Goldberg, M. B., Auperin, T. C., and Madoff, L. C. (2004) Alpha C protein of group B Streptococcus binds host cell surface glycosaminoglycan and enters cells by an actin-dependent mechanism. *The Journal of biological chemistry* **279**, 24714-24723

31. Baron, M. J., Wong, S. L., Nybakken, K., Carey, V. J., and Madoff, L. C. (2009) Host glycosaminoglycan confers susceptibility to bacterial infection in Drosophila melanogaster. *Infection and immunity* **77**, 860-866

32. Schmidtchen, A., Holst, E., Tapper, H., and Bjorck, L. (2003) Elastase-producing Pseudomonas aeruginosa degrade plasma proteins and extracellular products of human skin and fibroblasts, and inhibit fibroblast growth. *Microbial pathogenesis* **34**, 47-55

33. Radolf, J. D., Caimano, M. J., Stevenson, B., and Hu, L. T. (2012) Of ticks, mice and men: understanding the dual-host lifestyle of Lyme disease spirochaetes. *Nature reviews. Microbiology* **10**, 87-99

34. Feder, H. M., Jr., Johnson, B. J., O'Connell, S., Shapiro, E. D., Steere, A. C., Wormser, G. P., Ad Hoc International Lyme Disease, G., Agger, W. A., Artsob, H., Auwaerter, P., Dumler, J. S., Bakken, J. S., Bockenstedt, L. K., Green, J., Dattwyler, R. J., Munoz, J., Nadelman, R. B., Schwartz, I., Draper, T., McSweegan, E., Halperin, J. J., Klempner, M. S., Krause, P. J., Mead, P., Morshed, M., Porwancher, R., Radolf, J. D., Smith, R. P., Jr., Sood, S., Weinstein, A., Wong, S. J., and Zemel, L. (2007) A critical appraisal of "chronic Lyme disease". *The New England journal of medicine* **357**, 1422-1430

35. Steere, A. C., and Glickstein, L. (2004) Elucidation of Lyme arthritis. *Nature reviews. Immunology* **4**, 143-152

36. Guo, B. P., Brown, E. L., Dorward, D. W., Rosenberg, L. C., and Hook, M. (1998) Decorin-binding adhesins from Borrelia burgdorferi. *Molecular microbiology* **30**, 711-723

37. Guo, B. P., Norris, S. J., Rosenberg, L. C., and Hook, M. (1995) Adherence of Borrelia burgdorferi to the proteoglycan decorin. *Infection and immunity* **63**, 3467-3472

38. Fischer, J. R., Parveen, N., Magoun, L., and Leong, J. M. (2003) Decorin-binding proteins A and B confer distinct mammalian cell type-specific attachment by Borrelia burgdorferi, the Lyme disease spirochete. *Proceedings of the National Academy of Sciences of the United States of America* **100**, 7307-7312

39. Leong, J. M., Robbins, D., Rosenfeld, L., Lahiri, B., and Parveen, N. (1998) Structural requirements for glycosaminoglycan recognition by the Lyme disease spirochete, Borrelia burgdorferi. *Infection and immunity* **66**, 6045-6048

40. Wang, X. (2012) Solution structure of decorin-binding protein A from Borrelia burgdorferi. *Biochemistry* **51**, 8353-8362

41. Benoit, V. M., Fischer, J. R., Lin, Y. P., Parveen, N., and Leong, J. M. (2011) Allelic variation of the Lyme disease spirochete adhesin DbpA influences spirochetal binding to decorin, dermatan sulfate, and mammalian cells. *Infection and immunity* **79**, 3501-3509

42. Roberts, W. C., Mullikin, B. A., Lathigra, R., and Hanson, M. S. (1998) Molecular analysis of sequence heterogeneity among genes encoding decorin binding proteins A and B of Borrelia burgdorferi sensu lato. *Infection and immunity* **66**, 5275-5285

43. Shi, Y., Xu, Q., Seemanaplli, S. V., McShan, K., and Liang, F. T. (2008) Common and unique contributions of decorin-binding proteins A and B to the overall virulence of Borrelia burgdorferi. *PloS one* **3**, e3340

44. Fortune, D. E., Lin, Y. P., Deka, R. K., Groshong, A. M., Moore, B. P., Hagman, K. E., Leong, J. M., Tomchick, D. R., and Blevins, J. S. (2014) Identification of Lysine Residues in the Borrelia burgdorferi DbpA Adhesin Required for Murine Infection. *Infection and immunity* **82**, 3186-3198

45. Hynes, R. O. (2009) The extracellular matrix: not just pretty fibrils. *Science* **326**, 1216-1219

46. Bonnans, C., Chou, J., and Werb, Z. (2014) Remodelling the extracellular matrix in development and disease. *Nature reviews. Molecular cell biology* **15**, 786-801

47. Luo, B. H., Carman, C. V., and Springer, T. A. (2007) Structural basis of integrin regulation and signaling. *Annual review of immunology* **25**, 619-647

48. Johnson, M. S., Lu, N., Denessiouk, K., Heino, J., and Gullberg, D. (2009) Integrins during evolution: Evolutionary trees and model organisms. *Bba-Biomembranes* **1788**, 779-789

49. Tamkun, J. W., DeSimone, D. W., Fonda, D., Patel, R. S., Buck, C., Horwitz, A. F., and Hynes, R. O. (1986) Structure of integrin, a glycoprotein involved in the transmembrane linkage between fibronectin and actin. *Cell* **46**, 271-282

50. Larson, R. S., Corbi, A. L., Berman, L., and Springer, T. (1989) Primary structure of the leukocyte function-associated molecule-1 alpha subunit: an integrin with an embedded domain defining a protein superfamily. *The Journal of cell biology* **108**, 703-712

51. Xiong, J. P., Stehle, T., Diefenbach, B., Zhang, R., Dunker, R., Scott, D. L., Joachimiak, A., Goodman, S. L., and Arnaout, M. A. (2001) Crystal structure of the extracellular segment of integrin alpha Vbeta3. *Science* **294**, 339-345

52. Zhu, J., Luo, B. H., Xiao, T., Zhang, C., Nishida, N., and Springer, T. A. (2008) Structure of a complete integrin ectodomain in a physiologic resting state and activation and deactivation by applied forces. *Molecular cell* **32**, 849-861

53. Xie, C., Zhu, J., Chen, X., Mi, L., Nishida, N., and Springer, T. A. (2010) Structure of an integrin with an alphaI domain, complement receptor type 4. *The EMBO journal* **29**, 666-679

54. Shi, M., Foo, S. Y., Tan, S. M., Mitchell, E. P., Law, S. K., and Lescar, J. (2007) A structural hypothesis for the transition between bent and extended

conformations of the leukocyte beta2 integrins. *The Journal of biological chemistry* **282**, 30198-30206

55. Nermut, M. V., Green, N. M., Eason, P., Yamada, S. S., and Yamada, K. M. (1988) Electron microscopy and structural model of human fibronectin receptor. *The EMBO journal* **7**, 4093-4099

56. Carrell, N. A., Fitzgerald, L. A., Steiner, B., Erickson, H. P., and Phillips, D. R. (1985) Structure of human platelet membrane glycoproteins IIb and IIIa as determined by electron microscopy. *The Journal of biological chemistry* **260**, 1743-1749

57. Du, X., Gu, M., Weisel, J. W., Nagaswami, C., Bennett, J. S., Bowditch, R., and Ginsberg, M. H. (1993) Long range propagation of conformational changes in integrin alpha IIb beta 3. *The Journal of biological chemistry* **268**, 23087-23092

58. Erb, E. M., Tangemann, K., Bohrmann, B., Muller, B., and Engel, J. (1997) Integrin alphaIIb beta3 reconstituted into lipid bilayers is nonclustered in its activated state but clusters after fibrinogen binding. *Biochemistry* **36**, 7395-7402

59. Hantgan, R. R., Paumi, C., Rocco, M., and Weisel, J. W. (1999) Effects of ligand-mimetic peptides Arg-Gly-Asp-X (X = Phe, Trp, Ser) on alphaIIbbeta3 integrin conformation and oligomerization. *Biochemistry* **38**, 14461-14474

60. Kelly, T., Molony, L., and Burridge, K. (1987) Purification of two smooth muscle glycoproteins related to integrin. Distribution in cultured chicken embryo fibroblasts. *The Journal of biological chemistry* **262**, 17189-17199

61. Parise, L. V., and Phillips, D. R. (1985) Platelet membrane glycoprotein IIb-IIIa complex incorporated into phospholipid vesicles. Preparation and morphology. *The Journal of biological chemistry* **260**, 1750-1756

62. Weisel, J. W., Nagaswami, C., Vilaire, G., and Bennett, J. S. (1992) Examination of the platelet membrane glycoprotein IIb-IIIa complex and its interaction with fibrinogen and other ligands by electron microscopy. *The Journal of biological chemistry* **267**, 16637-16643

63. Humphries, M. J. (2004) Monoclonal antibodies as probes of integrin priming and activation. *Biochemical Society transactions* **32**, 407-411

64. Nishida, N., Xie, C., Shimaoka, M., Cheng, Y., Walz, T., and Springer, T. A. (2006) Activation of leukocyte beta2 integrins by conversion from bent to extended conformations. *Immunity* **25**, 583-594

65. Shtengel, G., Galbraith, J. A., Galbraith, C. G., Lippincott-Schwartz, J., Gillette, J. M., Manley, S., Sougrat, R., Waterman, C. M., Kanchanawong, P., Davidson, M.

W., Fetter, R. D., and Hess, H. F. (2009) Interferometric fluorescent super-resolution microscopy resolves 3D cellular ultrastructure. *Proceedings of the National Academy of Sciences of the United States of America* **106**, 3125-3130

66. Moore, T. I., Aaron, J., Chew, T. L., and Springer, T. A. (2018) Measuring Integrin Conformational Change on the Cell Surface with Super-Resolution Microscopy. *Cell reports* **22**, 1903-1912

67. Campbell, I. D., and Humphries, M. J. (2011) Integrin structure, activation, and interactions. *Cold Spring Harbor perspectives in biology* **3**

68. Podolnikova, N. P., Podolnikov, A. V., Haas, T. A., Lishko, V. K., and Ugarova, T. P. (2015) Ligand recognition specificity of leukocyte integrin alphaMbeta2 (Mac-1, CD11b/CD18) and its functional consequences. *Biochemistry* **54**, 1408-1420

69. Ryan, E., Shen, D., and Wang, X. (2016) Structural studies reveal an important role for the pleiotrophin C-terminus in mediating interactions with chondroitin sulfate. *The FEBS journal* **283**, 1488-1503

70. Loscalzo, J., Melnick, B., and Handin, R. I. (1985) The interaction of platelet factor four and glycosaminoglycans. *Archives of biochemistry and biophysics* **240**, 446-455

71. Shen, D., Podolnikova, N. P., Yakubenko, V. P., Ardell, C. L., Balabiyev, A., Ugarova, T. P., and Wang, X. (2017) Pleiotrophin, a multifunctional cytokine and growth factor, induces leukocyte responses through the integrin Mac-1. *The Journal of biological chemistry* **292**, 18848-18861

72. Lishko, V. K., Yakubenko, V. P., Ugarova, T. P., and Podolnikova, N. P. (2018) Leukocyte integrin Mac-1 (CD11b/CD18, alphaMbeta2, CR3) acts as a functional receptor for platelet factor 4. *The Journal of biological chemistry* **293**, 6869-6882

Chapter 2 References

1. Brissette, C. A., and Gaultney, R. A. (2014) That's my story, and I'm sticking to it--an update on B. burgdorferi adhesins. *Front Cell Infect Microbiol* **4**, 41

2. Coburn, J., Leong, J., and Chaconas, G. (2013) Illuminating the roles of the Borrelia burgdorferi adhesins. *Trends Microbiol* **21**, 372-379

3. Guo, B. P., Brown, E. L., Dorward, D. W., Rosenberg, L. C., and Hook, M. (1998) Decorin-binding adhesins from Borrelia burgdorferi. *Molecular microbiology* **30**, 711-723

4. Shi, Y., Xu, Q., McShan, K., and Liang, F. T. (2008) Both decorin-binding proteins A and B are critical for the overall virulence of Borrelia burgdorferi. *Infection and immunity* **76**, 1239-1246

5. Weening, E. H., Parveen, N., Trzeciakowski, J. P., Leong, J. M., Hoeoek, M., and Skare, J. T. (2008) Borrelia burgdorferi Lacking DbpBA Exhibits an Early Survival Defect during Experimental Infection. *Infection and immunity* **76**, 5694-5705

6. Imai, D. M., Samuels, D. S., Feng, S., Hodzic, E., Olsen, K., and Barthold, S. W. (2013) The early dissemination defect attributed to disruption of decorin-binding proteins is abolished in chronic murine lyme borreliosis. *Infect Immun* **81**, 1663-1673

7. Salo, J., Jaatinen, A., Soderstrom, M., Viljanen, M. K., and Hytonen, J. (2015) Decorin binding proteins of Borrelia burgdorferi promote arthritis development and joint specific post-treatment DNA persistence in mice. *PloS one* **10**, e0121512

8. Shi, Y., Xu, Q., Seemanaplli, S. V., McShan, K., and Liang, F. T. (2008) Common and unique contributions of decorin-binding proteins A and B to the overall virulence of Borrelia burgdorferi. *PloS one* **3**, e3340

9. Fischer, J. R., Parveen, N., Magoun, L., and Leong, J. M. (2003) Decorin-binding proteins A and B confer distinct mammalian cell type-specific attachment by Borrelia burgdorferi, the Lyme disease spirochete. *Proceedings of the National Academy of Sciences of the United States of America* **100**, 7307-7312

10. Wang, X. (2012) Solution structure of decorin-binding protein A from Borrelia burgdorferi. *Biochemistry* **51**, 8353-8362

11. Roberts, W. C., Mullikin, B. A., Lathigra, R., and Hanson, M. S. (1998) Molecular analysis of sequence heterogeneity among genes encoding decorin binding proteins A and B of Borrelia burgdorferi sensu lato. *Infection and immunity* **66**, 5275-5285

12. Guo, B. P., Norris, S. J., Rosenberg, L. C., and Hook, M. (1995) Adherence of Borrelia burgdorferi to the proteoglycan decorin. *Infection and immunity* **63**, 3467-3472

13. Benoit, V. M., Fischer, J. R., Lin, Y. P., Parveen, N., and Leong, J. M. (2011) Allelic variation of the Lyme disease spirochete adhesin DbpA influences spirochetal binding to decorin, dermatan sulfate, and mammalian cells. *Infection and immunity* **79**, 3501-3509

14. Leong, J. M., Robbins, D., Rosenfeld, L., Lahiri, B., and Parveen, N. (1998) Structural requirements for glycosaminoglycan recognition by the Lyme disease spirochete, Borrelia burgdorferi. *Infection and immunity* **66**, 6045-6048

15. Parveen, N., Robbins, D., and Leong, J. M. (1999) Strain variation in glycosaminoglycan recognition influences cell-type-specific binding by lyme disease spirochetes. *Infect Immun* **67**, 1743-1749

16. Varki, A. (2009) *Essentials of glycobiology*, 2nd ed., Cold Spring Harbor Laboratory Press, Cold Spring Harbor, N.Y.

17. Leong, J. M., Wang, H., Magoun, L., Field, J. A., Morrissey, P. E., Robbins, D., Tatro, J. B., Coburn, J., and Parveen, N. (1998) Different classes of proteoglycans contribute to the attachment of Borrelia burgdorferi to cultured endothelial and brain cells. *Infection and immunity* **66**, 994-999

18. Fortune, D. E., Lin, Y. P., Deka, R. K., Groshong, A. M., Moore, B. P., Hagman, K. E., Leong, J. M., Tomchick, D. R., and Blevins, J. S. (2014) Identification of Lysine Residues in the Borrelia burgdorferi DbpA Adhesin Required for Murine Infection. *Infection and immunity*

19. Morgan, A., and Wang, X. (2013) The novel heparin-binding motif in decorin-binding protein A from strain B31 of Borrelia burgdorferi explains the higher binding affinity. *Biochemistry* **52**, 8237-8245

20. Barbour, A. G., Jasinskas, A., Kayala, M. A., Davies, D. H., Steere, A. C., Baldi, P., and Felgner, P. L. (2008) A genome-wide proteome array reveals a limited set of immunogens in natural infections of humans and white-footed mice with Borrelia burgdorferi. *Infect Immun* **76**, 3374-3389

21. Catanzariti, A. M., Soboleva, T. A., Jans, D. A., Board, P. G., and Baker, R. T. (2004) An efficient system for high-level expression and easy purification of authentic recombinant proteins. *Protein science : a publication of the Protein Society* **13**, 1331-1339

22. Xiao, Z., Zhao, W., Yang, B., Zhang, Z., Guan, H., and Linhardt, R. J. (2011) Heparinase 1 selectivity for the 3,6-di-O-sulfo-2-deoxy-2-sulfamido-alpha-D-glucopyranose (1,4) 2-O-sulfo-alpha-L-idopyranosyluronic acid (GlcNS3S6S-IdoA2S) linkages. *Glycobiology* **21**, 13-22

23. Yang, H. O., Gunay, N. S., Toida, T., Kuberan, B., Yu, G., Kim, Y. S., and Linhardt, R. J. (2000) Preparation and structural determination of dermatan sulfate-derived oligosaccharides. *Glycobiology* **10**, 1033-1039

24. Wurtz, P., Hellman, M., Tossavainen, H., and Permi, P. (2006) Towards unambiguous assignment of methyl-containing residues by double and triple sensitivity-enhanced HCCmHm-TOCSY experiments. *J Biomol Nmr* **36**, 13-26

25. Liu, Y., and Prestegard, J. H. (2009) Measurement of one and two bond N-C couplings in large proteins by TROSY-based J-modulation experiments. *J Magn Reson* **200**, 109-118

26. Delaglio, F., Grzesiek, S., Vuister, G. W., Zhu, G., Pfeifer, J., and Bax, A. (1995) NMRPipe: a multidimensional spectral processing system based on UNIX pipes. *Journal of biomolecular NMR* **6**, 277-293

27. Johnson, B. A. (2004) Using NMRView to visualize and analyze the NMR spectra of macromolecules. *Methods Mol Biol* **278**, 313-352

28. Iwahara, J., Tang, C., and Marius Clore, G. (2007) Practical aspects of (1)H transverse paramagnetic relaxation enhancement measurements on macromolecules. *J Magn Reson* **184**, 185-195

29. d'Auvergne, E. J., and Gooley, P. R. (2008) Optimisation of NMR dynamic models I. Minimisation algorithms and their performance within the model-free and Brownian rotational diffusion spaces. *Journal of biomolecular NMR* **40**, 107-119

30. Kay, L. E., Torchia, D. A., and Bax, A. (1989) Backbone dynamics of proteins as studied by 15N inverse detected heteronuclear NMR spectroscopy: application to staphylococcal nuclease. *Biochemistry* **28**, 8972-8979

31. Tollinger, M., Skrynnikov, N. R., Mulder, F. A., Forman-Kay, J. D., and Kay, L. E. (2001) Slow dynamics in folded and unfolded states of an SH3 domain. *J Am Chem Soc* **123**, 11341-11352

32. Shen, Y., Delaglio, F., Cornilescu, G., and Bax, A. (2009) TALOS+: a hybrid method for predicting protein backbone torsion angles from NMR chemical shifts. *Journal of biomolecular NMR* **44**, 213-223

33. Guntert, P. (2004) Automated NMR structure calculation with CYANA. *Methods Mol Biol* **278**, 353-378

34. Schwieters, C. D., Kuszewski, J. J., Tjandra, N., and Clore, G. M. (2003) The Xplor-NIH NMR molecular structure determination package. *J Magn Reson* **160**, 65-73

35. Lyon, M., Deakin, J. A., Lietha, D., Gherardi, E., and Gallagher, J. T. (2004) The interactions of hepatocyte growth factor/scatter factor and its NK1 and NK2 variants with glycosaminoglycans using a modified gel mobility shift assay.

Elucidation of the minimal size of binding and activatory oligosaccharides. *The Journal of biological chemistry* **279**, 43560-43567

36. Farmer, B. T., 2nd, Constantine, K. L., Goldfarb, V., Friedrichs, M. S., Wittekind, M., Yanchunas, J., Jr., Robertson, J. G., and Mueller, L. (1996) Localizing the NADP+ binding site on the MurB enzyme by NMR. *Nature structural biology* **3**, 995-997

37. Pikas, D. S., Brown, E. L., Gurusiddappa, S., Lee, L. Y., Xu, Y., and Hook, M. (2003) Decorin-binding sites in the adhesin DbpA from Borrelia burgdorferi: a synthetic peptide approach. *The Journal of biological chemistry* **278**, 30920-30926

38. Lipari, G., and Szabo, A. (1982) Model-Free Approach to the Interpretation of Nuclear Magnetic-Resonance Relaxation in Macromolecules .1. Theory and Range of Validity. *J Am Chem Soc* **104**, 4546-4559

39. Lipari, G., and Szabo, A. (1982) Model-Free Approach to the Interpretation of Nuclear Magnetic-Resonance Relaxation in Macromolecules .2. Analysis of Experimental Results. *J Am Chem Soc* **104**, 4559-4570

40. Morgan, A. M., and Wang, X. (2015) Structural mechanisms underlying sequence-dependent variations in GAG affinities of decorin binding protein A, a Borrelia burgdorferi adhesin. *Biochem J* **467**, 439-451

41. Bertini, I., Luchinat, C., and Parigi, G. (2001) *Solution NMR of Paramagnetic Molecules: Applications to metallobiomolecules and models*, 2 ed., Elsevier Science

42. Brown, E. L., Guo, B. P., O'Neal, P., and Hook, M. (1999) Adherence of Borrelia burgdorferi. Identification of critical lysine residues in DbpA required for decorin binding. *The Journal of biological chemistry* **274**, 26272-26278

Chapter 3 References

1. Lee, J. O., Rieu, P., Arnaout, M. A., and Liddington, R. (1995) Crystal structure of the A domain from the alpha subunit of integrin CR3 (CD11b/CD18). *Cell* **80**, 631-638

2. Qu, A., and Leahy, D. J. (1995) Crystal structure of the I-domain from the CD11a/CD18 (LFA-1, alpha L beta 2) integrin. *Proceedings of the National Academy of Sciences of the United States of America* **92**, 10277-10281

3. Emsley, J., King, S. L., Bergelson, J. M., and Liddington, R. C. (1997) Crystal structure of the I domain from integrin alpha2beta1. *The Journal of biological chemistry* **272**, 28512-28517

4. Luo, B. H., Carman, C. V., and Springer, T. A. (2007) Structural basis of integrin regulation and signaling. *Annual review of immunology* **25**, 619-647

5. Zhang, K., and Chen, J. (2012) The regulation of integrin function by divalent cations. *Cell adhesion & migration* **6**, 20-29

6. Hyun, Y. M., Lefort, C. T., and Kim, M. (2009) Leukocyte integrins and their ligand interactions. *Immunologic research* **45**, 195-208

7. Springer, T. A., Thompson, W. S., Miller, L. J., Schmalstieg, F. C., and Anderson, D. C. (1984) Inherited deficiency of the Mac-1, LFA-1, p150,95 glycoprotein family and its molecular basis. *The Journal of experimental medicine* **160**, 1901-1918

8. Miller, L. J., Bainton, D. F., Borregaard, N., and Springer, T. A. (1987) Stimulated Mobilization of Monocyte Mac-1 and P150,95 Adhesion Proteins from an Intracellular Vesicular Compartment to the Cell-Surface. *J Clin Invest* **80**, 535-544

9. Diamond, M. S., and Springer, T. A. (1993) A subpopulation of Mac-1 (CD11b/CD18) molecules mediates neutrophil adhesion to ICAM-1 and fibrinogen. *The Journal of cell biology* **120**, 545-556

10. Podolnikova, N. P., Podolnikov, A. V., Haas, T. A., Lishko, V. K., and Ugarova, T. P. (2015) Ligand recognition specificity of leukocyte integrin alphaMbeta2 (Mac-1, CD11b/CD18) and its functional consequences. *Biochemistry* **54**, 1408-1420

11. Altieri, D. C., Bader, R., Mannucci, P. M., and Edgington, T. S. (1988) Oligospecificity of the cellular adhesion receptor Mac-1 encompasses an inducible recognition specificity for fibrinogen. *The Journal of cell biology* **107**, 1893-1900

12. Beller, D. I., Springer, T. A., and Schreiber, R. D. (1982) Anti-Mac-1 selectively inhibits the mouse and human type three complement receptor. *The Journal of experimental medicine* **156**, 1000-1009

13. Catanzariti, A. M., Soboleva, T. A., Jans, D. A., Board, P. G., and Baker, R. T. (2004) An efficient system for high-level expression and easy purification of authentic recombinant proteins. *Protein science : a publication of the Protein Society* **13**, 1331-1339

14. Delaglio, F., Grzesiek, S., Vuister, G. W., Zhu, G., Pfeifer, J., and Bax, A. (1995) NMRPipe: a multidimensional spectral processing system based on UNIX pipes. *Journal of biomolecular NMR* **6**, 277-293

15. Johnson, B. A. (2004) Using NMRView to visualize and analyze the NMR spectra of macromolecules. *Methods in molecular biology* **278**, 313-352

16. Hafsa, N. E., Arndt, D., and Wishart, D. S. (2015) CSI 3.0: a web server for identifying secondary and super-secondary structure in proteins using NMR chemical shifts. *Nucleic acids research* **43**, W370-377

17. Lee, J. O., Bankston, L. A., Arnaout, M. A., and Liddington, R. C. (1995) Two conformations of the integrin A-domain (I-domain): a pathway for activation? *Structure* **3**, 1333-1340

18. Bryant, R. G. (1983) The Nmr Time Scale. *J Chem Educ* **60**, 933-935

19. Fassolari, M., Chemes, L. B., Gallo, M., Smal, C., Sanchez, I. E., and de Prat-Gay, G. (2013) Minute time scale prolyl isomerization governs antibody recognition of an intrinsically disordered immunodominant epitope. *The Journal of biological chemistry* **288**, 13110-13123

20. Sarkar, P., Reichman, C., Saleh, T., Birge, R. B., and Kalodimos, C. G. (2007) Proline cis-trans isomerization controls autoinhibition of a signaling protein. *Molecular cell* **25**, 413-426

21. Paradise, R. K., Lauffenburger, D. A., and Van Vliet, K. J. (2011) Acidic extracellular pH promotes activation of integrin alpha(v)beta(3). *PloS one* **6**, e15746

22. Stock, C., Gassner, B., Hauck, C. R., Arnold, H., Mally, S., Eble, J. A., Dieterich, P., and Schwab, A. (2005) Migration of human melanoma cells depends on extracellular pH and Na+/H+ exchange. *The Journal of physiology* **567**, 225-238

23. Takagi, J., Petre, B. M., Walz, T., and Springer, T. A. (2002) Global conformational rearrangements in integrin extracellular domains in outside-in and inside-out signaling. *Cell* **110**, 599-511

24. Mould, A. P., Akiyama, S. K., and Humphries, M. J. (1995) Regulation of integrin alpha 5 beta 1-fibronectin interactions by divalent cations. Evidence for distinct classes of binding sites for Mn2+, Mg2+, and Ca2+. *The Journal of biological chemistry* **270**, 26270-26277

25. Mould, A. P., Askari, J. A., Barton, S., Kline, A. D., McEwan, P. A., Craig, S. E., and Humphries, M. J. (2002) Integrin activation involves a conformational change in the alpha 1 helix of the beta subunit A-domain. *The Journal of biological chemistry* **277**, 19800-19805

26. Kovrigin, E. L. (2012) NMR line shapes and multi-state binding equilibria. *Journal of biomolecular NMR* **53**, 257-270

27. Ajroud, K., Sugimori, T., Goldmann, W. H., Fathallah, D. M., Xiong, J. P., and Arnaout, M. A. (2004) Binding Affinity of Metal Ions to the CD11b A-domain Is Regulated by Integrin Activation and Ligands. *The Journal of biological chemistry* **279**, 25483-25488

28. Xie, C., Zhu, J., Chen, X., Mi, L., Nishida, N., and Springer, T. A. (2010) Structure of an integrin with an alphaI domain, complement receptor type 4. *The EMBO journal* **29**, 666-679

29. Clore, G. M., and Iwahara, J. (2009) Theory, practice, and applications of paramagnetic relaxation enhancement for the characterization of transient low-population states of biological macromolecules and their complexes. *Chemical reviews* **109**, 4108-4139

30. Vinogradova, O., Velyvis, A., Velyviene, A., Hu, B., Haas, T., Plow, E., and Qin, J. (2002) A structural mechanism of integrin alpha(IIb)beta(3) "inside-out" activation as regulated by its cytoplasmic face. *Cell* **110**, 587-597

31. Vinogradova, O., Vaynberg, J., Kong, X., Haas, T. A., Plow, E. F., and Qin, J. (2004) Membrane-mediated structural transitions at the cytoplasmic face during integrin activation. *Proceedings of the National Academy of Sciences of the United States of America* **101**, 4094-4099

32. Lau, T. L., Partridge, A. W., Ginsberg, M. H., and Ulmer, T. S. (2008) Structure of the integrin beta3 transmembrane segment in phospholipid bicelles and detergent micelles. *Biochemistry* **47**, 4008-4016

33. Lau, T. L., Kim, C., Ginsberg, M. H., and Ulmer, T. S. (2009) The structure of the integrin alphaIIbbeta3 transmembrane complex explains integrin transmembrane signalling. *The EMBO journal* **28**, 1351-1361

34. Yang, J., Ma, Y. Q., Page, R. C., Misra, S., Plow, E. F., and Qin, J. (2009) Structure of an integrin alphaIIb beta3 transmembrane-cytoplasmic heterocomplex provides insight into integrin activation. *Proceedings of the National Academy of Sciences of the United States of America* **106**, 17729-17734

35. Kim, C., Schmidt, T., Cho, E. G., Ye, F., Ulmer, T. S., and Ginsberg, M. H. (2011) Basic amino-acid side chains regulate transmembrane integrin signalling. *Nature* **481**, 209-213

36. Schmidt, T., Situ, A. J., and Ulmer, T. S. (2016) Structural and thermodynamic basis of proline-induced transmembrane complex stabilization. *Scientific reports* **6**, 29809

37. Chin, Y. K., Headey, S. J., Mohanty, B., Patil, R., McEwan, P. A., Swarbrick, J. D., Mulhern, T. D., Emsley, J., Simpson, J. S., and Scanlon, M. J. (2013) The

structure of integrin alpha1I domain in complex with a collagen-mimetic peptide. *The Journal of biological chemistry* **288**, 36796-36809

38. Nunes, A. M., Zhu, J., Jezioro, J., Minetti, C. A., Remeta, D. P., Farndale, R. W., Hamaia, S. W., and Baum, J. (2016) Intrinsic local destabilization of the C-terminus predisposes integrin alpha1 I domain to a conformational switch induced by collagen binding. *Protein science : a publication of the Protein Society* **25**, 1672-1681

39. Chin, Y. K., Headey, S., Mohanty, B., Emsley, J., Simpson, J. S., and Scanlon, M. J. (2014) Assignments of human integrin alpha1I domain in the apo and Mg(2)(+) bound states. *Biomolecular NMR assignments* **8**, 117-121

40. Elshorst, B., Jacobs, D. M., Schwalbe, H., and Langer, T. (2003) 1H, 13C and 15N backbone resonance assignment of the integrin alpha2 I-domain. *Journal of biomolecular NMR* **27**, 191-192

41. Crump, M. P., Ceska, T. A., Spyracopoulos, L., Henry, A., Archibald, S. C., Alexander, R., Taylor, R. J., Findlow, S. C., O'Connell, J., Robinson, M. K., and Shock, A. (2004) Structure of an allosteric inhibitor of LFA-1 bound to the I-domain studied by crystallography, NMR, and calorimetry. *Biochemistry* **43**, 2394-2404

42. Huth, J. R., Olejniczak, E. T., Mendoza, R., Liang, H., Harris, E. A., Lupher, M. L., Jr., Wilson, A. E., Fesik, S. W., and Staunton, D. E. (2000) NMR and mutagenesis evidence for an I domain allosteric site that regulates lymphocyte function-associated antigen 1 ligand binding. *Proceedings of the National Academy of Sciences of the United States of America* **97**, 5231-5236

43. Zimmerman, T., Oyarzabal, J., Sebastian, E. S., Majumdar, S., Tejo, B. A., Siahaan, T. J., and Blanco, F. J. (2007) ICAM-1 peptide inhibitors of T-cell adhesion bind to the allosteric site of LFA-1. An NMR characterization. *Chemical biology & drug design* **70**, 347-353

44. Legge, G. B., Kriwacki, R. W., Chung, J., Hommel, U., Ramage, P., Case, D. A., Dyson, H. J., and Wright, P. E. (2000) NMR solution structure of the inserted domain of human leukocyte function associated antigen-1. *Journal of molecular biology* **295**, 1251-1264

45. Baldwin, E. T., Sarver, R. W., Bryant, G. L., Jr., Curry, K. A., Fairbanks, M. B., Finzel, B. C., Garlick, R. L., Heinrikson, R. L., Horton, N. C., Kelley, L. L., Mildner, A. M., Moon, J. B., Mott, J. E., Mutchler, V. T., Tomich, C. S., Watenpaugh, K. D., and Wiley, V. H. (1998) Cation binding to the integrin CD11b I domain and activation model assessment. *Structure* **6**, 923-935

46. Yang, W., Shimaoka, M., Salas, A., Takagi, J., and Springer, T. A. (2004) Intersubunit signal transmission in integrins by a receptor-like interaction with a pull spring. *Proceedings of the National Academy of Sciences of the United States of America* **101**, 2906-2911

47. Shimaoka, M., and Springer, T. A. (2003) Therapeutic antagonists and conformational regulation of integrin function. *Nature reviews. Drug discovery* **2**, 703-716

48. Xiong, J. P., Li, R., Essafi, M., Stehle, T., and Arnaout, M. A. (2000) An isoleucine-based allosteric switch controls affinity and shape shifting in integrin CD11b A-domain. *The Journal of biological chemistry* **275**, 38762-38767

Chapter 4 References

1. Luo, B. H., Carman, C. V., and Springer, T. A. (2007) Structural basis of integrin regulation and signaling. *Annual review of immunology* **25**, 619-647

2. Abram, C. L., and Lowell, C. A. (2009) The ins and outs of leukocyte integrin signaling. *Annual review of immunology* **27**, 339-362

3. Song, G., Yang, Y., Liu, J. H., Casasnovas, J. M., Shimaoka, M., Springer, T. A., and Wang, J. H. (2005) An atomic resolution view of ICAM recognition in a complex between the binding domains of ICAM-3 and integrin alphaLbeta2. *Proceedings of the National Academy of Sciences of the United States of America* **102**, 3366-3371

4. Mahalingam, B., Ajroud, K., Alonso, J. L., Anand, S., Adair, B. D., Horenstein, A. L., Malavasi, F., Xiong, J. P., and Arnaout, M. A. (2011) Stable coordination of the inhibitory Ca2+ ion at the metal ion-dependent adhesion site in integrin CD11b/CD18 by an antibody-derived ligand aspartate: implications for integrin regulation and structure-based drug design. *Journal of immunology* **187**, 6393-6401

5. Carafoli, F., Hamaia, S. W., Bihan, D., Hohenester, E., and Farndale, R. W. (2013) An activating mutation reveals a second binding mode of the integrin alpha2 I domain to the GFOGER motif in collagens. *PloS one* **8**, e69833

6. Bajic, G., Yatime, L., Sim, R. B., Vorup-Jensen, T., and Andersen, G. R. (2013) Structural insight on the recognition of surface-bound opsonins by the integrin I domain of complement receptor 3. *Proceedings of the National Academy of Sciences of the United States of America* **110**, 16426-16431

7. Pentikainen, O., Hoffren, A. M., Ivaska, J., Kapyla, J., Nyronen, T., Heino, J., and Johnson, M. S. (1999) "RKKH" peptides from the snake venom metalloproteinase of Bothrops jararaca bind near the metal ion-dependent adhesion site of the

human integrin alpha(2) I-domain. *The Journal of biological chemistry* **274**, 31493-31505

8. Yakubenko, V. P., Lishko, V. K., Lam, S. C., and Ugarova, T. P. (2002) A molecular basis for integrin alphaMbeta 2 ligand binding promiscuity. *The Journal of biological chemistry* **277**, 48635-48642

9. Lishko, V. K., Moreno, B., Podolnikova, N. P., and Ugarova, T. P. (2016) Identification of Human Cathelicidin Peptide LL-37 as a Ligand for Macrophage Integrin alphaMbeta2 (Mac-1, CD11b/CD18) that Promotes Phagocytosis by Opsonizing Bacteria. *Research and reports in biochemistry* **2016**, 39-55

10. Podolnikova, N. P., Brothwell, J. A., and Ugarova, T. P. (2015) The opioid peptide dynorphin A induces leukocyte responses via integrin Mac-1 (alphaMbeta2, CD11b/CD18). *Molecular pain* **11**, 33

11. Shen, D., Podolnikova, N. P., Yakubenko, V. P., Ardell, C. L., Balabiyev, A., Ugarova, T. P., and Wang, X. (2017) Pleiotrophin, a multifunctional cytokine and growth factor, induces leukocyte responses through the integrin Mac-1. *The Journal of biological chemistry* **292**, 18848-18861

12. Lishko, V. K., Yakubenko, V. P., Ugarova, T. P., and Podolnikova, N. P. (2018) Leukocyte integrin Mac-1 (CD11b/CD18, alphaMbeta2, CR3) acts as a functional receptor for platelet factor 4. *The Journal of biological chemistry* **293**, 6869-6882

13. Ajroud, K., Sugimori, T., Goldmann, W. H., Fathallah, D. M., Xiong, J. P., and Arnaout, M. A. (2004) Binding Affinity of Metal Ions to the CD11b A-domain Is Regulated by Integrin Activation and Ligands. *The Journal of biological chemistry* **279**, 25483-25488

14. Catanzariti, A. M., Soboleva, T. A., Jans, D. A., Board, P. G., and Baker, R. T. (2004) An efficient system for high-level expression and easy purification of authentic recombinant proteins. *Protein science : a publication of the Protein Society* **13**, 1331-1339

15. Ryan, E., Shen, D., and Wang, X. (2016) Structural studies reveal an important role for the pleiotrophin C-terminus in mediating interactions with chondroitin sulfate. *The FEBS journal* **283**, 1488-1503

16. Delaglio, F., Grzesiek, S., Vuister, G. W., Zhu, G., Pfeifer, J., and Bax, A. (1995) NMRPipe: a multidimensional spectral processing system based on UNIX pipes. *Journal of biomolecular NMR* **6**, 277-293

17. Johnson, B. A. (2004) Using NMRView to visualize and analyze the NMR spectra of macromolecules. *Methods in molecular biology* **278**, 313-352

18. Farmer, B. T., 2nd, Constantine, K. L., Goldfarb, V., Friedrichs, M. S., Wittekind, M., Yanchunas, J., Jr., Robertson, J. G., and Mueller, L. (1996) Localizing the NADP+ binding site on the MurB enzyme by NMR. *Nature structural biology* **3**, 995-997

19. Iwahara, J., Tang, C., and Marius Clore, G. (2007) Practical aspects of (1)H transverse paramagnetic relaxation enhancement measurements on macromolecules. *Journal of magnetic resonance* **184**, 185-195

20. Lee, J. O., Rieu, P., Arnaout, M. A., and Liddington, R. (1995) Crystal structure of the A domain from the alpha subunit of integrin CR3 (CD11b/CD18). *Cell* **80**, 631-638

21. Wishart, D. S., and Sykes, B. D. (1994) The 13C chemical-shift index: a simple method for the identification of protein secondary structure using 13C chemical-shift data. *Journal of biomolecular NMR* **4**, 171-180

22. Wishart, D. S., Sykes, B. D., and Richards, F. M. (1992) The chemical shift index: a fast and simple method for the assignment of protein secondary structure through NMR spectroscopy. *Biochemistry* **31**, 1647-1651

23. Chin, Y. K., Headey, S., Mohanty, B., Emsley, J., Simpson, J. S., and Scanlon, M. J. (2014) Assignments of human integrin alpha1I domain in the apo and Mg(2)(+) bound states. *Biomolecular NMR assignments* **8**, 117-121

24. Lee, J. O., Bankston, L. A., Arnaout, M. A., and Liddington, R. C. (1995) Two conformations of the integrin A-domain (I-domain): a pathway for activation? *Structure* **3**, 1333-1340

25. Shimaoka, M., Xiao, T., Liu, J. H., Yang, Y., Dong, Y., Jun, C. D., McCormack, A., Zhang, R., Joachimiak, A., Takagi, J., Wang, J. H., and Springer, T. A. (2003) Structures of the alpha L I domain and its complex with ICAM-1 reveal a shape-shifting pathway for integrin regulation. *Cell* **112**, 99-111

26. Loscalzo, J., Melnick, B., and Handin, R. I. (1985) The interaction of platelet factor four and glycosaminoglycans. *Archives of biochemistry and biophysics* **240**, 446-455

27. Maeda, N., Fukazawa, N., and Hata, T. (2006) The binding of chondroitin sulfate to pleiotrophin/heparin-binding growth-associated molecule is regulated by chain length and oversulfated structures. *The Journal of biological chemistry* **281**, 4894-4902

28. Li, J., and Springer, T. A. (2017) Integrin extension enables ultrasensitive regulation by cytoskeletal force. *Proceedings of the National Academy of Sciences of the United States of America* **114**, 4685-4690

29. Durrant, T. N., van den Bosch, M. T., and Hers, I. (2017) Integrin alphaIIbbeta3 outside-in signaling. *Blood* **130**, 1607-1619

Chapter 5 References

1. Ortega, G., Pons, M., and Millet, O. (2013) Protein functional dynamics in multiple timescales as studied by NMR spectroscopy. *Advances in protein chemistry and structural biology* **92**, 219-251

2. Mittermaier, A. K., and Kay, L. E. (2009) Observing biological dynamics at atomic resolution using NMR. *Trends in biochemical sciences* **34**, 601-611

3. Abragam, A. (1961) *The principles of nuclear magnetism*, Clarendon Press, Oxford,

4. Solomon, I. (1955) Relaxation Processes in a System of 2 Spins. *Phys Rev* **99**, 559-565

5. Luginbuhl, P., and Wuthrich, K. (2002) Semi-classical nuclear spin relaxation theory revisited for use with biological macromolecules. *Prog Nucl Mag Res Sp* **40**, 199-247

6. Neuhaus, D., and Williamson, M. P. (2000) *The nuclear Overhauser effect in structural and conformational analysis*, 2nd ed., Wiley, New York

7. Lipari, G., and Szabo, A. (1982) Model-Free Approach to the Interpretation of Nuclear Magnetic-Resonance Relaxation in Macromolecules .1. Theory and Range of Validity. *J Am Chem Soc* **104**, 4546-4559

8. Lipari, G., and Szabo, A. (1982) Model-Free Approach to the Interpretation of Nuclear Magnetic-Resonance Relaxation in Macromolecules .2. Analysis of Experimental Results. *J Am Chem Soc* **104**, 4559-4570

9. Kay, L. E., Torchia, D. A., and Bax, A. (1989) Backbone dynamics of proteins as studied by 15N inverse detected heteronuclear NMR spectroscopy: application to staphylococcal nuclease. *Biochemistry* **28**, 8972-8979

10. Pochapsky, T. C., and Pochapsky, S. S. (2007) *NMR for physical and biological scientists*, Taylor & Francis, New York

11. Mcconnell, H. M. (1958) Reaction Rates by Nuclear Magnetic Resonance. *J Chem Phys* **28**, 430-431

12. Abergel, D., and Palmer, A. G. (2004) Approximate solutions of the Bloch-McConnell equations for two-site chemical exchange. *Chemphyschem : a European journal of chemical physics and physical chemistry* **5**, 787-793

13. Carr, H. Y., and Purcell, E. M. (1954) Effects of Diffusion on Free Precession in Nuclear Magnetic Resonance Experiments. *Phys Rev* **94**, 630-638

14. Meiboom, S., and Gill, D. (1958) Modified Spin-Echo Method for Measuring Nuclear Relaxation Times. *Rev Sci Instrum* **29**, 688-691

15. Mittermaier, A. K., and Kay, L. E. (2009) Observing biological dynamics at atomic resolution using NMR. *Trends in biochemical sciences* **34**, 601-611

16. Luo, B. H., Carman, C. V., and Springer, T. A. (2007) Structural basis of integrin regulation and signaling. *Annual review of immunology* **25**, 619-647

17. Campbell, I. D., and Humphries, M. J. (2011) Integrin structure, activation, and interactions. *Cold Spring Harbor perspectives in biology* **3**

18. Lee, J. O., Rieu, P., Arnaout, M. A., and Liddington, R. (1995) Crystal structure of the A domain from the alpha subunit of integrin CR3 (CD11b/CD18). *Cell* **80**, 631-638

19. Lee, J. O., Bankston, L. A., Arnaout, M. A., and Liddington, R. C. (1995) Two conformations of the integrin A-domain (I-domain): a pathway for activation? *Structure* **3**, 1333-1340

20. Humphries, M. J. (2004) Monoclonal antibodies as probes of integrin priming and activation. *Biochemical Society transactions* **32**, 407-411

21. Oxvig, C., Lu, C., and Springer, T. A. (1999) Conformational changes in tertiary structure near the ligand binding site of an integrin I domain. *Proceedings of the National Academy of Sciences of the United States of America* **96**, 2215-2220

22. Xiong, J. P., Li, R., Essafi, M., Stehle, T., and Arnaout, M. A. (2000) An isoleucine-based allosteric switch controls affinity and shape shifting in integrin CD11b A-domain. *The Journal of biological chemistry* **275**, 38762-38767

23. Shimaoka, M., Lu, C., Salas, A., Xiao, T., Takagi, J., and Springer, T. A. (2002) Stabilizing the integrin alpha M inserted domain in alternative conformations with a range of engineered disulfide bonds. *Proceedings of the National Academy of Sciences of the United States of America* **99**, 16737-16741

24. McCleverty, C. J., and Liddington, R. C. (2003) Engineered allosteric mutants of the integrin alphaMbeta2 I domain: structural and functional studies. *The Biochemical journal* **372**, 121-127

25. Xie, C., Zhu, J., Chen, X., Mi, L., Nishida, N., and Springer, T. A. (2010) Structure of an integrin with an alphaI domain, complement receptor type 4. *The EMBO journal* **29**, 666-679

26. Weinreb, P. H., Li, S., Gao, S. X., Liu, T., Pepinsky, R. B., Caravella, J. A., Lee, J. H., and Woods, V. L., Jr. (2012) Dynamic structural changes are observed upon collagen and metal ion binding to the integrin alpha1 I domain. *The Journal of biological chemistry* **287**, 32897-32912

27. Zhang, L., and Plow, E. F. (1999) Amino acid sequences within the alpha subunit of integrin alpha M beta 2 (Mac-1) critical for specific recognition of C3bi. *Biochemistry* **38**, 8064-8071

28. Podolnikova, N. P., Podolnikov, A. V., Haas, T. A., Lishko, V. K., and Ugarova, T. P. (2015) Ligand recognition specificity of leukocyte integrin alphaMbeta2 (Mac-1, CD11b/CD18) and its functional consequences. *Biochemistry* **54**, 1408-1420

29. Nunes, A. M., Minetti, C., Remeta, D. P., and Baum, J. (2018) Magnesium Activates Microsecond Dynamics to Regulate Integrin-Collagen Recognition. *Structure* **26**, 1080-1090 e1085

30. Loria, J. P., Rance, M., and Palmer, A. G. (1999) A relaxation-compensated Carr-Purcell-Meiboom-Gill sequence for characterizing chemical exchange by NMR spectroscopy. *J Am Chem Soc* **121**, 2331-2332

31. Delaglio, F., Grzesiek, S., Vuister, G. W., Zhu, G., Pfeifer, J., and Bax, A. (1995) NMRPipe: a multidimensional spectral processing system based on UNIX pipes. *Journal of biomolecular NMR* **6**, 277-293

32. Johnson, B. A. (2004) Using NMRView to visualize and analyze the NMR spectra of macromolecules. *Methods in molecular biology* **278**, 313-352

33. Kleckner, I. R., and Foster, M. P. (2012) GUARDD: user-friendly MATLAB software for rigorous analysis of CPMG RD NMR data. *Journal of biomolecular NMR* **52**, 11-22

34. Carver, J. P., and Richards, R. E. (1972) General 2-Site Solution for Chemical Exchange Produced Dependence of T2 Upon Carr-Purcell Pulse Separation. *J Magn Reson* **6**, 89-&

35. Kim, J., Ahuja, L. G., Chao, F. A., Xia, Y., McClendon, C. L., Kornev, A. P., Taylor, S. S., and Veglia, G. (2017) A dynamic hydrophobic core orchestrates allostery in protein kinases. *Science advances* **3**, e1600663

36. Lee, A. L. (2015) Contrasting roles of dynamics in protein allostery: NMR and structural studies of CheY and the third PDZ domain from PSD-95. *Biophysical reviews* **7**, 217-226

37. Palmer, A. G., 3rd, Kroenke, C. D., and Loria, J. P. (2001) Nuclear magnetic resonance methods for quantifying microsecond-to-millisecond motions in biological macromolecules. *Methods in enzymology* **339**, 204-238

38. Ajroud, K., Sugimori, T., Goldmann, W. H., Fathallah, D. M., Xiong, J. P., and Arnaout, M. A. (2004) Binding Affinity of Metal Ions to the CD11b A-domain Is Regulated by Integrin Activation and Ligands. *The Journal of biological chemistry* **279**, 25483-25488

39. Xiong, J. P., Stehle, T., Diefenbach, B., Zhang, R., Dunker, R., Scott, D. L., Joachimiak, A., Goodman, S. L., and Arnaout, M. A. (2001) Crystal structure of the extracellular segment of integrin alpha Vbeta3. *Science* **294**, 339-345

40. Zhu, J., Luo, B. H., Xiao, T., Zhang, C., Nishida, N., and Springer, T. A. (2008) Structure of a complete integrin ectodomain in a physiologic resting state and activation and deactivation by applied forces. *Molecular cell* **32**, 849-861

41. Nermut, M. V., Green, N. M., Eason, P., Yamada, S. S., and Yamada, K. M. (1988) Electron microscopy and structural model of human fibronectin receptor. *The EMBO journal* **7**, 4093-4099

42. Carrell, N. A., Fitzgerald, L. A., Steiner, B., Erickson, H. P., and Phillips, D. R. (1985) Structure of human platelet membrane glycoproteins IIb and IIIa as determined by electron microscopy. *The Journal of biological chemistry* **260**, 1743-1749

43. Weisel, J. W., Nagaswami, C., Vilaire, G., and Bennett, J. S. (1992) Examination of the platelet membrane glycoprotein IIb-IIIa complex and its interaction with fibrinogen and other ligands by electron microscopy. *The Journal of biological chemistry* **267**, 16637-16643

44. Shtengel, G., Galbraith, J. A., Galbraith, C. G., Lippincott-Schwartz, J., Gillette, J. M., Manley, S., Sougrat, R., Waterman, C. M., Kanchanawong, P., Davidson, M. W., Fetter, R. D., and Hess, H. F. (2009) Interferometric fluorescent super-resolution microscopy resolves 3D cellular ultrastructure. *Proceedings of the National Academy of Sciences of the United States of America* **106**, 3125-3130

45. Zhang, K., and Chen, J. (2012) The regulation of integrin function by divalent cations. *Cell adhesion & migration* **6**, 20-29

46. Gailit, J., and Ruoslahti, E. (1988) Regulation of the fibronectin receptor affinity by divalent cations. *The Journal of biological chemistry* **263**, 12927-12932

Chapter 6 References

1. Kjellen, L., and Lindahl, U. (1991) Proteoglycans - Structures and Interactions. *Annu Rev Biochem* **60**, 443-475

2. Schulze, R. J., and Zuckert, W. R. (2006) Borrelia burgdorferi lipoproteins are secreted to the outer surface by default. *Molecular microbiology* **59**, 1473-1484

3. Ulbrandt, N. D., Cassatt, D. R., Patel, N. K., Roberts, W. C., Bachy, C. M., Fazenbaker, C. A., and Hanson, M. S. (2001) Conformational nature of the Borrelia burgdorferi decorin binding protein A epitopes that elicit protective antibodies. *Infection and immunity* **69**, 4799-4807

4. Fischer, J. R., Parveen, N., Magoun, L., and Leong, J. M. (2003) Decorin-binding proteins A and B confer distinct mammalian cell type-specific attachment by Borrelia burgdorferi, the Lyme disease spirochete. *Proceedings of the National Academy of Sciences of the United States of America* **100**, 7307-7312

5. Roberts, W. C., Mullikin, B. A., Lathigra, R., and Hanson, M. S. (1998) Molecular analysis of sequence heterogeneity among genes encoding decorin binding proteins A and B of Borrelia burgdorferi sensu lato. *Infection and immunity* **66**, 5275-5285

6. Wang, X. (2012) Solution structure of decorin-binding protein A from Borrelia burgdorferi. *Biochemistry* **51**, 8353-8362

7. Shi, Y., Xu, Q., Seemanaplli, S. V., McShan, K., and Liang, F. T. (2008) Common and unique contributions of decorin-binding proteins A and B to the overall virulence of Borrelia burgdorferi. *PloS one* **3**, e3340

8. Shen, D., Podolnikova, N. P., Yakubenko, V. P., Ardell, C. L., Balabiyev, A., Ugarova, T. P., and Wang, X. (2017) Pleiotrophin, a multifunctional cytokine and growth factor, induces leukocyte responses through the integrin Mac-1. *The Journal of biological chemistry* **292**, 18848-18861

9. Lishko, V. K., Yakubenko, V. P., Ugarova, T. P., and Podolnikova, N. P. (2018) Leukocyte integrin Mac-1 (CD11b/CD18, alphaMbeta2, CR3) acts as a functional receptor for platelet factor 4. *The Journal of biological chemistry* **293**, 6869-6882

10. Xiong, J. P., Stehle, T., Diefenbach, B., Zhang, R., Dunker, R., Scott, D. L., Joachimiak, A., Goodman, S. L., and Arnaout, M. A. (2001) Crystal structure of the extracellular segment of integrin alpha Vbeta3. *Science* **294**, 339-345

11. Zhu, J., Luo, B. H., Xiao, T., Zhang, C., Nishida, N., and Springer, T. A. (2008) Structure of a complete integrin ectodomain in a physiologic resting state and activation and deactivation by applied forces. *Molecular cell* **32**, 849-861

12. Xie, C., Zhu, J., Chen, X., Mi, L., Nishida, N., and Springer, T. A. (2010) Structure of an integrin with an alphaI domain, complement receptor type 4. *The EMBO journal* **29**, 666-679

13. Nermut, M. V., Green, N. M., Eason, P., Yamada, S. S., and Yamada, K. M. (1988) Electron microscopy and structural model of human fibronectin receptor. *The EMBO journal* **7**, 4093-4099

14. Carrell, N. A., Fitzgerald, L. A., Steiner, B., Erickson, H. P., and Phillips, D. R. (1985) Structure of human platelet membrane glycoproteins IIb and IIIa as determined by electron microscopy. *The Journal of biological chemistry* **260**, 1743-1749

15. Weisel, J. W., Nagaswami, C., Vilaire, G., and Bennett, J. S. (1992) Examination of the platelet membrane glycoprotein IIb-IIIa complex and its interaction with fibrinogen and other ligands by electron microscopy. *The Journal of biological chemistry* **267**, 16637-16643

16. Shtengel, G., Galbraith, J. A., Galbraith, C. G., Lippincott-Schwartz, J., Gillette, J. M., Manley, S., Sougrat, R., Waterman, C. M., Kanchanawong, P., Davidson, M. W., Fetter, R. D., and Hess, H. F. (2009) Interferometric fluorescent super-resolution microscopy resolves 3D cellular ultrastructure. *Proceedings of the National Academy of Sciences of the United States of America* **106**, 3125-3130

17. Luo, B. H., Carman, C. V., and Springer, T. A. (2007) Structural basis of integrin regulation and signaling. *Annual review of immunology* **25**, 619-647

18. Nunes, A. M., Minetti, C., Remeta, D. P., and Baum, J. (2018) Magnesium Activates Microsecond Dynamics to Regulate Integrin-Collagen Recognition. *Structure* **26**, 1080-1090 e1085

19. Oxvig, C., Lu, C., and Springer, T. A. (1999) Conformational changes in tertiary structure near the ligand binding site of an integrin I domain. *Proceedings of the National Academy of Sciences of the United States of America* **96**, 2215-2220

20. Moore, T. I., Aaron, J., Chew, T. L., and Springer, T. A. (2018) Measuring Integrin Conformational Change on the Cell Surface with Super-Resolution Microscopy. *Cell reports* **22**, 1903-1912

APPENDIX A

SUPPLEMENTAL FIGURES OF CHAPTER 2.

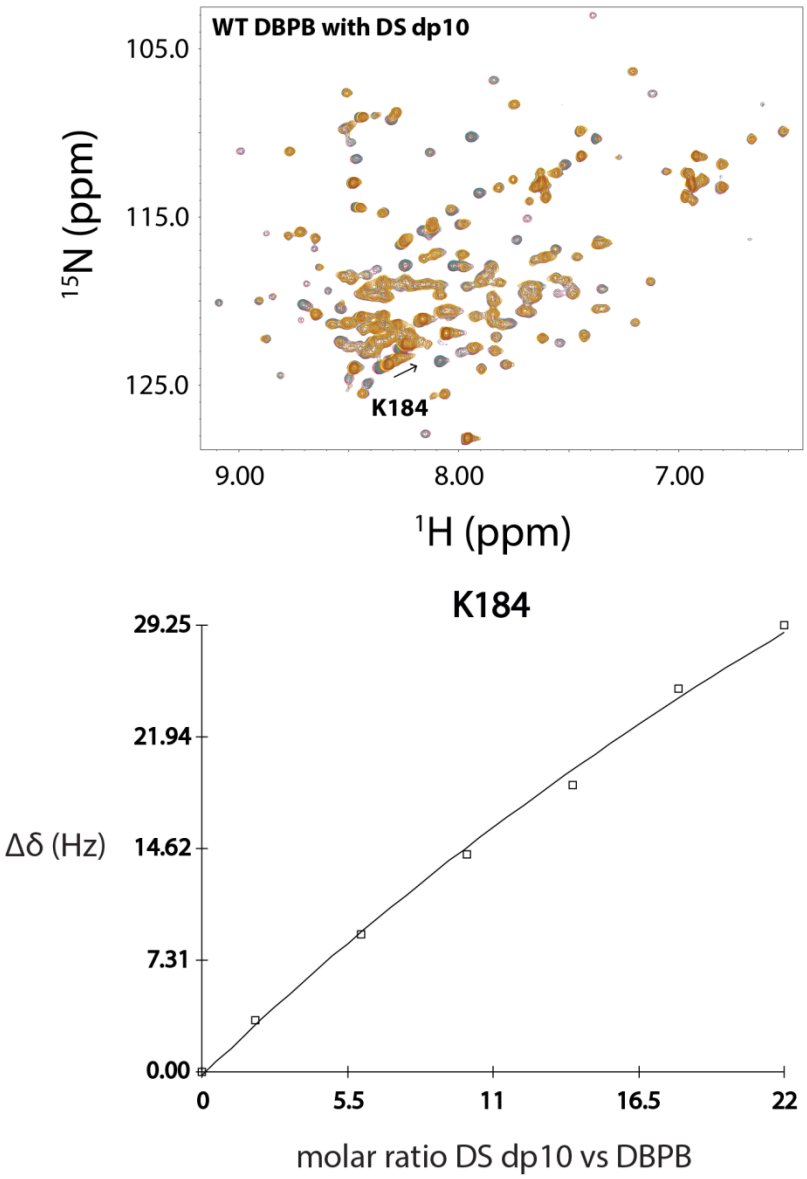

Figures 2S1 ^{1}H-^{15}N HSQC overlays (upper panel) of WT DBPB titrated with DS dp10 and fitting curve (lower panel) of residue K184. Contours are color-coded with increasing concentrations of GAG fragments (0, 0.2, 0.6, 1.0, 1.4, 1.8 and 2.2 mM). The sample contains 400 uL of 100 uM protein in 50 mM NaH_2PO_4 and 150 mM NaCl buffer (pH 6.5). K184 is displayed with an arrow indicating migration direction.

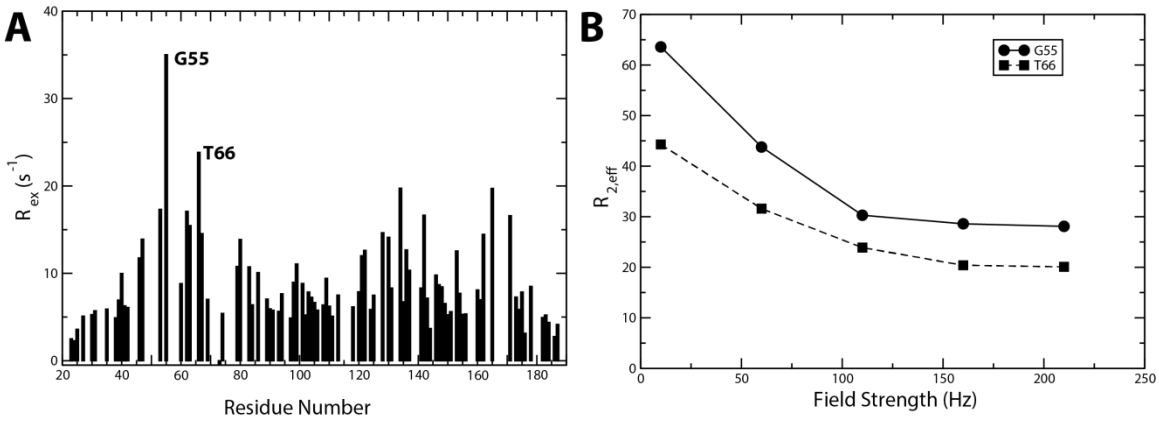

Figures 2S2 DS-induced DBPB conformational exchange characterized by CPMG-based relaxation dispersion experiments. (A) Residue specific Rex values derived from the experiment. Rex is taken as the difference between $R_{2,eff}$ values at field strengths of 10 and 210. (B) Changes in $R_{2,eff}$ of residues G55 and T66 as field strength increases.

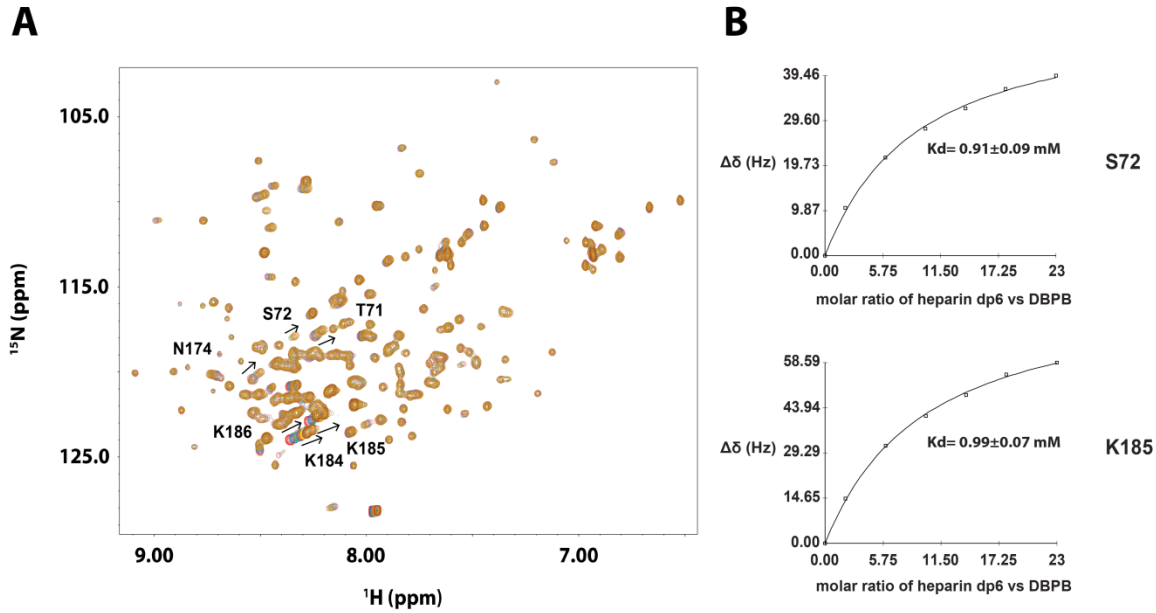

Figure 2S3 DBPB titrations with heparin dp6. (A) ^{1}H-^{15}N HSQC overlays of WT B31 DBPB with increasing concentrations of heparin dp6. Signals with large migrations are labeled with their residue numbers and arrows to indicate migration directions. (B) Fitting curves of DBPB residues S72 and K185 when titrated with heparin dp6.

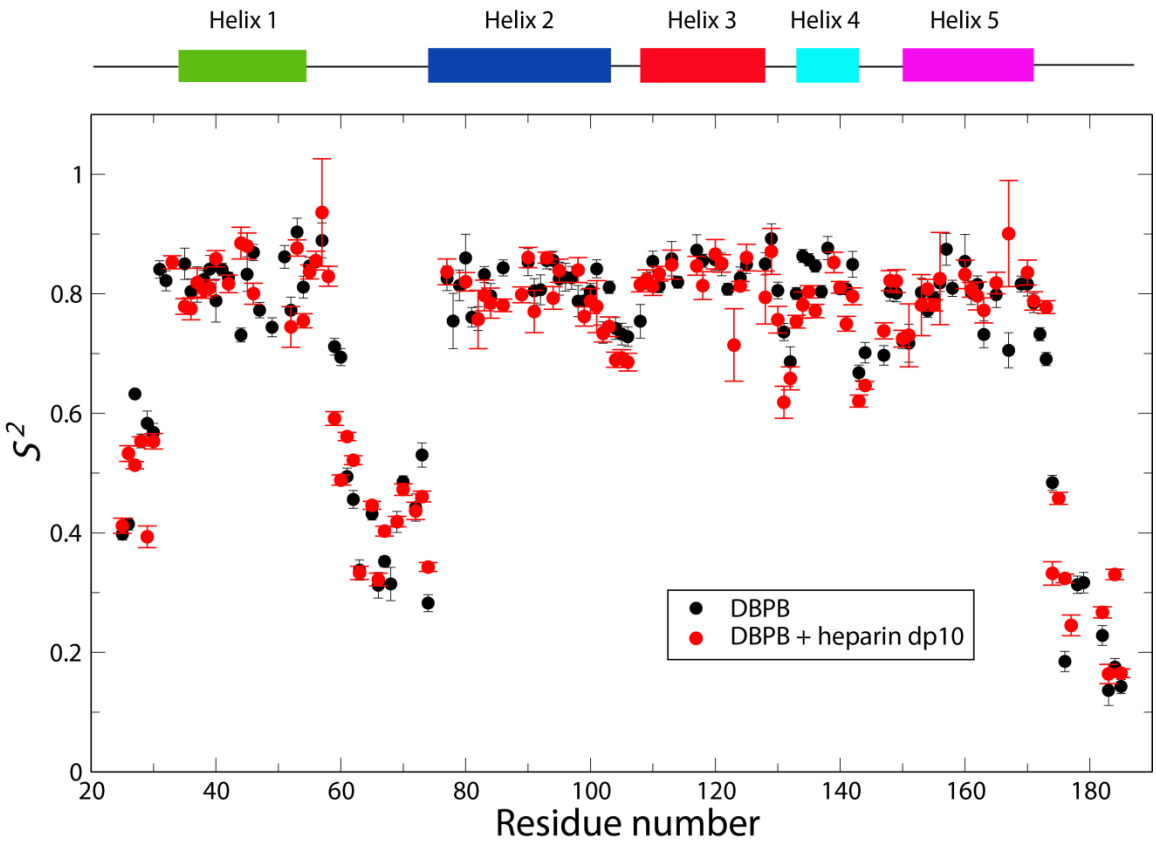

Figure 2S4 Backbone dynamics of DBPB in the presence and absence of heparin dp10. Order parameters of backbone amide nitrogen atoms for WT B31 DBPB with (red) or without (black) 10 molar equivalents of heparin dp10.

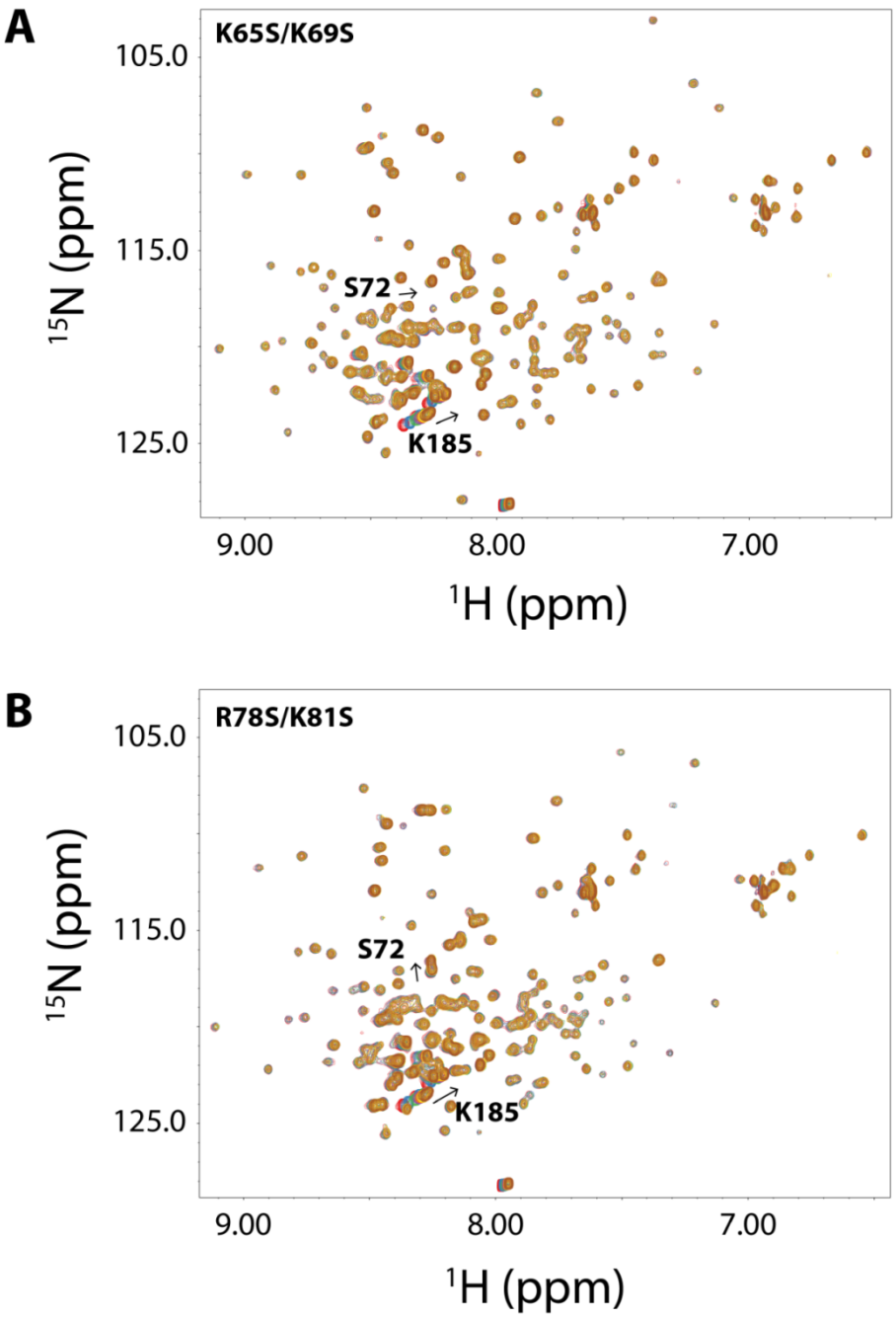

Figures 2S5 ^{1}H-^{15}N HSQC overlays (A) K65S/K69S DBPB. (B) R78S/K81S DBPB. (C) K81S/K169S DBPB. (D) $^{184}SSS^{187}$ DBPB. (E) $DBPB_{21\text{-}183}$. Contours are color-coded with increasing concentrations of GAG fragments (0, 0.2, 0.6, 1.0, 1.4, 1.8 and 2.2 mM). The sample contains 400 uL of 100 uM protein in 50 mM NaH_2PO_4 and 150 mM NaCl buffer (pH 6.5). Residues S72 and K185 were used in the Kd calculations.

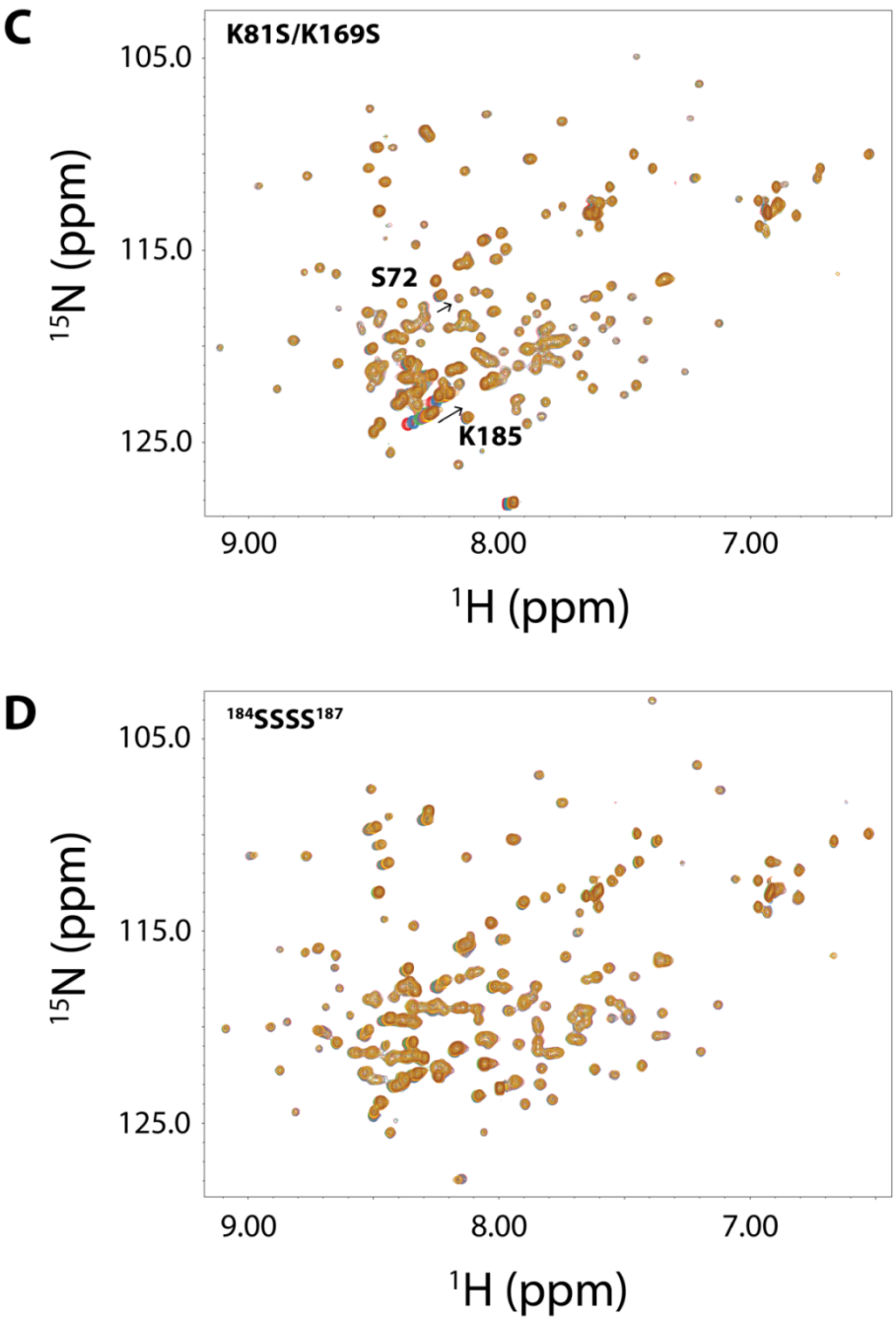

Figures 2S5 ^{1}H-^{15}N HSQC overlays (A) K65S/K69S DBPB. (B) R78S/K81S DBPB. (C) K81S/K169S DBPB. (D) $^{184}SSS^{187}$ DBPB. (E) $DBPB_{21\text{-}183}$. Contours are color-coded with increasing concentrations of GAG fragments (0, 0.2, 0.6, 1.0, 1.4, 1.8 and 2.2 mM). The sample contains 400 uL of 100 uM protein in 50 mM NaH_2PO_4 and 150 mM NaCl buffer (pH 6.5). Residues S72 and K185 were used in the Kd calculations.

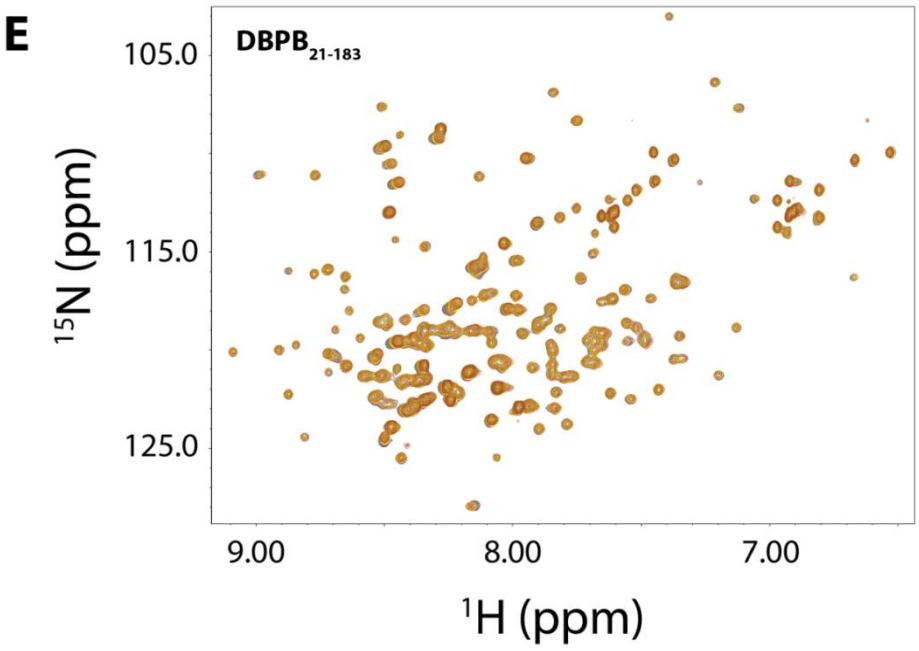

Figures 2S5 ^{1}H-^{15}N HSQC overlays (A) K65S/K69S DBPB. (B) R78S/K81S DBPB. (C) K81S/K169S DBPB. (D) ^{184}SSS^{187} DBPB. (E) DBPB$_{21-183}$. Contours are color-coded with increasing concentrations of GAG fragments (0, 0.2, 0.6, 1.0, 1.4, 1.8 and 2.2 mM). The sample contains 400 uL of 100 uM protein in 50 mM NaH_2PO_4 and 150 mM NaCl buffer (pH 6.5). Residues S72 and K185 were used in the Kd calculations.

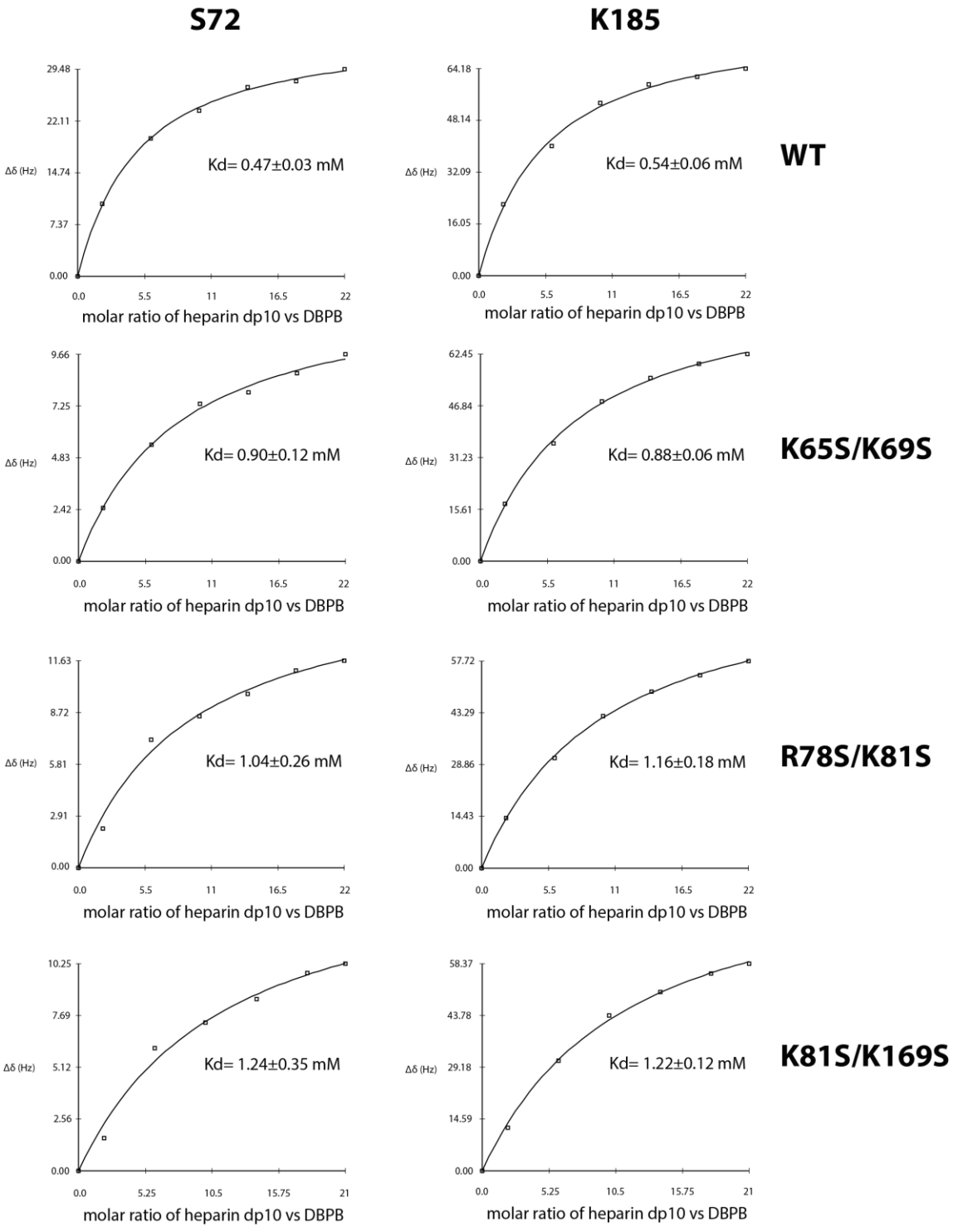

Figure 2S6 Kd binding curves of DBPBs. Kd fittings were obtained for NMR-monitored titrations using xcrvfit (http://www.bionmr.ualberta.ca/bds/software/xcrvfit/).

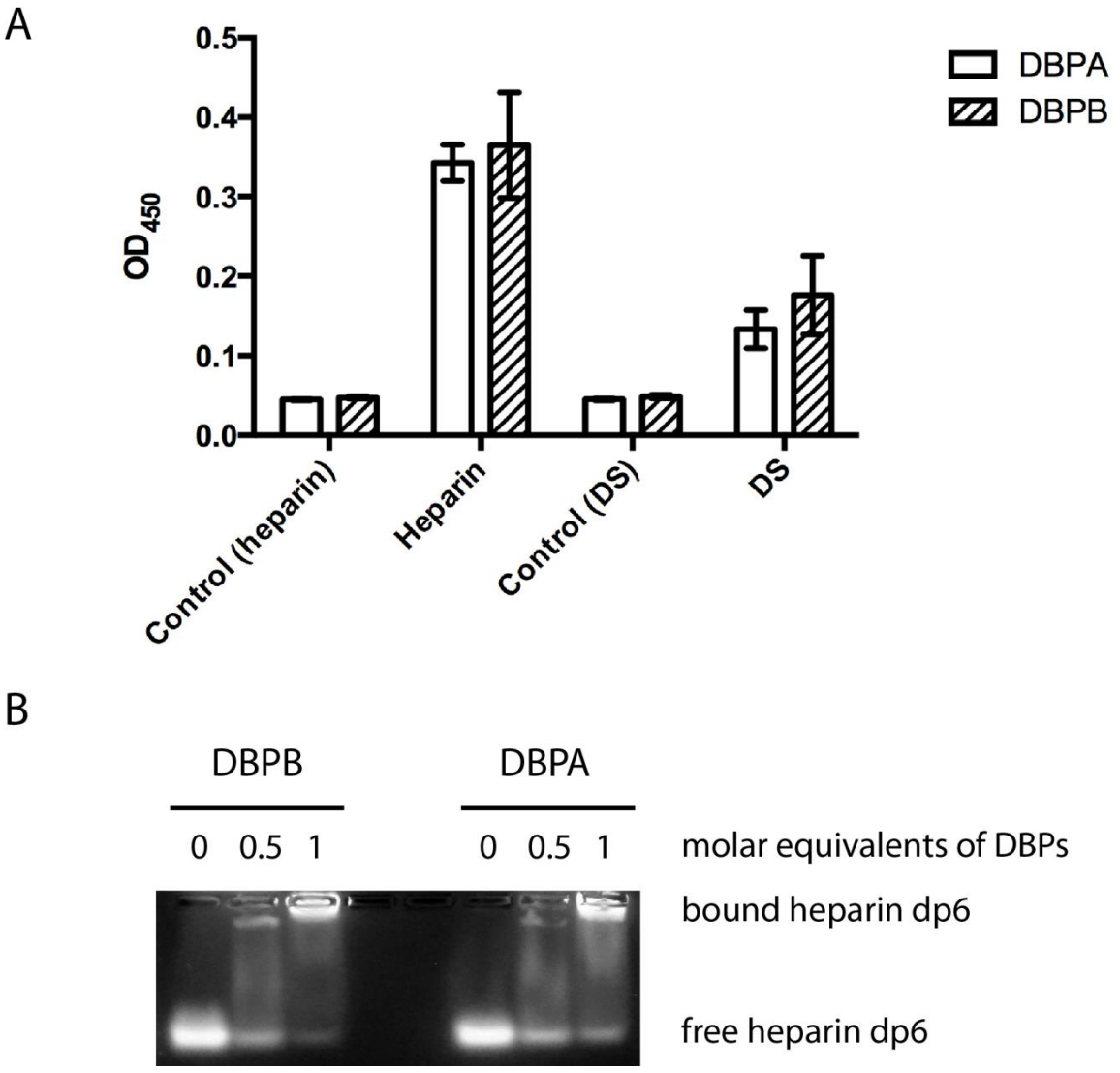

Figure 2S7 (A) Results of heparin and DS ELISA comparing the GAG affinities of B31 DBPA and DBPB. The two proteins have equal affinities for native heparin and DS. (B) Heparin dp6 GMSA of B31 DBPA and DBPB. Both proteins' affinities for size defined heparin are also similar.

APPENDIX B

SUPPLEMENTAL FIGURES OF CHAPTER 4

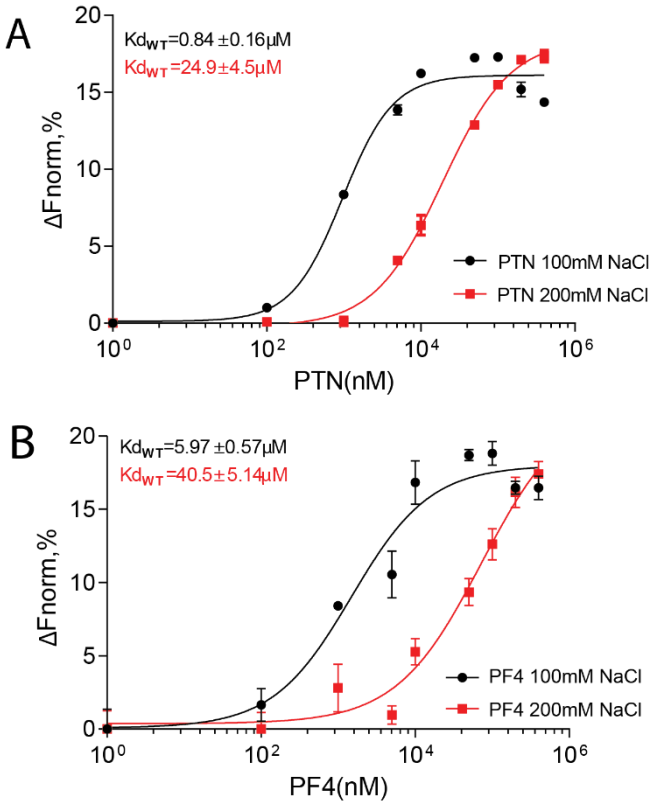

Figure 4S1 Effects of ionic strength on α_M I-domain's interactions with PTN and PF4. (A), MST-derived binding curves for interactions of PTN with Dylight 488 labeled α_M I-domain at ionic strength of 100 mM and 200 mM. (B), MST-derived binding curves for interactions of PF4 with Dylight 488 labeled α_M I-domain at ionic strength of 100 mM and 200 mM.

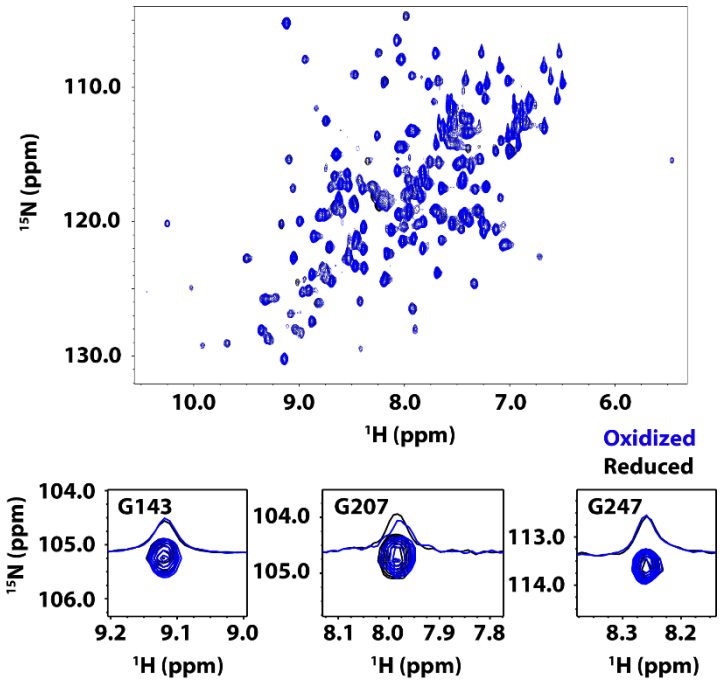

Figure 4S2 Effects of free MTSL on HSQC of α_M I-domain. ^{15}N HSQC of α_M I-domain in the presence of 0.9 mM of paramagnetic (blue) or diamagnetic (black) MTSL. Free MTSL alone has little effect on signal intensity of G143, G207 and G247.

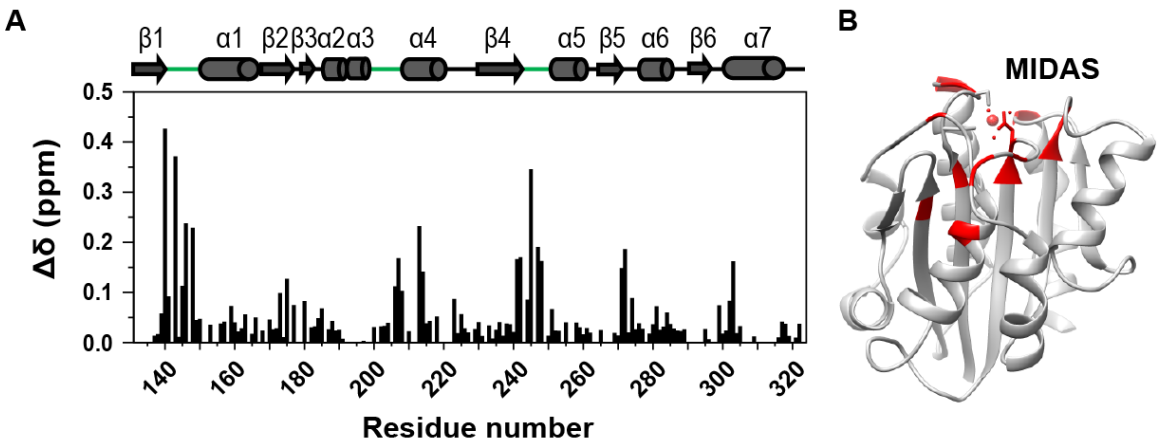

Figure 4S3 Mg^{2+} induced residue specific chemical shift changes in α_M I-domain. (A), Chemical shift changes are calculated as $\sqrt{\Delta H^2 + (0.25 * \Delta N)^2}$. Secondary structures of α_M I-domain as well as residues and regions forming the MIDAS are indicated on top of bar charts. (B), Ribbon representation of α_M I-domain showing positions of residues with significant Mg^{2+}-induced chemical shift changes.

APPENDIX C

PERMISSION FOR TABLE 1.1

JOHN WILEY AND SONS LICENSE TERMS AND CONDITIONS

Mar 06, 2019

This Agreement between Arizona State University -- Wei Feng ("You") and John Wiley and Sons ("John Wiley and Sons") consists of your license details and the terms and conditions provided by John Wiley and Sons and Copyright Clearance Center.

License Number	4543201034849
License date	Mar 06, 2019
Licensed Content Publisher	John Wiley and Sons
Licensed Content Publication	Biological Reviews
Licensed Content Title	Glycosaminoglycans in infectious disease
Licensed Content Author	Eyal Kamhi, Eun Ji Joo, Jonathan S. Dordick, et al
Licensed Content Date	Mar 29, 2013
Licensed Content Volume	88
Licensed Content Issue	4
Licensed Content Pages	16
Type of use	Dissertation/Thesis
Requestor type	University/Academic
Format	Print and electronic
Portion	Figure/table
Number of figures/tables	1
Original Wiley figure/table number(s)	Table 1
Will you be translating?	No
Title of your thesis / dissertation	Structural perspectives on glycosaminoglycan-binding proteins and their receptors
Expected completion date	Mar 2019
Expected size (number of pages)	150
Requestor Location	Arizona State University 550 E Orange St. TEMPE, AZ 85281 United States Attn: Wei Feng
Publisher Tax ID	EU826007151
Total	0.00 USD

APPENDIX D

PERMISSION FOR FIGURE 1.1

APPENDIX E

PERMISSION FOR TABLE 1.2

ELSEVIER LICENSE
TERMS AND CONDITIONS

Mar 06, 2019

This Agreement between Arizona State University -- Wei Feng ("You") and Elsevier ("Elsevier") consists of your license details and the terms and conditions provided by Elsevier and Copyright Clearance Center.

License Number	4543290964750
License date	Mar 06, 2019
Licensed Content Publisher	Elsevier
Licensed Content Publication	Elsevier Books
Licensed Content Title	Progress in Molecular Biology and Translational Science
Licensed Content Author	Lijuan Zhang
Licensed Content Date	Jan 1, 2010
Licensed Content Pages	17
Start Page	1
End Page	17
Type of Use	reuse in a thesis/dissertation
Intended publisher of new work	other
Portion	figures/tables/illustrations
Number of figures/tables/illustrations	1
Format	both print and electronic
Are you the author of this Elsevier chapter?	No
Will you be translating?	No
Original figure numbers	Figure 2
Title of your thesis/dissertation	Structural perspectives on glycosaminoglycan-binding proteins and their receptors
Publisher of new work	Arizona State University
Expected completion date	Mar 2019
Estimated size (number of pages)	150
Requestor Location	Arizona State University 550 E Orange St. TEMPE, AZ 85281 United States Attn: Wei Feng
Publisher Tax ID	98-0397604
Total	0.00 USD

APPENDIX F

PERMISSION FOR FIGURE 1.2

APPENDIX G

PERMISSION FOR FIGURE 1.3

JOHN WILEY AND SONS LICENSE TERMS AND CONDITIONS

Mar 06, 2019

This Agreement between Arizona State University -- Wei Feng ("You") and John Wiley and Sons ("John Wiley and Sons") consists of your license details and the terms and conditions provided by John Wiley and Sons and Copyright Clearance Center.

License Number	4543230218091
License date	Mar 06, 2019
Licensed Content Publisher	John Wiley and Sons
Licensed Content Publication	The EMBO Journal
Licensed Content Title	Structure of an integrin with an αI domain, complement receptor type 4
Licensed Content Author	Can Xie, Jianghai Zhu, Xing Chen, et al
Licensed Content Date	Dec 24, 2009
Licensed Content Volume	29
Licensed Content Issue	3
Licensed Content Pages	14
Type of use	Dissertation/Thesis
Requestor type	University/Academic
Format	Print and electronic
Portion	Figure/table
Number of figures/tables	1
Original Wiley figure/table number(s)	Figure 2
Will you be translating?	No
Title of your thesis / dissertation	Structural perspectives on glycosaminoglycan-binding proteins and their receptors
Expected completion date	Mar 2019
Expected size (number of pages)	150
Requestor Location	Arizona State University 550 E Orange St. TEMPE, AZ 85281 United States Attn: Wei Feng
Publisher Tax ID	EU826007151
Total	0.00 USD

APPENDIX H

PERMISSION FOR FIGURE 1.4

Order Details

Annual review of immunology

Billing Status: **N/A**

Order detail ID:	71840350
ISSN:	1545-3278
Publication Type:	e-Journal
Volume:	
Issue:	
Start page:	
Publisher:	ANNUAL REVIEWS

Permission Status: Granted

Permission type: Republish or display content
Type of use: Thesis/Dissertation
Order License Id: 4543261485414

Hide details

Requestor type	Academic institution
Format	Print, Electronic
Portion	chart/graph/table/figure
Number of charts/graphs/tables/figures	1
The requesting person/organization	Wei Feng/Arizona State University
Title or numeric reference of the portion(s)	Figure 6.
Title of the article or chapter the portion is from	Structural Basis of Integrin Regulation and Signaling
Editor of portion(s)	N/A
Author of portion(s)	Bing-Hao Luo, Christopher V. Carman, and Timothy A. Springer
Volume of serial or monograph	25
Page range of portion	619-647
Publication date of portion	2007
Rights for	Main product
Duration of use	Life of current and all future editions
Creation of copies for the disabled	no
With minor editing privileges	yes
For distribution to	United States
In the following language(s)	Original language of publication
With incidental promotional use	no
Lifetime unit quantity of new product	Up to 499
Title	Structural perspectives on glycosaminoglycan-binding proteins and their receptors
Institution name	Arizona State University
Expected presentation date	Mar 2019

Note: This item was invoiced separately through our **RightsLink service.** More info **$ 0.00**

APPENDIX I

PERMISSION TO REPRODUCE CHAPTER 2 FROM BIOCHIMICA ET BIOPHYSICA ACTA (BBA)-PROTEINS AND PROTEOMICS

APPENDIX J

PERMISSION FOR FIGURE 5.1

ELSEVIER LICENSE
TERMS AND CONDITIONS

Mar 06, 2019

This Agreement between Arizona State University -- Wei Feng ("You") and Elsevier ("Elsevier") consists of your license details and the terms and conditions provided by Elsevier and Copyright Clearance Center.

License Number	4543290065370
License date	Mar 06, 2019
Licensed Content Publisher	Elsevier
Licensed Content Publication	Elsevier Books
Licensed Content Title	Advances in Protein Chemistry and Structural Biology
Licensed Content Author	Gabriel Ortega,Miquel Pons,Oscar Millet
Licensed Content Date	Jan 1, 2013
Licensed Content Pages	33
Start Page	219
End Page	251
Type of Use	reuse in a thesis/dissertation
Intended publisher of new work	other
Portion	figures/tables/illustrations
Number of figures/tables/illustrations	1
Format	both print and electronic
Are you the author of this Elsevier chapter?	No
Will you be translating?	No
Original figure numbers	Figure 6.2
Title of your thesis/dissertation	Structural perspectives on glycosaminoglycan-binding proteins and their receptors
Publisher of new work	Arizona State University
Expected completion date	Mar 2019
Estimated size (number of pages)	150
Requestor Location	Arizona State University 550 E Orange St. TEMPE, AZ 85281 United States Attn: Wei Feng
Publisher Tax ID	98-0397604
Total	0.00 USD

APPENDIX K

PERMISSION FOR FIGURE 5.2

ELSEVIER LICENSE
TERMS AND CONDITIONS

Mar 06, 2019

This Agreement between Arizona State University -- Wei Feng ("You") and Elsevier ("Elsevier") consists of your license details and the terms and conditions provided by Elsevier and Copyright Clearance Center.

License Number	4543290504917
License date	Mar 06, 2019
Licensed Content Publisher	Elsevier
Licensed Content Publication	Trends in Biochemical Sciences
Licensed Content Title	Observing biological dynamics at atomic resolution using NMR
Licensed Content Author	Anthony K. Mittermaier,Lewis E. Kay
Licensed Content Date	Dec 1, 2009
Licensed Content Volume	34
Licensed Content Issue	12
Licensed Content Pages	11
Start Page	601
End Page	611
Type of Use	reuse in a thesis/dissertation
Intended publisher of new work	other
Portion	figures/tables/illustrations
Number of figures/tables/illustrations	1
Format	both print and electronic
Are you the author of this Elsevier article?	No
Will you be translating?	No
Original figure numbers	Figure I of Box 2
Title of your thesis/dissertation	Structural perspectives on glycosaminoglycan-binding proteins and their receptors
Publisher of new work	Arizona State University
Expected completion date	Mar 2019
Estimated size (number of pages)	150
Requestor Location	Arizona State University 550 E Orange St. TEMPE, AZ 85281 United States Attn: Wei Feng
Publisher Tax ID	98-0397604
Total	0.00 USD